Spring 6-11-2023

Intraoperative Quantification of Bone Perfusion in Lower Extremity Injury Surgery

Xinyue Han
Dartmouth College, xinyue.han.th@dartmouth.edu

INTRAOPERATIVE QUANTIFICATION OF BONE PERFUSION IN LOWER EXTREMITY INJURY SURGERY

A Thesis
Submitted to the Faculty
in partial fulfillment of the requirements for the
degree of

Doctor of Philosophy

in

Engineering Sciences

by XINYUE HAN

Thayer School of Engineering
Guarini School of Graduate and Advanced Studies
Dartmouth College
Hanover, New Hampshire

APRIL 2023

Examining Committee:

Chair_____
(Jonathan T. Elliott, Ph.D.)

Member_____
(Kimberley S. Samkoe, Ph.D.)

Member_____
(Vikrant S. Vaze, Ph.D.)

Member_____
(I. Leah Gitajn, M.D.)

_____
F. Jon Kull, Ph.D.
Dean of the Guarini School of Graduate and Advanced Studies

Abstract

Orthopaedic surgery is one of the most common surgical categories. In particular, lower extremity injuries sustained from trauma can be complex and life-threatening injuries that are addressed through orthopaedic trauma surgery. Timely evaluation and surgical debridement following lower extremity injury is essential, because devitalized bones and tissues will result in high surgical site infection rates. However, the current clinical judgment of what constitutes "devitalized tissue" is subjective and dependent on surgeon experience, so it is necessary to develop imaging techniques for guiding surgical debridement, in order to control infection rates and to improve patient outcome.

In this thesis work, computational models of fluorescence-guided debridement in lower extremity injury surgery will be developed, by quantifying bone perfusion intraoperatively using Dynamic contrast-enhanced fluorescence imaging (DCE-FI) system. Perfusion is an important factor of tissue viability, and therefore quantifying perfusion is essential for fluorescence-guided debridement. In Chapters 3-7 of this thesis, we explore the performance of DCE-FI in quantifying perfusion from benchtop to translation: We proposed a modified fluorescent microsphere quantification technique using cryomacrotome in animal model. This technique can measure bone perfusion in periosteal and endosteal separately, and therefore to validate bone perfusion measurements obtained by DCE-FI; We developed pre-clinical rodent contaminated fracture model to correlate DCE-FI with infection risk, and compare with multi-modality scanning; Furthermore in clinical studies, we investigated first-pass kinetic parameters of DCE-FI and arterial input functions for characterization of perfusion changes during lower limb amputation surgery; We conducted the first in-human use of dynamic contrast-enhanced texture analysis for

orthopaedic trauma classification, suggesting that spatiotemporal features from DCE-FI can classify bone perfusion intraoperatively with high accuracy and sensitivity; We established clinical machine learning infection risk predictive model on open fracture surgery, where pixel-scaled prediction on infection risk will be accomplished.

In conclusion, pharmacokinetic and spatiotemporal patterns of dynamic contrast-enhanced imaging show great potential for quantifying bone perfusion and prognosing bone infection. The thesis work will decrease surgical site infection risk and improve successful rates of lower extremity injury surgery.

Acknowledgements

I would firstly express my sincere gratitude to my supervisor, Dr. Jonathan Elliott, for his invaluable advice and continuous support at every stage of my journey. His profession and passion in science has a huge influence in shaping my research methodology. His patience has encouraged me to embrace every challenge with confidence. Every time I ran into problems, no matter in science or in career, he always offered the kindest support. He taught me not only hands-on skills in experiments and coding, but also insights and tastes about science, which really speed up my growth from a beginner to an independent researcher. Without his support, I would not be able to enter the scientific world smoothly and pleasantly.

I am also grateful to our Orthopeadic Translational Engineering Lab members, Dr. Valentin Demidov and Scott Sottosanti. I really appreciate their assistance and support during my time at the lab. We have collaborated in multiple projects, and I can always learn new ideas and skills from our discussion and collaboration. They have demonstrated me the value of teamwork in science.

I would also like to offer my special thanks to Dr. Leah Gitajn, the lead of clinical team and a member of my thesis committee. She always has unique vision and impact insights of every problems. Her immerse knowledge and plentiful experience has greatly inspired my research. Her devotion to science as a clinician has encouraged my career choice as a scientist on improving human health.

I would like to extend my sincere thanks to my thesis committee member from Thayer School of Engineering, Dr. Kimberley Samkoe and Dr. Vikrant Vaze. Their treasured support and help lasted through the whole journey of my PhD. Every single

progress I have made, from successful experiments and coding, to publications and international conferences, were all under their guidance and support.

I also appreciate all the support from my family and friends. My husband, Haoyu, is with me on everything, from teaching me coding, debugging, and advising on computation and algorithms, to accompanying me in attending conferences and assisting my homework. My parents are always by my side to support and help me whenever I need help.

Lastly, I would like to thank China Scholarship Council, Thayer School of Engineering at Dartmouth College, and Department of Orthopaedics at Dartmouth Health for the funding of my thesis.

Table of Contents

List of Tables

List of Figures

List of Acronyms

5-Aminolevulinic Acid	5-ALA
Adiabatic Approximation to The Tissue Homogeneity	AATH
American Society of Anesthesiologists	ASA
Area-Under-Curve	AUC
Arrival Time	Ta
Arterial Input Function	AIF
Below Knee Amputation	BKA
Bioluminescent Imaging	BLI
Body Mass Index	BMI
Cerebral Blood Flow	CBF
Colony-Forming Unit	CFU
Computed Tomography	CT
Confidence Interval	CI
Counts Per Second	CPS
Dartmouth-Hitchcock Medical Center	DHMC
Dye Densitometer	DDM
Dynamic Contrast-Enhanced	DCE
Dynamic Contrast-Enhanced Computed Tomography	DCE-CT
Dynamic Contrast-Enhanced Fluorescence Imaging	DCE-FI
Dynamic Contrast-Enhanced Magnetic Resonance Imaging	DCE-MRI
Dynamic Contrast-Enhanced Positron Emission Tomography	DCE-PET
Dynamic Contrast-Enhanced Ultrasound	DCE-US

Egress Slope	ES
Ejection Fraction	EF
Endosteal Blood Flow	EBF
Fluorescence Intensity	FI
Fluorescence-Guided Surgery	FGS
Fluorescent Microsphere	FM
Food and Drug Administration	FDA
Gray-Level Co-Occurrence Matrix	GLCM
Heart Rate	HR
Hemoglobin Concentration	Hb
Hybrid Plug/Flow Compartment	HyPC
Impulse Residue Function	IRF
Indocyanine Green	ICG
Ingress Slope	IS
Linear Time-Invariant	LTI
Machine Learning	ML
Macro Molecular Contrast Media	MMCM
Magnetic Resonance Imaging	MRI
Maximum Intensity	Imax
Methicillin-Resistant Staphylococcus Aureus	MRSA
Microsphere Quantification Using Imaging Cryomacrotome	mQUIC
Near-Infrared	NIR
Optical Coherence Tomography	OCT

Optical Density	OD
Optimal Cutting Temperature Compound	OCT
Oxyhemoglobin Saturation	SaO_2
Patient	Pt
Peak Enhancement	PE
Periosteal Blood Flow	PBF
Phosphate-Buffered Saline	PBS
Positron Emission Tomography	PET
Potassium Hydroxide	KOH
Principle Component	PC
Principle Component Analysis	PCA
Receiver Operating Characteristic	ROC
Region-Of-Interest	ROI
Respiratory Rate	RR
Single-Photon Emission Computed Tomography	SPECT
Small Molecular Contrast Media	SMCM
Staphylococcus Aureus	*S. aureus*
Surgeon's Burden	SB
Surgical Site Infection	SSI
Time-Of-Peak	Tp
Time-To-Peak	TTP
Tryptic Soy Agar	TSA
Tryptic Soy Broth	TSB

Chapter 1

Introduction and Background

This chapter is an introduction and a background explanation of the research topic and objectives of this thesis. The main topic of this thesis is to quantify bone perfusion by analysis of dynamic contrast-enhanced fluorescence imaging (DCE-FI) data. To explain the significance and innovation of the main topic: First, the rationale of this thesis will be stated within the context of the clinical problem, which is surgical site infection (SSI) following lower extremity injury surgery. A detailed description of the cause of SSI in lower extremity injury surgery, patient outcomes following SSI, and current standard of care of SSI will be provided. Second, the knowledge gaps that this thesis seeks to address are highlighted. Those gaps include the uncertainty of the extent of surgical debridement in lower extremity injury surgery, the lack of objective quantification of bone perfusion intraoperatively, and the difficulty in deciding the risk of potential SSI. Corresponding to the main topic, three main research objectives that this thesis will address will be discussed, which include validation of DCE-FI, preclinical fracture contamination model, and surgical debridement guidance using DCE-FI spatial and kinetic features on open-fractured lower extremity.

1.1. Clinical Problem/Rationale

Orthopaedic surgery is one of the most rapidly growing categories of surgical procedures: such procedures are performed 22.3 million times per year, worldwide, and are growing at an annual rate of 4.9% [1]. Orthopaedic surgery can be categorized as upper extremity surgery (hand, elbow, arm and shoulder) and lower extremity surgery (knee, foot,

ankle, thigh and back), corresponding to upper and lower extremity injuries, respectively. Lower extremity injuries are more complex and life-threatening than upper extremity injuries. They account for 32% of all injuries [2], and their main etiologies include falling, motor vehicle collision and military involvement [3]. Timely evaluation and surgical management of lower extremity injuries— especially high-energy injuries—is important, as the morbidity and mortality rates are highly related to the time between injury and treatment. Surgical management includes damage control by vascular ligation and/or vascular shunting, infection control by antibiotics, debridement and irrigation, and fracture management by internal or external fixation.

Postoperative complications of SSI must be considered in orthopaedic surgery, as one of the most challenging postoperative complications, it makes up 15.6% of total postoperative complications [4]. In the United States, there were 110,800 SSIs associated with inpatient surgeries in 2015, 3% annual increase in SSI ratio in 2021, annual cost of $3.3 billion, extended hospital length of stay by 9.7 days, and increased cost of hospitalization by $20,000 per admission [5]. High-energy lower extremity injuries have an even higher incidence of SSI. SSI is strongly associated with residual foreign bodies and/or devitalized bone/tissue, when primary surgical debridement has not been adequate for all injured regions. Failed treatment of SSI will result in increasing morbidity, loss of function and even amputation [6].

1.2. Knowledge Gap

Thorough debridement is necessary in the management of SSIs, and it is the primary step before the establishment of mechanical stability. Inadequate debridement

leaving with residual devitalized bone or tissue will necessitate additional unplanned surgery and prolonged morbidity [6–9]. Microbial biofilm also forms preferentially on these tissues, making antibiotic treatment and immune cell response less effective [10,11]. However, thorough debridement is challenging, for the following reasons: First, devitalized bone or tissue is difficult to spot, because devitalized bone or tissue usually has no obvious outlines from its surrounding vitalized bone or tissue; Second, the clinical judgment of devitalized bone or tissue is rudimentary. The clinical signs, such as color changes, turgidity and "paprika" areas [12,13], are often hard to distinguish under the ambiguous surgical light; Third, obvious clinical signs are not always existing in the surgical sites. Some devitalized bone or tissue are in "gray-regions" that show no obvious clinical signs, making them harder to be recognized [13]. As a result, a functional intraoperative imaging system that can guide amount of tissue to be debrided as well as its precise boundary is needed. The development of this type of imaging system should improve SSI occurrence, treatment and patient outcome.

Intraoperative imaging can leverage tissue perfusion to guide debridement, since perfusion is an important determinant of tissue viability, and perfusion can theoretically be measured intraoperatively using dynamic contrast-enhanced fluorescence imaging (DCE-FI). Specifically in bone, adequate perfusion is essential for maintaining bone activity [14], and deficient perfusion prevents delivery of nutrition and antibiotics, and it accelerates biofilm formation [15,16]. However, there are currently no imaging systems that can quantify bone perfusion intraoperatively. Most of the current systems in imaging bone (*i.e.* plain radiography, computed tomography, and magnetic resonance imaging) have complex systematic components that are difficult to be incorporated in surgical procedures, and

acquiring these images intraoperatively will lead to prolonged operational time. This extensive gap in our understanding leads to substantial variation in extent of debridement, potentially compromising perfusion to the tibia from periosteal tissue. This gap also places patients at unnecessarily high risk for initial osteitis, recurrent infection/osteitis, and osteonecrosis, and therefore increasing possibilities of repeated surgery and decreasing patients' outcome.

1.3. Research Objectives

We propose a fluorescence-guided approach that applies DCE-FI techniques to assess the perfusion of bone, and to provide precise guidance of debridement during lower extremity injury surgery**. Our central hypothesis is: DCE-FI contains perfusion-associated features that enables the prediction of negative outcomes of bone devitalization.** The proposed computational model works by incorporating spatiotemporal, statistical, and kinetic parameters extracted from DCE-FI, and using this information to predict bone perfusion status, with the goal of guiding debridement. By the model, bone needing debridement will be labeled as low perfused regions and have clear margins from well perfused regions, when visualized as a classification map. The proposed model will be a useful debridement guidance tool that has high clinical potential. The thesis work will focus on developing the model from benchtop to bedside (**Figure 1.1**), with the following specific aims:

Aim 1: Validation of DCE-FI with fluorescent microspheres. The first aim is to develop a "gold standard" for DCE-FI. In our pilot animal study [17], we modify the classic fluorescent microsphere (FM) perfusion measurement technique, making it not only

quantitative but also a spatially resolved visualization of perfusion. By the modified FM technique, perfusion can be visualized in 3D as volumetric whole-bone/cortex/marrow perfusion map, by overlaid with different segmented bone structures. In this aim, we will develop this modified FM technique to validate the accuracy of DCE-FI in quantifying bone perfusion. To complete this aim, we will 1) design animal study of administrating FMs and indocyanine green (ICG) into bones with different perfusion levels, 2) use DCE-FI to image the bones, 3) scan FMs with cryo-macotome imaging system and calculate volumetric perfusion maps, and 4) compare the volumetric perfusion maps by FM technique with the predicted perfusion by DCE-FI models.

Aim 2: Correlate DCE-FI with infection risk in rodent Methicillin-resistant *Staphylococcus aureus* (MRSA)- contaminated fracture model. We have previously developed a rodent fracture model that has controlled level of trauma by blast overpressure tube injury. In the second aim, we will further incorporate survival and infection into the rodent fracture model, and correlate the detected contaminated region by bioluminescent imaging with the predicted low perfusion bone region by DCE-FI. We hypothesize that infected regions are more likely to have low post-injury perfusion, and that DCE-FI can guide debridement of tissue most susceptible to infection. To complete this aim, we will 1) introduce low-energy fracture to rodent femur by the blast overpressure tube platform, 2) conduct surgical debridement and stabilization, 3) inoculate bioluminescent MRSA at fracture site, 4) image rodent femur by DCE-FI and bioluminescent imaging during MRSA growth period, and 5) compare multi-modality results and compute the correlation coefficients.

<u>Aim 3:</u> Validate machine learning predictive model on clinical open infection data. Clinical prediction of bone infection is mainly based on patient demographics and preoperative laboratory test results [18], which can only provide patient-wise prediction not region-wise or pixel-wise prediction, and therefore, can only influence surgeon decision slightly. To make region-wise prediction, we will develop a machine learning predictive model based on DCE-FI and validate it on clinical open infection data. Machine learning has been previously utilized in differentiating damaged bones verses normal bones [19] and assessing bone perfusion [20]. In this aim, we will build the machine learning predictive model by including kinetic features, spatiotemporal features and infection risk score [18], and validate its accuracy with multi-site open infection patient data. In detail, we will 1) extract spatiotemporal features and kinetic features by texture analysis and kinetic analysis, 2) calculate patient-wise infection risk score, 3) train machine learning algorithms, and 3) compute classification metrics by comparing with ground truth of confirmed patient outcome from multiple medical centers.

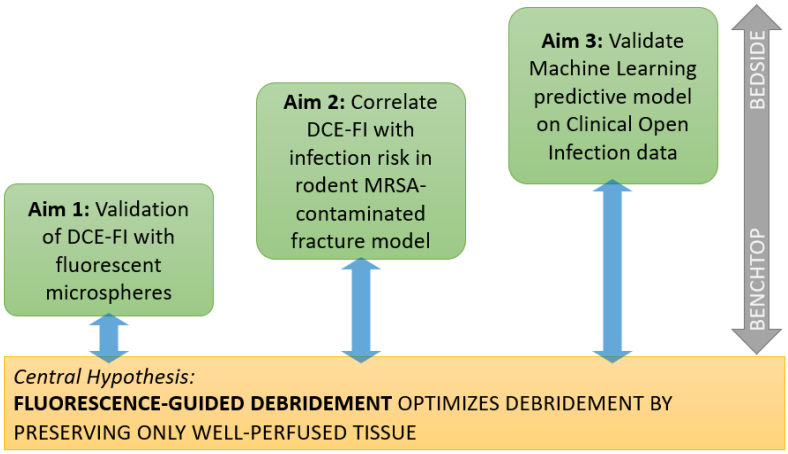

Figure 1.1: Diagram of research objectives in the thesis work.

1.4. Research Significance and Impact

This thesis work has significance and impact both in research and in clinics, as listed below:

Firstly, this thesis work will make predictions for SSI occurrence. SSI is one of the most challenging postoperative complications following orthopaedic surgery, but current prognostic strategies for SSI are inadequate. With the proposed predictive model, the potential of bone infection can be assessed intraoperatively.

Secondly, this thesis work will extend fluorescence-guided techniques by developing them specifically for surgical debridement. In particular, the proposed predictive model will enable the classification of bone tissue regions-of-interest according to different perfusion levels (and other perfusion-associated features), and meanwhile visualize margin between low-perfused regions and other regions. We anticipate that this model will be helpful for surgeons, especially inexperienced ones, whose surgical success rates have the most to gain, and which will in turn improve the outcome and quality of life for patients.

Thirdly, this thesis work advances the ability to quantify bone perfusion intraoperatively. Classical fluorescence-guided surgery (FGS) technique provide only qualitative information, and in contrast, this thesis work further expands the usability of FGS by providing quantitative information such as blood volume and blood flow. This is accomplished by accounting for sources of variation in the delivery of ICG to the tissue region of interest, for example. Such quantitative information can be then used in developing bone-specific kinetic models [19,21] and machine learning models.

Lastly, this thesis work has demonstrated a "gold standard" for validating the measurement of perfusion in orthopaedic research, in principle. The modified fluorescent microsphere technique we have developed using imaging macrotome is a repeatable and valuable perfusion measurement, and it can be applied in both pre-clinical and clinical studies. While we were only able to complete a limited dataset due to challenges accessing the imaging macrocryotome, the technique was demonstrated and results showing the potential of the approach were highlighted.

1.5. Thesis Outline

This thesis consists of eight chapters. The first and second chapters provide introduction, background, and literature review matterial. The following five chapters provide an adaptation of published or ongoing studies that have been accomplished during my graduate work. The final chapter provides a conclusion and discusses where I think future work should focus on. Provided here is a summary of each of the chapters which pertain to the research studies I performed:

1.5.1. Validation of DCE-FI by microsphere quantification technique using custom-built multi-channel cryomacrotome (mQUIC) in rabbit femur (Chapter 3)

Perfusion is important in maintaining normal bone viability, but currently there are no techniques to directly measure bone blood flow rate. Therefore, there is no "ground truth" method for bone perfusion to validate DCE-FI. This chapter summarizes the work from the paper "Validation of dynamic contrast-enhanced bone blood flow imaging technique with fluorescent microspheres", published in *Proc. SPIE 11943* in 2022, by X.

Han, V. Demidov, D. Wirth, B. Byrd, S. C. Davis, I. L. Gitajn, and J. T. Elliott, and the paper "Initial experience of perfusion assessment in a rabbit model of orthopaedic trauma surgery using fluorescent microspheres and hyperspectral imaging cryomacrotome", published in *Proc. SPIE 12146* in 2022, by X. Han, V. Demidov, D. Wirth, B. Byrd, S. C. Davis, I. L. Gitajn, and J. T. Elliott. Here we proposed a modified fluorescent microsphere quantification technique using custom-built multi-channel cryomacrotome, termed as "mQUIC". This technique converted the spatial density of fluorescent microsphere counted in *ex vivo* serial frozen sections into volumetric perfusion maps, and through the use of corresponding color images of the frozen tissue, enabled the visualization of periosteal and endosteal perfusion separately. As a result, mQUIC is a method that can be used as a validation approach for bone perfusion assessment.

1.5.2. Low-energy fractured MRSA-contaminated rodent femur model for correlating DCE-FI with bioluminescent imaging (Chapter 4)

This chapter will expand the application of DCE-FI in bone viability assessment to bone infection assessment. Bone infection associated with fractures is difficult to characterize, due to the complex changes in blood flow and vasculature. This chapter describes a completed work using DCE-FI and bioluminescent imaging to visualize the vascular changes after fracture and bacterial contamination. This completed work will be published in a peer-review journal in the near future. In this study, we developed a low-energy rodent femur fracture model followed by MRSA contamination. DCE-FI imaging were correlated with a longitudinal bioluminescent imaging, providing a multi-modality imaging approach for understanding and monitoring bone infection. As a result, this

preclinical study represents an important first step for any further preclinical and clinical studies in evaluating the DCE-FI in bone infection imaging.

1.5.3. First-pass kinetic parameters and arterial input functions (AIFs) characterization of amputation (Chapter 5)

Model-dependent methods in computing blood flow from DCE temporal curves have been established decades ago, but the required assumptions of physical conditions and location-specific interpretations have limited their applications in broader orthopaedic problems. In addition, intrasubject variations caused by differences in dose and cardiovascular conditions within a patient group were one of main reasons for inaccurate computations. This chapter demonstrates the work from the paper "First pass kinetics of dynamic contrast-enhanced fluorescence imaging in lower limb amputations: model-independent characterization and classification in perfusion states", under review in *Journal of Bone and Joint Surgery* in 2023, by X. Han, J. T. Elliott, Y. Tang, J. S. Sottosanti, A. Hall, S. Jiang, and I. L. Gitajn. In this study, we developed a simplified model-independent method using first-pass kinetic parameters extracted from DCE-FI intensity curves. Meantime, we corrected the intersubjective variations caused by AIF-associated fluctuations using a simple AIF correction method. This work will prove the first-pass kinetic analysis in characterization of amputation degrees, and will accelerate the applications of DCE-FI in bone imaging.

1.5.4. First in-human use of dynamic contrast-enhanced texture analysis for orthopaedic trauma classification (Chapter 6)

Assessing bone viability levels intraoperatively is challenging due to lack of accurate physical measurement. This chapter describes the work presented in the paper "Spatial and temporal patterns in dynamic-contrast enhanced intraoperative fluorescence imaging enable classification of bone perfusion in patients undergoing leg amputation", published in *Biomedical Optics Express* in 2022, by X. Han, V. Demidov, V. S. Vaze, S. Jiang, I. L. Gitajn, and J. T. Elliott. Here we developed an unsupervised machine learning based bone viability level classification approach using spatial and temporal features extracted from DCE-FI human data. In this approach, we used principle component analysis to reduce the feature dimension, and *k*-means clustering algorithm to separate the data into normal/suspicious/compromised groups. This study opened up the possibility of dynamic contrast-enhanced texture analysis in orthopaedic trauma classification.

1.5.5. Risk prediction on orthopaedic trauma patients for fracture-associated infection using DCE-FI (Chapter 7)

Proper surgical debridement is a critical step for preventing SSI. However, currently there are no techniques to predict the risk of SSI and thus to guide the location and degree of debridement. This chapter is based on the work in the paper "Risk prediction on orthopaedic trauma patients for fracture-associated infection using dynamic contrast enhanced-fluorescence imaging" in press in *Proc. SPIE 11943* in 2023, by X. Han, L. M. Bateman, P. M. Werth, S. Jiang, I. L.Gitajn, and J. T. Elliott. Here we presented an SSI risk prediction method using DCE-FI and supervised machine learning. In this method, we extracted three categories of predictive features: spatial, temporal and informatic features.

A combination of these features can not only predict the possibility of SSI, but also provide a three-level predictive map for visual guidance of debridement.

1.5.6. Conclusion and future studies (Chapter 8)

This chapter will summarize the previous five chapters and draw conclusions regarding the main results. Essentially, the above five chapters have developed the assessment and validation approaches in bone viability and bone infection from benchtop to translation, which can provide visual guidance for surgical debridement in orthopaedic trauma surgery. This chapter will tie all of these pieces together, and will also discuss some potential future studies associated with the completed studies, including and model-dependent approach in bone perfusion evaluation, multi-institutional cohort clinical study on guiding open-fracture surgery, and correlating DCE-FI with multiple injury levels for more precise bone infection evaluation.

Chapter 2

Literature Review

This chapter reviews the literature relevant to the topic of this thesis—the development and validation of dynamic contrast-enhanced fluorescence imaging (DCE-FI) approaches for bone perfusion quantification in lower extremity injury surgery. First, the clinical problem—surgical site infection (SSI) following lower extremity injury surgery—will be introduced. A detailed description of the cause of SSI in lower extremity injury surgery will be provided, followed by the challenges in current standard of care. Second, the background related to physiology of bone perfusion will be discussed. Here the reader will understand the importance of perfusion in bone viability, the complex structure of bone vasculature, characteristics of osteomyelitis, and the current methods for measuring bone perfusion. Third, the theoretical basis of dynamic contrast-enhanced (DCE) imaging will be introduced in detail, as DCE imaging serves as fundamental to the approaches developed in this thesis. Here we will describe the history of DCE, theories of tracer kinetic models, and current applications and techniques of DCE imaging. Fourth, an overview of tissue optics, and specifically, fluorescence imaging will be provided. The theory of tissue scattering and absorption, physical modeling of light propagation in tissue, principle of fluorescence and fluorophores will be explained here. Specifically, DCE-FI techniques will be discussed, as it is the imaging modality used in this thesis. Fifth, microsphere dilution theory will be demonstrated, including its specific application in tissue perfusion quantification. Last, machine learning classification theory and its application in bone imaging will be addressed. Detailed descriptions involve theoretical basis, texture analysis and prognosis models.

2.1. Issues in Orthopaedic Trauma

2.1.1. Clinical presentation

Orthopaedic trauma surgery includes lower extremity (knee, foot, ankle, thigh and back) surgery and upper extremity (hand, elbow, arm and shoulder) surgery. The annual number of orthopaedic surgical procedures is 22.3 million worldwide, and the annual growth rate is 4.9% [1], making it one of the most rapidly growing categories of surgical procedures. In the United States, approximately 7.9 million musculoskeletal injuries are reported each year, with 5-10% of which ending in delayed or impaired healing [22]. Trauma costs nearly $56 billion per year for health care, making it the second most expensive medical problem in the US, just after heart disease [23]. Of all reported orthopaedic trauma patients, 22% of them suffer severe injuries, and 33% of them have moderate injuries. The overall mortality rate is 4.39%, with largest number of deaths caused by fall-related injuries (44.2%), motor vehicle accidents (26%) and firearm injuries (15.3%) [24].

In orthopaedic trauma surgery, one of the common types is lower extremity injury that accounts for 32% of all injuries [2]. In 2012, there are approximately 278,100 lower extremity injuries in the US [25]. Common causes for lower extremity injury include falling, motor vehicle collision and military involvement [3]. Most severe civilian extremity injuries are caused by blunt trauma, and then by penetrating or combined mechanisms. In contrast, most military extremity injuries are due to penetrating or combined mechanisms that have high rates of open fracture and vascular injury [3,26]. Lower extremity injuries are limb-threatening and even life-threatening. Severe lower extremity injuries are associated with a high incidence of complications, including wound

complications such as infection, necrosis, nonunion and osteomyelitis, venous thromboembolism, rhabdomyolysis, and late complications such as amputation and heterotopic ossification in residual limbs [3]. These complications following lower extremity injuries will result in prolonged hospitalization and additional operative treatment [27]. Mortality of civilian extremity injury ranges from 5 to 10 percent, and is greater in blunt injuries than in penetrating injuries [28].

Postoperative complication is one of the most challenging issues in orthopaedic surgery, especially when dealing with high-energy lower extremity injury. SSI makes up 15.6% of total postoperative complications [4], and is one of the most severe complications. In 2009 in the US alone, annual incidence of SSI in all surgical categories is 1.07%, along with annual deaths of 8,000 and financial cost of treatment of $10 billion [29]. The main causes of SSI are incomplete primary surgical debridement, leaving behind residual foreign bodies and/or injured tissue. SSI will result morbidity, loss of function and amputation [6]. This thesis work will focus specifically on the critical issue of optimizing debridement so that it is thorough and leaves the patient with the least likelihood of infection.

2.1.2. Challenges in current standard of care

Current evaluation of lower extremity injuries consists of four functional components—nerves, vessels, bones, and soft tissues—that must be evaluated both individually and in combination. The injury is a mangled extremity if any three of the four components are injured [30]. To achieve the best outcome, limb salvage can be attempted even if the patient has a mangled extremity, or primary amputation is required if the injury level is so severe.

The goal of surgical management is to restore the limbs for maximum function. Surgical management of lower extremity injuries includes damage control by vascular ligation and/or vascular shunting, infection control by antibiotics, debridement and irrigation, and fracture management by internal or external fixation [6–9]. Thorough debridement of foreign body and devitalized tissue is necessary in the management of SSIs, and it is the primary step before the other mechanical maintenance [6–9]. In debridement surgery, clinical judgment of devitalized bone or tissue is based on the clinical signs, such as color changes, turgidity and "paprika" areas [12,13]. However, these clinical signs are often hard to distinguish under the ambiguous surgical light, and some devitalized bone or tissue are in "gray-regions" that do not display obvious clinical signs [13]. Therefore, the risk of debriding too much or too little is high due to lack of objective measurement tools of bone perfusion, especially on the "grayish regions" that don't satisfy all clinical signs. In other words, debridement is currently performed 'blind'—while the goal of debridement is to improve the overall perfusion of tissue remaining in the patient by removing poorly perfused tissue, there is no currently used method to confirm this has been accomplished.

2.2. Physiology of Bone Perfusion

2.2.1. Importance of perfusion in bone viability

Perfusion characterizes blood flow at the level of the capillary bed. Why is perfusion critical for keeping bone viable? Generally, for both bone and soft tissue, adequate perfusion is essential for repair and healing of fracture, prevention of secondary fractures, management of infection following trauma, maintenance of bone growth and strength, and delivering oxygen, nutrients, antibiotics, immune cells [14,31–37]. In contrast,

deficient perfusion prevents the delivery of antibiotics and endogenous immune cells to traumatized bone, becomes a site of biofilm formation, and resists antibiotic effects [15,16]. Inadequate perfusion will result in tissue and organ dysfunction, which associated with chronic conditions including hypertension, obesity, diabetes mellitus and dyslipidemia [38]. Regulation of tissue perfusion is done by microcirculation, where stand 70% to 90% of the systemic arterial pressure and offer the main resistance to flow of blood [39].

As for bone specifically, first, poor bone perfusion is associated with complications including infection, necrosis, functional deficits [40–42]. If a bone is poorly perfused, it is likely that it becomes devitalized. Residual devitalized bone or tissue will require additional unplanned surgery and prolonged morbidity [6–9]. Microbial biofilm will also form on them, making antibiotics treatment and immune cell response even harder [10,11]. Failure of proper treatment in devitalized bone will lead to significant loss of bone function, increased risk of recurrent infection and repeat surgery, prolonged morbidity, reduced quality of life, and conversion to amputation [43–46]. Second, perfusion is also crucial for bone remodeling and healing. Inadequate perfusion in bone remodeling is associated with increased risk of fracture and avascular necrosis [47]. Third, reduced bone perfusion is related to skeletal diseases, such as osteoporosis [48] and osteoarthritis [49].

2.2.2. Structure of bone vasculature

As discussed in section 2.2.1, blood vessels function in transporting and maintaining homeostasis of bone. Bone vasculature is a complex and heterogenous system (**Figure 2.1**). Distinct vessel subtypes consist of bone vasculature, and differentially regulate osteogenesis, hematopoiesis and disease conditions in bone [50]. Similar to other

tissues, bone vasculature consists of arteries and veins, and connected through capillary network. In longbones such as tibia and femur, arteries can be separated as periosteal arteries surrounding the bone, and endosteal arteries (including principle nutrient artery and Haversian arteries) penetrating the bone. Periosteal system supplies the outer one-third of the cortex, and endosteal system supply the medulla and inner two-thirds of the cortex. Capillary vessels fill the marrow cavity, and are mostly linear columnar arranged. The main capillary network connects with a large central vein, where other smaller veins are drained separately by epiphyseal capillaries.

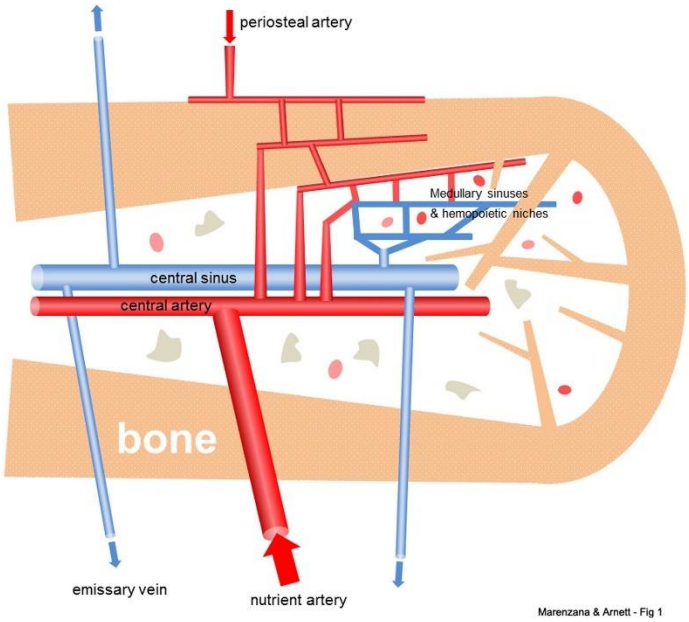

Figure 2.1: Schematic diagram of bone vascular supply. One or more nutrient arteries are the main blood supply, which penetrate the medulla. Smaller periosteal arteries supply the cortex and connect to the nutrient arteries. The arterial branches drain into arterio-venous sinuses in the medulla. Image from [14]. Reproduced with permission from Springer Nature.

2.2.3. Characteristics of osteomyelitis

Osteomyelitis is an inflammatory process caused by infecting microorganism. *Staphylococcus aureus* (*S. aureus*) is the most common pathogenic microorganism. *S.*

aureus can attach to extracellular matrix protein to adhere the host tissues, evade from host defenses by emitting some toxins, attack host tissues or degrade components of extracellular matrix, and colonize tissues and persist after bacteremia [51]. *S. aureus* can also form biofilms, which is a structured microbial community. Once *S. aureus* attaches to the bone tissue, the bacteria begin to accumulate and produce a sticky matrix of initial biofilm. This accumulation results in the formation of biofilm microcolonies and development of mature biofilm. The biofilm may then finally break down and release the bacteria from within, causing contamination throughout the host [52,53]. As a result, biofilms are difficult to treat with antimicrobial agents, and create a diffusion barrier to inhibit the penetration of nutrients.

Osteomyelitis can involve a single or several regions of the bone, including marrow, cortex, periosteum and soft tissue. Infection can happen after trauma, surgery or joint replacement, and then can spread locally from the initial infection source. Acute osteomyelitis usually develops over several days or weeks, and chronic osteomyelitis evolves over months or years. In chronic osteomyelitis, persistence of microorganisms, low-grade inflammation, and the presence of dead bone and fistulous tracts are characteristics of the disease [54,55].

In osteomyelitis, the infected regions have acute suppurative inflammations where microorganisms are embedded. The inflammation, along with leucocytes, contribute to tissue necrosis and bone structure destruction. Moreover, blood vessels are compressed and occluded by the inflammation in tissue, leading to ischemia and bone necrosis. Necrotic bones without blood supply can become separated and extended to form sequestra, letting microorganisms grow within and becoming resistant of antibiotic treatment. At the

infarction edge, there is reactive hyperemia and increased osteoclastic activity that leads to bone loss and osteoporosis. Bone apposition also occurs, causing periosteal apposition and new bone formation [54,56].

2.2.4. Current methods for measuring bone perfusion

Focusing on the critical parameter of 'perfusion' as the implicit or explicit goal of any debridement procedure, we now turn to a discussion of the current methods for measuring perfusion in bone. Quantitative measurement of bone perfusion is important in various clinical conditions such as infection, trauma, inflammation, arthritis, avascular necrosis neoplasms, and bone grafting [57].

Various non-invasive techniques are used for clinical measurement of tissue perfusion, such as Doppler flow probe [58] and transit time flow measurement probe [59]. Monitoring tissue perfusion can be done by looking at biomarkers of global tissue perfusion including serum lactate and central venous oxygen saturation, assessment of non-vital organ perfusion, and direct visualization of sublingual microcirculation [60]. Ideally, measurement of tissue perfusion should be rapid, non-invasive and user-friendly.

For measuring perfusion in bone, angiographic imaging techniques are routinely used in the clinic [61]. Different preoperative imaging modalities can improve surgical strategies in many aspects, including early detection, improving diagnostic accuracy and operative staging and planning [62]. Plain film radiography doesn't have sufficient sensitivity [63]. Magnetic resonance imaging (MRI) is capable of diagnosing very early lesions, and has a very high sensitivity and specificity (more than 90%). MRI detects bone marrow changes more readily than other than bone changes [64,65]; however, MRI is

expensive and not always available at smaller hospitals. Single-photon emission computerized tomography (SPECT) can detect vascular integrity, focus avascular regions on early lesions. SPECT also has high sensitivity and high resolution [66,67]. Computed tomography (CT) has high spatial resolution and contrast resolution. CT can detect morphologic features. However, CT cannot visualize early vascular and marrow abnormalities [68,69]. Planar scintigraphy has been reported to have a moderate sensitivity. Quantitative bone scan using planar scintigraphy allows quantitative analysis of perfusion and static phases, but it is still under investigation and not widely used clinically [66,70].

Specifically, MRI has strengths in providing carriable soft tissue contrast related to the inherent T1 and T2 relaxivities of the tissue. Both cortical and trabecular bones can have excellent contrast by MRI [71]. Current techniques of MRI incorporate contrast media, including small and macro molecular contrast media, into MRI to allow for assessment of angiogenic activity and estimation of physiological parameters including permeability, blood flow and clearance rates. Positron emission tomography (PET) acquire quantitative information about the localization and metabolism of tissues by injecting radiotracer. A specific radiotracer, ^{18}F-Fluoride, is Food and Drug Administration (FDA) approved bone seeking radiotracer that can bind to hydroxyapatite in the bone matrix [72]. Dynamic PET time-activity curves can be used to analysis the behavior of ^{18}F-Fluoride, demonstrating differentiation of bone blood flow in the angiogenic phase from bone mineral binding and bone formation in the osteoblastic phase [57].

In section 2.3, the technique proposed in this thesis to measure bone perfusion—mainly, DCE-FI—will be further discussed. In the subsequent section, however, the general principles of dynamic contrast-enhanced imaging, which are relevant to a number

of different modalities such as CT and MRI, will be thoroughly discussed to provide the most comprehensive foundation for understanding the specific fluorescence-based technique that has been developed in this work.

2.3. Dynamic Contrast-Enhanced Imaging

2.3.1. History of DCE

Dynamic contrast-enhanced imaging is based on indicator dilution theory that describes the kinetic behavior of the indicator diluted into the circulatory system. The first study of indicator dilution theory was done in 1761, where an indicator was injected into the vena cava to compare pulmonary circulation times [73,74]. In 1824, indicator dilution theory was further developed to measure blood flow, cardiac output, and central blood volume [73]. The first attempt for measuring cerebral blood flow (CBF) was done by utilizing the highly diffusible gas nitrous oxide as a blood flow tracer, and measuring the time-varying concentration of nitrous oxide in arterial blood and venous blood samples from the jugular bulb [75]. After that, radiolabeled ^{85}Kr replaced nitrous oxide and assessed regional CBF by placing scintillation counting devices at various locations on the scalp [76]. The measurement of blood flow was further improved by using radioactive ^{133}Xe, modifying three tissue compartment equation, and determining noninvasively the arterial input function (AIF) [77]. Later, after the indicator dilution theory was corrected by taking account recirculation, it became a reliable method of characterizing the vascular dynamic of tissue [78].

Later on, along with the development of multiple imaging modalities, indicator dilution theory has been combined with imaging techniques and developed as DCE

imaging, including DCE-Ultrasound (US), DCE-MRI, DCE-CT and DCE-FI [79,80]. In DCE imaging, contrast agent works as indicator of blood behavior, and therefore its kinetic distribution and signal enhancement patterns can reflect several hemodynamic features including regional blood flow and vessel density [81]. The first tomographic method of quantifying blood flow used DCE-PET and $H_2{}^{15}O$ [82]. Theoretical groundwork for DCE-CT was published in 1980 that implemented a sequence of scans following an intravenous bolus injection of contrast agent to determine CBF [83]. These past historical works have built foundations for the recent imaging and analytical techniques on DCE in blood flow measurement.

2.3.2. Overview of current DCE applications and techniques

Dynamic contrast-enhanced imaging acquires a series of images over time after an intravenous bolus injection of contrast agent, and refer to baseline images without contrast enhancement. The presence of contrast agent within regional blood vessels and tissues reflect as signal enhancement in a linear or non-linear manner. Analysis of the temporal changes in signal enhancement from the time-concentration curves can quantify physiological parameters reflecting the status of vascularity and adjacent tissues. By fitting specific compartment model, the pharmacokinetics of contrast agent during the first-pass circulation can represent perfusion, relative blood volume and mean transit time.

In general, DCE imaging has become increasingly applicable to several clinical and research problems, such as tumor imaging [84,85], vasculature imaging [86,87], perfusion measurement [88,89] and malignance determination [90,91]. In clinics, DCE imaging gain increasing popularity as the imaging protocols are easily implementable in standard clinical

settings [81,92], and several contrast agents have certificated for clinical use [93–95]; In research, DCE imaging systems are also promising because they have high spatiotemporal resolution, wide availability and reasonable cost, and thus making them suitable for studies such as antiangiogenic therapy and complex physiological models [96].

Multiple imaging modalities have leveraged DCE, including DCE-CT, DCE-MRI, DCE-FI and DCE-US [80,97]. DCE-CT uses contrast agent nonionic iodine for contrast acquisition. DCE-CT has main advantages of simplicity in terms of image acquisition and processing, linear relationship between contrast agent concentration and signal attenuation, wide availability, low cost and high spatial resolution. DCE-CT can be incorporated into CT angiography, and can be integrated into PET/CT system that enables tumor vascularity and glucose metabolism to be simultaneously evaluated [98]. DCE-MRI uses contrast agent gadolinium. The changes in MRI signals are non-linear. DCE-MRI can be acquired using either T_2* or T_2 weighting (known as T_2 weighted DCE-MRI or dynamic susceptibility contrast MRI) or T_1 weighting (known as T_1 weighted DCE-MRI).

Among those techniques, DCE-FI has gained the fastest growth in clinical applications, including cancer imaging, sentinel lymph nodes imaging, neurological diseases, cardiovascular diseases, skeletal processes, ureter imaging and bile-duct imaging [99–111]. DCE-FI outstand others in clinical acceptance with the following reasons: Ultrasonography cannot incorporate targeted contrast agents to apply precise visualization. It also induces ionizing radiation and direct dose to patients and surgeons; MRI and CT are complex and costly, and predominantly used preoperatively [112]; PET and SPECT are sensitive to deep depth but have low contrast and cannot take real-time imaging [113,114]. In contrast, fluorescence imaging uses near infrared (NIR, wavelength ranges 700-900 nm)

contrast agents that have high sensitivity to targets below the surface, are safe without ionizing radiation, are invisible so won't interfere with the surgical field, and are capable of visualizing tissue in real time [112]. In summary, NIR fluorescence imaging will increase surgical accuracy and decrease postoperative morbidity.

2.3.3. Tracer kinetic modeling: review of theory

Tracer kinetic modeling is an approach of measuring tissue blood flow, and it has been widely used in DCE imaging to obtain quantitative parameters. Tracer kinetic modeling is based on linear time-invariant (LTI) system theory. In detail, a tissue region-of-interest (ROI) can be treated as an LTI system. Following an ideal bolus injection of dye approximating a Dirac delta function input, the response of the system will characterize the hemodynamics of the tissue [115]. In this context, the dye acts as a blood flow tracer. The transport of the dye through the microvasculature of the tissue can be described by constructing a kinetic model and applying it to time-dependent measurements of the dye concentration. In LTI system, the dye concentration of tissue ROI, $Q(t)$, is given by the convoluted tracer kinetics [115]:

$$Q(t) = C_a(t) * FR(t) \tag{2.1}$$

Where $C_a(t)$ is the time-dependent concentration of dye in the arterial system (*i.e.* AIF), F is the volumetric blood flow, and $R(t)$ is the impulse residue function (IRF). IRF is defined as the fraction of dye remaining in the system at time t. Both $Q(t)$ and $C_a(t)$ can be extracted directly from DCE fluorescent video data.

There are two main solutions to the above equation. First one is deconvolution method (as known as nonparametric analysis). In this method, no explicit assumptions

regarding the tracer and the compartments is required. However, this method is mathematically difficult, requiring long computational time, and sensitive to system noise. Second solution is nonlinear lest squares. Here the function *FR(t)* can be estimated by minimizing:

$$\|Q_i(t) - F_i C_a(t) * R_i(t)\|^2 \tag{2.2}$$

Where $Q_i(t)$, F_i, and R_i is the *i*th pixel from the DCE fluorescent video. This method is also highly susceptible to experimental noise.

Various tracer kinetic models all follow the same LTI theory, but the main variation among those is how to approximate *R(t)* (**Table 2.1**). *R(t)* is the fundamental function describing the tissue hemodynamics. In general, *R(t)* can be regarded as a sum of $R_v(t)$ (**Table 2.1, Column 2**) which is for vascular phase and $R_p(t)$ (**Table 2.1, Column 3**) which is for extravascular phase, and different models have different expressions of $R_v(t)$ and $R_p(t)$. Among all the models, Tofts model [90] is the simplest one, with an assumption of negligible vascular phase. Extended Tofts model [116] is an expansion of Tofts model, and it allows for the separate estimation of vascular and extravascular phases. The adiabatic approximation to the tissue homogeneity (AATH) model [117,118] describes the vascular phase as plug-flow system and the extravascular phase as a well-mixed compartment, and assumes that the vascular-extravascular exchange only occurs at the capillary end. AATH model accounts for the fact that the dynamics in the vascular space in much faster than in the extravascular space. The two-compartments exchange model assumes the vascular space as a well-mixed compartment [119].

Table 2.1: Vascular and extravascular response functions for various compartment models. Adapted from [120]. Reprinted by permission from Schabel, M.C. A unified impulse response model for DCE-MRI. Magn Reson Med, 68: 1632-1646. Copyright © 2012 Wiley Periodicals, Inc.

Model	$R_v(t)$	$R_p(t)$
Tofts	0	$(\frac{K^{trans}}{F})e^{-k_{ep}t}$
Extended Tofts	$(\frac{v_b}{F})\delta(t)$	$(\frac{K^{trans}}{F})e^{-k_{ep}t}$
AATH	$1-\theta(t-t_c)$	$Ee^{-k_{ep}}(t-t_c)\theta(t-t_c)$
Two compartment exchange	$(1-E_+)e^{-t/T_{-1}}$	E_+e^{-t/T_+}

2.3.4. DCE in assessing bone perfusion

In this section, we will discuss the techniques of DCE-MRI, DCE-PET and DCE-FI in assess bone perfusion.

Dynamic contrast-enhanced MRI use small (SMCM) or macro (MMCM) molecular contrast media, and the extraction of perfusion-related physiological parameters is dependent on the size and binding affinities of the contrast media. In SMCM, contrast media has molecular weight of approximately 538 Da and clearance time of 12 minutes [57]. SMCM based DCE-MRI has been applied in studying osteoarthritis [116], bone marrow lesions [121], osteoporosis [47] and osteonecrosis [122]. In SMCM DCE-MRI, T_1-weighted time-intensity curves for each voxel in the field of view are analyzed using tracer kinetic modelling, so that physiological perfusion parameters in bone can be quantifying from signal intensity. In MMCM, contrast media has molecular weight of approximately 92,000 Da and clearance time of 3 hours. Due to the large molecular weight, MMCM yields flow-independent estimates of permeability surface area product, plasma volume, and fractional leak rate [123]. Because MMCM only accumulates in areas with increased vascular permeability, and quantitative measures of permeability are not subject to contributions from flow. Therefore, MMCM DCE-MRI has great potential in studying

advanced states of osteoarthritis where intraosseous pressure is increased [124]. In MMCM DCE-MRI, two-compartment tracer kinetic models are used, as the reflux rate from the extravascular extracellular space to the plasma space is negligible [123].

Dynamic contrast-enhanced PET using ^{18}F-Fluoride can assess bone blood flow. Complete extraction of ^{18}F-Fluoride during the first few minutes after infection can reflect bone blood flow, and ^{18}F-Fluoride binding to hydroxyapatite in the bone matrix at the time of maximal uptake can demonstrate bone turnover [57]. Analysis methods of ^{18}F-Fluoride DCE-PET use the three-compartment tracer kinetic models [125]. The accuracy of ^{18}F-Fluoride DCE-PET in bone blood flow measurement has been validated with $H_2{}^{15}O$ PET [126,127].

Theoretically in DCE-FI, the dynamic indocyanine green (ICG) inflow/outflow curves were found to be respectively proportional to superficial (periosteal)/deep (endosteal) blood flows using a specific bone blood flow model [37]; Kinetic analysis using the faster early component (early bone perfusion) and the slower late component (late bone perfusion) of the dynamic ICG fluorescence curve can quantitatively measure bone perfusion from both periosteal and endosteal sources, with predictable and reproducible changes after debridement [14,15].

2.3.5. Tracer kinetic models of bone perfusion

When applying tracer kinetic models to bone, special consideration is needed because the blood supply system in bone is more complex than other tissue types. Therefore, an appropriate bone-specific kinetic model should exhibit two criteria: First, the difference in arrival times of dye in the periosteum and endosteal compartment; Second, the porous

nature of endosteal vessels which freely exchange material with the medullary cavity of the bone [21]. Hybrid plug/flow compartment (HyPC) model [21], developed by Dr. Elliott and our research team, applies specifically to the bone periosteal/endosteal perfusion system and fulfills both criteria. HyPC model separates the periosteal and endosteal components and articulates the slow-flow component of the endosteal medullary cavity. HyPC model represents the superposition of a plug flow model in periosteal compartment (P), and has a two-compartment model in endosteal compartment (E), with independent bolus arrival time. The time-dependent tissue concentration of dye, $Q_P(t)$ and $Q_E(t)$ represent the periosteal and endosteal compartments, respectively. In the HyPC model, the time-dependent bone tissue dye concentration $Q(t)$ can be considered a summation of partial volumes of $Q_P(t)$ and $Q_E(t)$:

$$Q(t) = d_P Q_P(t) + d_E Q_E(t) \tag{2.3}$$

Where d_P and d_E are the fractional volumes. In practice, it is not always possible to determine the d_P and d_E, so we use periosteal blood flow (*PBF)* and endosteal blood flow (*EBF)*, for a specific imaging geometry and assumed partial volume distribution. Then $Q(t)$ is given by:

$$Q(t) = \left[PBFR_p(t) + EBFR_e(t)\right] * C_a(t) \tag{2.4}$$

Where *PBF* is the instrument-independent periosteal blood flow, *EBF* is the quantitative endosteal blood flow, $C_a(t)$ is the arterial input function, and $R_p(t)$ and $R_e(t)$ are the IRFs in periosteal and endosteal, respectively, which are defined as:

$$R_p(t) = \begin{cases} 0 & t < T_p \\ 1 & T_p < t < T_p + M_p \\ 0 & t > T_p + M_p \end{cases} \tag{2.5}$$

$$R_e(t) = \begin{cases} 0 & t < T_e \\ e^{-k_2(t-T_e)} & t > T_e \end{cases} \tag{2.6}$$

Where T_p is the arrival time of the bolus to the periosteal vasculature centered, M_p is the minimum time required for dye to travel across the periosteal vasculature, and T_e is the arrival time of the bolus to the endosteal vasculature in the area of interrogation.

Model-dependent and model-independent methods of DCE-FI quantitative analysis can provide necessary clinical information about bone, such as blood flow and blood volume. However, there are some limitations [128] in both methods: First, an explicit model, like the HyPC model or other models such as the AATH model, extract physiologically-meaningful parameters regardless of the sufficiency of the fit or the veracity of its interpretation. Interpretations of these data might be location-specific and pathology dependent. Second, model-independent approaches such as physiologically-constrained deconvolution [129] assume, among other things, that the vascular unit represented in a pixel or ROI have a single arterial input and single venous output—a constraint violated by the overlapping nature of endosteal and periosteal blood flow contributions. Third, inter-subject variations caused by dye injection dose and rate, patient cardiac and circulation conditions, or human artifacts haven't been addressed much yet.

2.4. Microsphere Dilution to Measure Perfusion

2.4.1. Introduction to microsphere techniques

As discussed in the previous three sections, multiple imaging modalities and instruments can measure tissue perfusion by different physical quantities. However, they are indirect measurements, and there is no 'gold standard' for validating the measurements. To establish a reliable and accurate perfusion measurement, microsphere technique with radioactive label has been first introduced in 1967 [130]. Radioactive microsphere

technique was further improved to ensure the microsphere well-mixing [131], to optimize the size and minimum injected number [131,132], and to reach 13.2% difference against molecular tracer [133]. However, radioactive microspheres are toxin and unsafe, which has encouraged the development of fluorescent labels. Fluorescent microsphere (FM) technique was first introduced in 1993 [134]. FM has similar accuracy with radioactive microspheres [134], but it is less expensive, safer, and better retention of label [135].

Microsphere technique is based on the fundamental hypothesis that the number of microspheres within one region is proportional to the blood flow in the region. However, there are several assumptions [136] for this hypothesis to hold true: 1) Microspheres must be well mixed and evenly distributed within the blood stream so that the concentration in all arteries is equal; 2) Microspheres are complete entrapped during the first circulation, and remain entrapped until counted; 3) Blood supply to organ(s) of interest is single; 4) Microsphere distribution should approximate red blood cell distribution; 5) Injection and entrapment of microspheres must have no effect on physiology.

Established protocol of microsphere technique is based on the measurement of blood flow to reference organ [137], and minimum of 400 microspheres are injected per tissue piece. 10-15 micrometer diameter polystyrene beads are injected into the animal's atrium or left ventricle from where they are distributed in the central circulation. Then microspheres are then entrapped on the first pass in the capillaries of the tissues. Then the tissue samples are removed from euthanized animal and counted the number of microspheres within the tissue samples as relative perfusion. To convert the measured relative perfusion to absolute perfusion, a reference arterial blood sample is withdrawn at

a constant known rate R (ml/min) during the microsphere injection. Then the blood flow to piece i, Q_i (ml/min), is given by:

$$Q_i = N_i / N_{ref} \times R \tag{2.7}$$

Where N_i is the number of microspheres counted in the piece i, and N_{ref} is the number of microspheres counted in the reference blood sample.

2.4.2. Fluorescence microspheres for tissue perfusion quantification

Traditional microspheres methods use radioactive-labeled microspheres. Radioactive-labeled microspheres do not need to be physically recovered but can be measured *in situ* using a scintillation counter [138]. In contrast, FMs work on the same principal as radioactive-labeled spheres, but tissue samples containing entrapped FMs need harvest and digestion, and the number of FMs is measured by fluorimetry after filtration. Regardless of the above limitations, FM techniques have become more prevalent in recent years. FM techniques have several crucial advantages: Firstly, FMs are safer and contain no ionizing radiation. Secondly, blood flow in other organs can be determined simultaneously in a single measurement. Thirdly, comparisons between different physiological conditions can be achieved by injecting multiple color microsphere species.

As FM technique has been improved and investigated in multiple pre-clinical models, it becomes one of the most reliable methods to measure organ's perfusion, and it is a primarily used tool to validate new imaging modalities and techniques. Early evaluation of microsphere techniques as tissue perfusion quantification included correlating colored microspheres with radioactive microsphere [137], and correlating with CT measurement [139]. Until recently, FM technique has been accepted as standard

technique in multiple organ perfusion studies [138,140–143]. As for bone perfusion quantification, FM techniques have been applied in several animal models including chicken [144], mice [145], rabbits [146] and rats [147]. In summary, FM techniques have proven to be valid in bulk tissue perfusion quantification.

2.4.3. Fluorescence microspheres and cryo-imaging

Application of FM techniques has bloomed since the incorporation with cryo-imaging. Traditionally, the method of counting microspheres within tissue piece is by measuring the fluorescent intensity from digested microspheres. However, this method can only provide numerical values but lacks information about how microspheres distribute within the tissue volume. Compared to the traditional method, cryo-imaging can improve quantitative analysis and spatial visualization of FMs in the following three ways: Firstly, the digestion of solid tissue sample is skipped. FMs in tissue samples are counted directly by cryo-imaging rather than being estimated indirectly by fluorescence intensity. Secondly, the step of measuring tissue volume can be placed at the end of analysis instead of at the beginning. Thirdly, the process of measuring the number of microspheres is completely automated, and therefore it can avoid manual errors. Lastly, cryo-imaging can produce a 3D volumetric spatial density map of FMs, which enhance the visualization of tissue samples with complex structures.

Cryo-imaging system has been firstly introduced to FM techniques in 2000 [148], and it can specify the location of microspheres deposited in the tissue volume. Therefore, cryo-imaging system can further expand the usability of FM techniques by visualizing the spatial distribution of perfusion with high quality and high speed. The high correlation of

measured perfusion by cryo-imaging system with traditional microsphere counting has been validated in small animals [149]. In this thesis, we used a whole-body multi-channel hyperspectral fluorescence cryo-imaging system [150]. This system acquires densely-sampled spectra at each pixel in the 3D stack, and has high sensitivity in FM detection and more specific measurements. During image acquisition, frozen tissue sample is held fixed with respect to the camera and is advanced along the *z*-axis for serial sectioning. Then hyperspectral image stack has formed from the acquisition sequence, which can then be processing and volumetric rendering to recover the 3D structure. Therefore, FM techniques with cryo-imaging is a promising tool of perfusion quantification and visualization.

2.5. Theoretical Overview of Tissue Optics in Fluorescence Imaging

Leaving for a moment the methodology related to perfusion imaging and measurements, discussed in the previous section, the remaining part of this chapter will focus on the use of optical techniques to characterize the properties of tissue, including its perfusion-related or 'dynamic' (also called kinetic) properties. Therefore, it will be necessary to build a foundation of understanding with respect to the interaction of light with tissue, since the signal used to characterize the clinically relevant parameters of perfusion arise physically from the interaction of light with endogenous and exogenous molecules.

2.5.1. Tissue light scattering and absorption

When light shines on tissue, it will penetrate, scatter, absorb or reflect by tissue. These processes are determined by both the energy of the light and the optical properties

of the tissue. In the settings of medical imaging, it is important to understand how tissue interacts with light for both diagnostic and therapeutic applications, especially in optical imaging system design, image processing and interpretation, and therapeutic planning. In this section, the optical properties of tissue will be discussed. Tissue optical properties mainly include the absorption coefficient μ_a (cm^{-1}) and the scattering coefficient μ_s (cm^{-1}), which sums up to be the total attenuation coefficient μ_t (cm^{-1}):

$$\mu_t = \mu_s' + \mu_a \tag{2.8}$$

As for the scattering properties, μ_s' is the reduced scattering coefficient. μ_s' incorporates the scattering coefficient, μ_s, and the anisotropy factors, g, and is defined by $\mu_s' = (1-g)\mu_s$. The anisotropy factor g characterized tissue scattering in terms of the relative forward versus backward direction of scatter, and is defined as $g = <\cos\theta>$ where θ is the deflection angle of scatter. As a result, μ_s' can be regarded as an effective isotropic scattering coefficient that represent the cumulative effect of several forward-scattering events.

As for the absorption properties, absorption is the process of extracting energy from light, and it occurs when the photon wavelength matches the tissue's energy. There is a linear relationship between light absorbance and concentration of absorbing object, described by Beer-Lambert Law:

$$A = \varepsilon \mathrm{Cl} \tag{2.9}$$

Where A is the absorbance of light, and is defined as $A = -\log(T) = \log\left(\frac{I_0}{I}\right)$. T is the light transmission of the object. I_0 is the incident intensity and I is the transmitted intensity. ε ($M^{-1}cm^{-1}$) is the molar absorption coefficient of the object, and is given by $\varepsilon = \frac{\mu_a}{N_a}$. C (M) is the is molar concentration of the object. And l (cm) is the optical path length. Therefore,

according to Beer-Lambert Law, the concentration of the object can be measured by the light absorbance.

2.5.2. Light propagation modeling in tissue

The above section discussed light-tissue interaction macroscopically, and this section will discuss it microscopically. In nano-meter scales, light movement in tissue can be modelled in multiple ways [151]. Firstly, if light is treated as ballistic photons, each with a direction of travel that can be redirected by scattering used in Monte Carlo simulation. Monte Carlo simulation launches photons into a scattering medium and propagates the photons according to probability density functions for the step size between photon/tissue interaction sites and the angles of deflection. Secondly, if light is treated as a concentration of optical energy that diffuses down a concentration gradient using diffusion theory simulation, Diffusion theory assumes that the quantity that is diffusing does not have a preferential direction of travel and is down a concentration gradient. Diffusion theory also assumes that photons are able to participate in a random walk and thus photons should be able to undergo several scattering events before get absorbed. However, diffusion theory is not good near sources, and not good in tissues with strong absorption where $\mu_s\,(1-g)/\mu_a > 10$.

As discussed above, light will attenuate in tissue and the attenuation is increased with depth. Therefore, design of fluorescent imaging system should consider how light propagate in both tissue and air. In order to deliver enough light, the tissue penetration depth will need to be larger than the depth of tissue. As a result, one key element of fluorescent imaging system is the fluorescence excitation light. The fluence rate (the

number of photons illuminating a unit surface over time) should be maximized while keeping human exposure and photochemical bleaching low [152]. On the other hand, light distortion and attenuation in light should also be accounted in selecting the optics in fluorescent imaging system. Optimized optics specifically for NIR light can overcome the light propagation issue in air.

2.5.3. Principles of fluorescence

The technique described in this thesis makes use of fluorescence imaging. Knowing how fluorescence works is essential for the designs of experimental and analytic methods for this thesis. Fluorescence is a particular form of light that includes near ultraviolet, visible, and near infrared light. Fluorescence occurs when light apply to a molecule, and then the molecule absorb energy from light photons, and at the end emits light photons as it returns to its ground state. This energy conversion is explicitly described in Jablonski diagram. Specifically, the molecule absorb energy which causes excitation of electrons bound in the molecule, and the electrons then transit to a different eigenstate corresponding to the amount of energy transferred. The absorbed energy must be equivalent to the energy difference between the initial and high electronic state, and the corresponding wavelength is the excitation wavelength of the molecule. After the molecule absorbs photon energy, it is unstable and returns to its initial state with emitting photons. The energy of the photon emitted in fluorescence is equivalent of the difference between two energy states, and is less than that of the exciting photons due to heat or vibration. The corresponding wavelength is the emission wavelength of the molecule, and the difference between the excitation and emission wavelengths is the Stokes shift.

When fluorescence is emitted, the emission from molecules becomes polarized when the fluorophores are excited with plane-polarized light, and the level of polarized emission is described as anisotropy. When a fluorophore absorbs an incident photon, the excitation event arises from an interaction between the oscillating electric field component of the incoming radiation and the transition dipole moment created by the electronic state of the fluorophore molecular orbitals. Fluorophores preferentially absorb those photons that have an electric field vector aligned parallel to the absorption transition dipole moment of the fluorophore.

2.5.4. Exogenous and endogenous chromophores and fluorophores

What molecules can absorb and/or emit fluorescence? Fluorescence happens in exogenous fluorophores such as ICG and 5-aminolevulinic acid (5-ALA), and endogenous fluorophores such as hemoglobin and flavins. For example, ICG is a water-soluble compound that has been used clinically for diagnostics of cardiac output, hepatic function and other blood related diseases [153]. The peak absorption/excitation wavelength of ICG is 780 nm, and the peak fluorescence/emission wavelength is 840 nm (**Figure 2.2**). These wavelengths are in NIR window, and they can penetrate into tissue deeper compared with visible wavelength. Hemoglobin is a protein in red blood cells that carries oxygen. Hemoglobin molecule without bound to anything is called as deoxy-hemoglobin, and bound to oxygen is called oxy-hemoglobin. They have different absorption spectra (**Figure 2.2**). Moreover, autofluorescence is a main source of error in *in vivo* fluorescence imaging. Autofluorescence describes the background fluorescence from intrinsic endogenous fluorophores of cells and tissues, which is distinguished with exogenous fluorophores that

binds cell and tissue structures. When excited with photon of suitable wavelength, endogenous fluorophores will emit fluorescence, which can decrease signal-to-noise ratios.

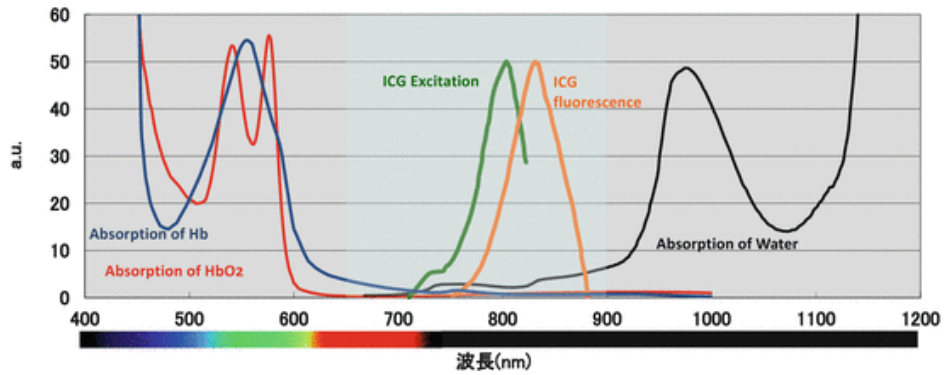

Figure 2.2: Absorption spectrum of common chromophores and fluorophores. Deoxy-hemoglobin is in dark blue, Oxy-hemoglobin is in red, ICG excitation is in green and emission is in orange, and water is in black. x-axis is wavelength (nm), and y-axis is absorption (a.u.). Image from [154]. Reproduced with permission from Springer Nature.

2.5.5. Optical properties of bone

Knowledge of light-tissue interactive properties of bone is required for designing and optimizing bone imaging system. The optical properties of bone have been studied in the visible, near infrared and infrared ranges [155]. Techniques and instruments for bone optical property measurement include integrating sphere [156], computerized CCD camera image analysis [157], diffuse reflectance and frequency domain photon migration [158], and time-resolved transmittance spectroscopy [159]. The absorption and reduced scattering coefficients of bone at 635 nm were determined to be 0.0359 mm^{-1} and 1.6160 mm^{-1}, respectively [160]. Specifically. bone structures including cortex and marrows have absorption coefficients of 0.038 mm^{-1} and 0.7 mm^{-1}, respectively; scattering coefficients of bone structures are same as whole bone because scattering in bone is determined by homogenous bone cavity.

2.5.6. Dynamic contrast-enhanced fluorescence imaging

Taking the knowledge of DCE, tracer kinetics, fluorescence and tissue optics discussed from the section 2.3 and section 2.5.1-2.5.5 together, we need to be cautious when designing the DCE-FI system, both in research and clinic settings. There are several important factors influencing the system performance and final results:

First, the designs of instrumentation need to consider for increasing detection sensitivity and signal specificity. The main problems in sensitivity and specificity are from the demand of detecting lowest possible concentration probes and the existing distractive background signal [161]. Fortunately, several existing hardware improvement approaches can solve the above problems, for example: Geometry and filter optimization can limit light leakage and increase signal efficiency [162]; Temporal gating can remove ambient light and gate to the excitation pulse [163]; Wavelength filtering and bandwidth restricting can remove the broad background [164–168]; Spectral fitting can remove background contamination [169].

Second, the selection of fluorescent contrast agent needs to consider the perfusion supply, clearance and nonspecific binding of the agent, as these factors dominate the performance of the agent [170–172]. In molecular imaging, single molecule agents tend to have nonspecific binding issues, and conjugation with antibody can increase the binding specificity [173–175]. However, the size of antibody will affect the pharmacokinetics, as larger antibodies have longer plasma retention times [176–178]. As a result, there are only a few agents approved in clinics. One of the few agents that are fully approved by the FDA is ICG, which is the contrast agent used in this thesis. ICG is intravenous administrated and cleared by the liver. ICG binds to plasma proteins and increases its hydrodynamic diameter.

The injection of ICG should be an ideal bolus injection, in order to ensure the quick targeted concentration and approximate a delta input [179].

Third, proper method of measuring AIF should also be used. Possible problems with AIF measurement include low temporal resolution for capturing fast AIF dynamics and saturation problems due to high contrast concentration in the artery [96]. When the artery is visible in the imaging plane, the AIF is measured from the DCE-FI images by fitting a model-based function [180]. When a suitable artery is not present in the imaging plane, then AIF can be retrieved using analytical form [181,182] or a population averaged AIF [183–185]. In this thesis, we are going to measure AIF using pulse dye densitometer [186,187] that is a modified pulse oximeter sensitive to ICG concentration. By this way, patient-specific AIF can be obtained intraoperatively by assembling the pulse dye densitometer to the DCE-FI system, and AIF can be extracted the offline [128]. **Figure 2.3** are numerical simulated AIFs produced under different perturbations.

Lastly, special attention should be paid towards what data interpretation and quantitative analysis approaches to use. The two main categories of approaches are model-dependent and model-independent approaches [188]. In model-dependent approaches, the physiology of tissue will be approximated in the form of mathematic equations, which provide the benefits of explicitly describing and quantifying the dynamic behavior of tissue [188]. Example of model-dependent approaches is compartment models, as described in section 2.2.3 and 2.2.5. In model-independent approaches, semiquantitative parameters are directly extracted from the tissue dye concentration curve (**Figure 2.4**). These parameters are related to physiological quantities of tissue, such as fractional blood volume, blood flow, permeability and interstitial volume [89,189]. The advantages of model-independent

approaches include free from prior assumptions and straightforward to implement [96]. Example of model-independent approaches is first-pass kinetic analysis, as will be introduced in Chapter 5. In first-pass kinetic analysis, peak enhancement (PE)/ maximum intensity (Imax) is extracted as the peak of the tissue dye concentration curve; time-to-peak (TTP) is the time from the arrival of dye to the PE/Imax; ingress slope (IS) and egress slope (ES) are calculated by fitting a line to the curve of ingress portion and egress portion, respectively.

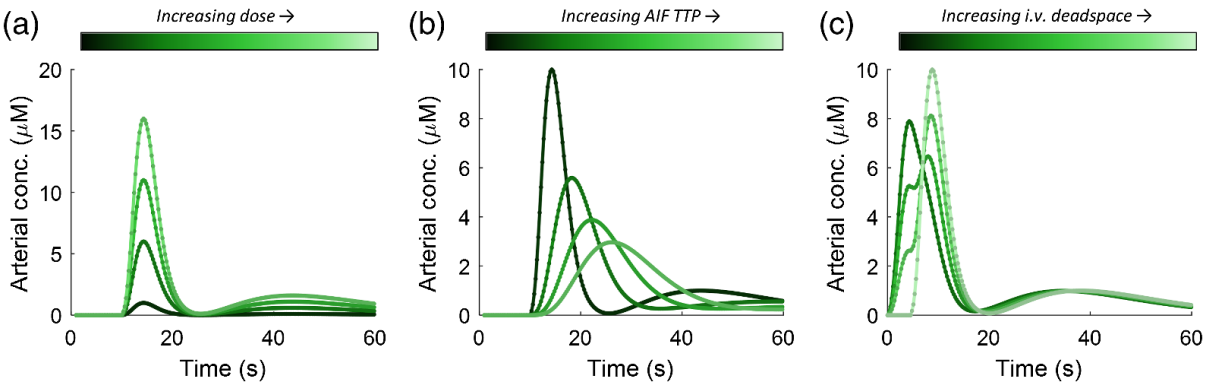

Figure 2.3: AIF perturbations. AIFs generated by modifying (a) dose, (b) speed of injection (TTP of the AIF), and (c) the "deadspace" in the intravenous tubing, which causes the bolus to enter the circulatory system in two phases. Image from [128]. Reprinted with permission from Society of Photo-Optical Instrumentation Engineers. © The Authors. [DOI: 10.1117/1.JBO.25.6.066002].

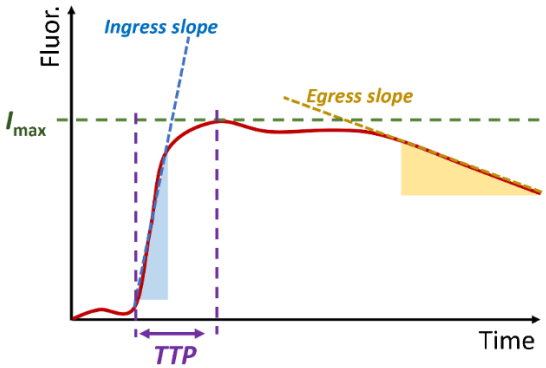

Figure 2.4: Extraction of first-pass kinetic parameters. The simple curve analysis produces typically one or more of the following parameters: Imax, TTP, ingress slope, and egress slope. Image from [128]. Reprinted with permission from Society of Photo-Optical Instrumentation Engineers. © The Authors. [DOI: 10.1117/1.JBO.25.6.066002].

2.6. Classification and Machine Learning

2.6.1. Overview of classification problem

In both clinical and operational settings, it is desirable to classify patients into whether they have particular disease as early as possible. Early classification can reduce the subsequent uncertainty and variability in the health care system and increase the efficiency of medical management and resource arrangement. Beside traditional classification by clinicians, computer-aided classification using machine learning/ artificial intelligence has gained increasing popularities. Current applications of using machine learning/ artificial intelligence include disease diagnose [190,191], tumor detection [192,193], and organ activity prediction [194–197]. Important criterion for computer-aided classification is accurate and insightful [198].

In general, the classification problem can be summarized as followed [199]: X is the measurement space where each x_i (i = 1, 2, …, n) is a measurement taken on a case. In each measurement x_i, predictive features/variables can be numerical or categorical. One of the classes (1, 2, …, J) has been assigned to x_i as labels in supervised learning, and no labels have been assigned in unsupervised learning. Classification process can be divided into training step and testing step. In training step, a classifier is trained by training data x_j ($j \subseteq i$) which is a subset of x_i. Then in testing step, the classifier assigns classes (1, 2, …, J) to testing data x_k ($k \subseteq i$) which is the exclusive from x_j. Classification metrices are computed by comparison of predicted classes of testing data with their true classes.

2.6.2. Image processing

Image processing refers to a sequence of operations on raw images to get enhanced images or extract information from images. In 2D image slices and 3D image stacks, the smallest unit in image processing is a pixel or voxel, respectively. Pixels and voxels contain intensity value at each channel of the image. In multi-channel images, channels may be combined or converted to a single channel. Image processing steps depend on the specific imaging modality and purpose, but there are some common steps as followed: (1) Image post-acquisition processing. This step is crucial in enhancing image quality. Current techniques in post-acquisition processing include denoising, image registration, artifact correction, and illumination correction [200–204]. (2) Image segmentation. Image segmentation is defined as the process of partitioning an image into nonoverlapping and homogeneous regions with respect to intensity or texture [205–207]. Common segmentation approaches are thresholding, region growing, clustering and artificial neural networks [208]. (3) Interpolation. Interpolation is required in texture feature extraction for isotropic voxel spacing and in comparison between different batches of image data. Interpolation algorithms include nearest neighbor, trilinear, tricubic convolution and tricubic spline interpolation [209].

2.6.3. Overview of features

One of the key components in machine learning classification is the selection of features/variables. The general term for features extracted from digital medical images is "radiomics". Radiomics describes the conversion of images into multi-dimensional data, and is motivated by that medical images contain information about underlying pathophysiology [210]. Application of radiomics can provide insights that are distinct from

clinical repots or laboratory tests, and can improve patient outcome by contributing to decision support, aiding cancer detection and predicting disease status.

There are two types of features in radiomics: “semantic” and “agnostic” features, where semantic features include common radiology lexicon terms and agnostic features are quantitative description of lesion heterogeneity [210]. Semantic features include size, shape, location, vascularity, speculation, necrosis and attachments or lepidic, and they are commonly used by radiologists to describe lesions quantitatively. Agnostic features include histogram, Haralick textures [211], Laws textures, wavelets, Laplacian transforms [212], Minkowski functionals [213] and fractal dimensions, and they are mathematically extracted quantitative descriptors of multi-order outputs. Among agnostic features, first-order features describe the distribution of values of individual voxels, second-order features describe statistical interrelationships between neighboring voxels and intratumoral heterogeneity, and higher-order features describe repetitive or non-repetitive patterns.

2.6.4. Texture analysis in bone imaging

Texture analysis [211] belongs to computer-aided classification and has been recently extended into bone imaging. By using texture analysis, important clinical and physiological information about the bone can be revealed. For example, texture analysis can reflect the spatial heterogeneity of lumbar vertebral bone marrow [214], reduced mineral bone density [215], osteoporosis [216,217], and operated/nonoperated femur [218]. Moreover, texture analysis combined with machine learning techniques have become accurate tools for classifying bone disorders, such as osteoporosis classification [219,220],

osteoarthritis control [221], bone fracture prediction and mineral disorders detection [222–224].

In this thesis, we used grey level co-occurrence matrix (GLCM) based features [211] for texture analysis in bone imaging. GLCM is a matrix describing how grey levels (*i.e.* discretized intensities) of neighboring pixels are distributed along one image direction, and the neighboring pixels refer to an 8-connected neighborhood (**Figure 2.5**). Therefore, there are four unique direction vectors for Chebyshev distance $\delta = 1$: (1, 0) (0°), (1, 1) (45°), (0, 1) (90°), and (-1, 1) (135°). A GLCM is calculated for each direction vector.

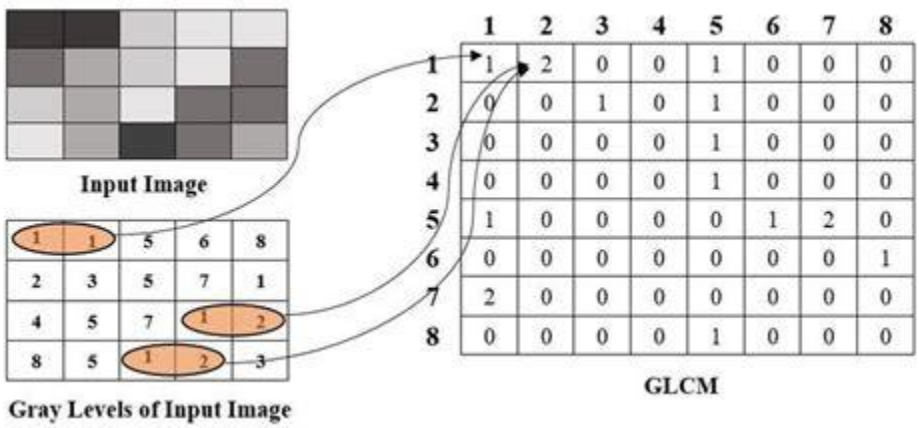

Figure 2.5: Example input image and the corresponding GLCM matrix. Image from [225]. Reproduced with permission from Springer Nature.

Let $\mathbf{M_m}$ be the $N_g \times N_g$ grey level co-occurrence matrix, with N_g the number of discretized grey levels in the region of interest, and **m** the particular direction vector. Element *(i, j)* of the GLCM contains the frequency where combinations of discretized grey levels *i* and *j* occur in neighboring pixels along direction **m**. In order to compute GLCM features, we need further calculate the probability distribution of the elements in the GLCM. The probability distribution of grey level co-occurrences, $\mathbf{P_m}$, is derived by normalizing $\mathbf{M_m}$ by the sum of all elements. Therefore, each element p_{ij} of $\mathbf{P_m}$ is then the joint

probability of grey levels *i* and *j* occurring in the neighboring pixels along direction **m**. At the end, GLCM features aggregated by computing from each 2D directional matrix and averaging over all directions. Four example GLCM features that have been included in this thesis: *Contrast* (describes intensity contrast between a pixel and its neighbor), *Correlation* (describes how correlated a pixel is to its neighbor), *Energy* (describes the sum of squared elements in the GLCM) and *Homogeneity* (describes the closeness of the distribution of elements in the GLCM to the GLCM diagonal), and their formulas are listed as followed:

$$Contrast = \sum_{i,j} |i-j|^2 p(i,j) \tag{2.10}$$

$$Correlation = \sum_{i,j} \frac{(i-\mu i)(j-\mu j)p(i,j)}{\sigma_i \sigma_j} \tag{2.11}$$

$$Energy = \sum_{i,j} p(i,j)^2 \tag{2.12}$$

$$Homogeneity = \sum_{i,j} \frac{p(i,j)}{1+|i-j|} \tag{2.13}$$

2.6.5. Feature dimensionality reduction

After extracting features, one big challenge is the large dimensionality associated with the large number of features. Large dimensionality will cause difficulty in computation speed and memorization space. In this case, dimensionality reduction, which is to find a matrix that contains same information but has fewer feature columns, is needed.

One type of the dimensionality reduction approaches is feature selection, which describes the process of keeping relevant features and discarding irrelevant or redundant ones. Feature selection methods include filters, embedded methods, and wrappers. Filters method, including Correlation-Base Feature Selection [226], Consistency-Based Filter [227], Information Gain [228], and ReliefF [229], focus on the general characteristics of the data and are independent of the learning algorithm. Embedded methods, including

Recursive Feature Elimination [230] and Lasso regularization [231], are performed during the training process and therefore are less computationally costly. Wrappers, including Wrapper Support vector machine [232], evaluate candidate subsets of features while interacting with the training classifier. The choice of feature selection should depend on which classifier is used, and sometimes combine two or more feature selection algorithms may work better [233].

Another common dimensionality reduction approach is principle component analysis (PCA). PCA is a mathematical algorithm that reduces the dimensionality of the data while retaining most of the variation in the data [234]. Principle components (PCs), along which the maximal variation in the data is, are identified and substituted the original features in the training process. By this way, the size of data can be reduced by reducing the number of features. For a dataset that contents p numerical variables and n observations, yielding an $n * p$ data matrix $\mathbf{X}$, PCs are the linear combinations of the columns of matrix $\mathbf{X}$ with maximum variance. PC can be computed [235] as:

$$\mathbf{X}\mathbf{a_k} = \sum_{j=1}^{p} a_{jk}\mathbf{x_j} \tag{2.14}$$

Where $\mathbf{a_k}$ (k=1,…, p) is the eigenvector of the covariance matrix $\mathbf{S}$ in which $\mathbf{a_1}$ is corresponding to the largest eigenvalue, a_{jk} is the vector of constant a_1, a_2,…, a_p of jth column, and $\mathbf{x_j}$ is pn-dimentional vector.

2.6.6. Predictive analytics on post-trauma infection

Predicting patient's risk for developing SSI after orthopaedic trauma surgery is the first step in preventing SSI. Early prediction of SSI can avoid surgery when there are reasonable nonoperative treatment options, spur prophylactic measures and alter

management strategies [236,237]. Based on identification factors of high-risk procedures and patient characteristics [238,239], a postoperative infection prediction model that predicts risk of infection at time of initial treatment has been developed by a shock trauma team recently [18]. In this predictive model, 8 independent variables were identified as significant association with increased risk of postoperative deep SSI, and they are age, male sex, obesity (body mass index (BMI) ≥ 30), diabetes mellitus, alcohol abuse, fracture region, Gustilo–Anderson type III open fracture, MRSA nasal swab result, and American Society of Anesthesiologists (ASA) class (**Table 2.2**). These variables were then used to create a risk score that can stratify patients based on infection risk with area-under-curve of 0.74, and estimate the percent risk of infection.

Table 2.2: **Prediction model of postoperative infection.** Table from [18]. Reprinted with permission from Wholters Kluwer Health, Inc.: Wise, Brent T.; Connelly, Daniel; Rocca, Michael; Mascarenhas, Daniel; Huang, Yanjie; Maceroli, Michael A.; Gage, Mark J.; Joshi, Manjari; Castillo, Renan C.; O'Toole, Robert V.. A Predictive Score for Determining Risk of Surgical Site Infection After Orthopaedic Trauma Surgery. Journal of Orthopaedic Trauma 33(10):p 506-513, October 2019. DOI: 10.1097/BOT.0000000000001513. Copyright © 2019 Wolters Kluwer Health, Inc.

Predictive variables	**Points**
Demographics	
Gender	
Female	0
Male	1
BMI	
<30.0	0
≥30.0	1
Comorbidity	
Diabetes	2
Alcohol abuse	2
Fracture characteristics	
Bone region	
Upper extremity	0
Hip and femur	1
Patella, talus, forefoot, and midfoot	2
Tibial plateau, tibial shaft, pilon, ankle, and calcaneus	2
Pelvis/acetabulum	4

Open/closed Gustilo type	
Closed	0
Open, Gustilo I-II	0
Open, Gustilo III	3
Injury and treatment characteristics	
MRSA nasal swab testing	
Not tested	1
Negative	0
Positive	5
Preoperative ASA class	
I	0
II	1
III	3
IV-V	3

Beside the above statistical predictive analytics, machine learning is also a useful tool in infection prediction on orthopaedic trauma surgery. When deciding on the treatment plan for patients presenting with trauma, clinicians should focus on factors revealing the presence of infection as many as they can. These factors have been found to be multidimensional, including imaging features, the informatic features as discussed above, and kinetic features. Features from these three categories can reveal important clinical information in different aspects, and they all have been applied to several related studies: Firstly, imaging features are mainly referring to the texture features in radiomics. Several recent studies on orthopaedic surgery have applied texture-based machine learning classification, which include bone age detection [240], osteoporosis detection [216], bone disorder classification [215] and fracture risk prediction [219]. Second, beside pure statistical analysis, machine learning classification based on informatic features have also been developed as predictive tools for clinical decision-making. Current applications are mainly in periprosthetic joint infection prediction including non-recurrent infection [241] and recurrent infection [242]. Last, kinetic features are extracted from tracer kinetic theory

of fluorophore temporal curves. The predictive performance of kinetic features has been proved by several pre-clinical studies [14,15,37].

Chapter 3

Validation of DCE-FI by mQUIC in the rabbit femur

This chapter highlights the work published in "Validation of dynamic contrast-enhanced bone blood flow imaging technique with fluorescent microspheres" by Han X, Demidov V, Wirth D, Byrd B, Davis SC, Gitajn IL, and Elliott JT, published in *Proc. SPIE* volume 11943, Molecular-Guided Surgery: Molecules, Devices, and Applications VIII in 2022, and "Initial experience of perfusion assessment in a rabbit model of orthopaedic trauma surgery using fluorescent microspheres and hyperspectral imaging cryomacrotome" by Han X, Demidov V, Wirth D, Byrd B, Davis SC, Gitajn IL, and Elliott JT, published in *Proc. SPIE* volume 12146, Clinical Biophotonics II in 2022. Jonathan T. Elliott provided supervision of the project, gave intellectual input and reviewed the manuscript. I. Leah Gitajn provided clinical instructions and review the manuscript. Scott C. Davis provided the cryo-imaging system. Brook Byrd assisted with the image acquisition and preprocessing. Dennis Wirth performed the image acquisition and assisted with sample preparations. Valentin Demidov provided intellectual input and assisted with manuscript writing. The author of this thesis designed and conducted animal experiments, processed and recovered images, programmed the analytic software, analyzed the data, and wrote the manuscript. This chapter has met copyright permission requirements under The International Society for Optics and Photonics copyright.

This chapter introduces a proof-of-concept validation for dynamic contrast-enhanced fluorescence imaging (DCE-FI) in bone perfusion measurement. The approach is a modified fluorescent microsphere quantification technique using a custom-built multi-channel cryomacrotome, which we have termed “mQUIC”. Phantom study, *ex vivo* blood

sample study and *in vivo* animal study have been included to examine the performance of mQUIC. mQUIC can provide volumetric bone perfusion maps in endosteal and periosteal compartments separately, which will be applied as a ground truth to assess bone perfusion changes detected via DCE-FI.

3.1. Introduction

In orthopaedic trauma surgery, timely assessment of bone tissue perfusion plays a vital role in successful treatment outcome. Perfusion is an important indicator of the viability of bones during orthopaedic surgery [14] For bones with inadequate perfusion, timely and thorough debridement is necessary, otherwise bacterial infection can become established, form biofilms and result in persistent infection and conversion to amputation [15,16,43,45]. With the most popular assessment approach still being the surgeon's eyes, contrast enhanced imaging modalities like computed tomography (CT) and magnetic resonance imaging (MRI) can provide useful information. However, their intraoperative use is very limited in this type of surgery. CT requires large radiation dose. MRI is time consuming, susceptible to metallic implant artifacts, and overall expensive [112]. In light of this, fluorescence-guided surgery (FGS) is gaining increased clinical interest [243] generally, and more recently, with respect to hemodynamic assessment of bone [19]. FGS works by introducing fluorescent contrast into the circulatory system, and then imaging the labeled blood circulating through tissue. Although the technique can be quite powerful, FGS is often only used in a qualitative manner, but can be made quantitative to extract perfusion information [19,21]. As we recently reported, intraoperative DCE-FI and subsequent analysis using kinetic models may not only visualize the perfused areas of the injured bone, but can also provide a valuable quantitative information to the surgeon about periosteal and endosteal blood flow [21]. Currently, there is no 'gold standard' for validating the performance of DCE-FI in quantifying perfusion.

As the next step in the development of the blood flow fluorescence imaging technique, we are validating DCE-FI with a modified fluorescent microsphere (FM)

quantification approach [244] called mQUIC. FMs are uniform sized spherical contrast agent that can emit fluorescence signals of various wavelength. The method used in this study is based on the observation that the number of FMs entrapped in capillary bed is proportional to blood flow [144]. Perfusion is computed by identifying the density of deposited microspheres in reconstructed imaging volumes, which are proportional to regional blood flow, and are compared to a 'reference organ'—a syringe drawing arterial blood at a known rate (e.g., ~1 mL/min). FM techniques have been developed to act as a 'gold standard' to measure perfusion in other FGS categories [32]. FM technique has been developed to measure blood flow and has applied in multiple organs [145]. In this study, we are further expanding the application of FM technique in orthopaedic surgery.

The methodology of this study involves the following steps: (1) phantom study, (2) whole blood study, and (3) rabbit femur study. The cryo-imaging was first tested in phantoms to have linear response to the number of microspheres, be independent of the color of microspheres, and can detect FMs in controlled environment. Whole blood study was included to evaluate detection accuracy in real blood samples, since whole blood is the reference sample for perfusion measurement.

In the rabbit femur model, cryo-imaging was used to scan six rabbit femurs (three left femurs under surgery and three right femurs without surgery), which were injected with three colors of microspheres corresponding to three conditions: baseline, post-osteotomy and post-periosteal stripping. Based on the image stacks from multiple imaging channels of the cryo-imaging system, we have successfully segmented bone and its surrounding muscle, and then incorporated these volumetric renderings into the visualization. Meanwhile, FMs from bone segmentation as well as muscle segmentation were been

recovered. Image processing, including top-hat transform and object-based colocalization analysis, was used to clean up noise and improve counting accuracy. Finally, individual FMs were plotted in 3D space with color-coded spatial density. In this way, the bone perfusion level in both endosteal and periosteal regions are estimated by converting from the FM density level based on the reference organ method. The volumetric FM density map is converted to bone perfusion units (mL/min/100 g) using the reference organ technique. This proposed fluorescent microsphere technique will be applied as a gold standard for measuring bone perfusion in orthopaedic surgery in planned validation studies.

3.2. Methods and Materials

3.2.1. Phantom and whole blood study

Fluorescent microspheres of 15 μm diameter (ThermoFisher FluoSpheres, Thermo Fisher Scientific, Waltham, MA) were used in this study. Four colors were selected in according to the near infrared (NIR) channel of the cryo-imaging system as well as their relatively high quantum efficiency, low spillover and high signal-to-noise ratio [140]: yellow-green (Ex 505/Em 515), orange (Ex 540/Em 560), crimson (Ex 625/Em 645) and scarlet (Ex 645/Em 680). FMs have been 2-fold serially diluted from 125 to 2000 beads/mL. Each serial dilution was added into (a) optimal cutting temperature compound (OCT compound, Fisher Scientific, Pittsburgh, PA), and (b) Na-Heparin bovine whole blood (Lampire Biological Laboratories, Inc., Pipersville, PA). Well-mixed FM solutions (a) were solidified at -20 °C, and scanned by a custom-built hyperspectral cryo-macrotome imaging system [150] at -20 °C. Briefly, the whole animal cryo-macrotome Leica CM3600 (Leica Biosystems, Germany) was modified by the Davis Lab at Thayer, adding a custom-

built multi-channel hyperspectral optical imaging system containing three LED light sources (470 nm, 530 nm and 633 nm). OCT compound-embedded mixture (a) was sectioned into 100 µm sections and scanned to obtain 93×93×30 mm^3 volumetric images and to count FMs using ImageJ software (National Institutes of Health, USA). Microspheres-blood mixture (b) was digested overnight by 89.2% potassium hydroxide (KOH) and filtered out next day by negative pressure filtration method using 10 µm polypropylene membrane (Sterlitech, Kent, WA). Each membrane with captured FMs was then dissolved into 2-ethoxyethyl acetate solution for fluorescent dye extraction and fluorescence quantification by fluorimeter (FluoroMax-4, Horiba, Ltd., Kyoto, Japan).

3.2.2. Animal study

We performed animal experiments (IACUC number-00002227) to evaluate the suitability and performance of mQUIC in bone blood flow. In this non-survival rabbit model (~3.0 kg, ~12 weeks, female New Zealand White rabbit, Charles River). Animals are anesthetized using isoflurane, prepared for microsphere injection and blood draws, and their left femurs are surgically exposed for imaging (**Appendix A**). Fluorescence camera is placed directly in front of the surgical site with a dye densitometer probe placed on the hind paw of the non-affected leg. 7.5 mL FMs of one color is injected into the right femoral artery at three conditions (**Figure 3.1**): (1) baseline, (2) osteotomy, and (3) osteotomy and periosteal tissue stripping. During the FM injection and washout, blood is withdrawn from the femoral artery at the rate of 0.33 ml/min. This blood draw represents the 'reference blood sample' [244]. Microspheres-blood mixture was digested overnight by 89.2% KOH and filtered out next day by negative pressure filtration method using 10 µm polypropylene

membrane. Each membrane with captured FMs was then dissolved into 2-ethoxyethyl acetate solution for fluorescent dye extraction and fluorescence quantification by fluorimeter. We measured the femur blood flow Q_i in mL/min at each condition using the following equation:

$$Q_i = \frac{n_i k_i}{fl_{ref,i}} R, \ (i=1,\ldots,4) \tag{3.1}$$

Where the withdrawal rate of the reference blood sample is R (= 0.33 mL/min in this study), $fl_{ref,i}$ is the measured fluorescence intensity of reference blood sample, n_i is the number of detected microspheres in the femur, and k_i is the intensity-FM concentration slope [244]. Here, the slope k_i for each FM color has been measured during whole blood study. FM-based rates Q_i versus DCE-FI-measured blood flow rates have then be analyzed and compared.

Following FM injection, DCE-FI involved acquiring femur images during the ear vein injection, wash-in, wash-out of indocyanine green (ICG) dye (0.1 mg/kg) at each condition with 30 min intervals to allow ICG to clear plasma (**Figure 3.1**). At the end, animals are euthanized, their left and right femurs (surgery-side and no-surgery-side, respectively) were removed, frozen in OCT compound of 120 × 60 × 30 mm^3 size and processed in the 3D cryo-macrotome for slicing into 100 μm sections and imaging. The main goal of this procedure is to see if we can reliably recover the microspheres *in situ* to produce then volumetric maps of bone blood perfusion and to compare these results with DCE-FI blood flow measurements.

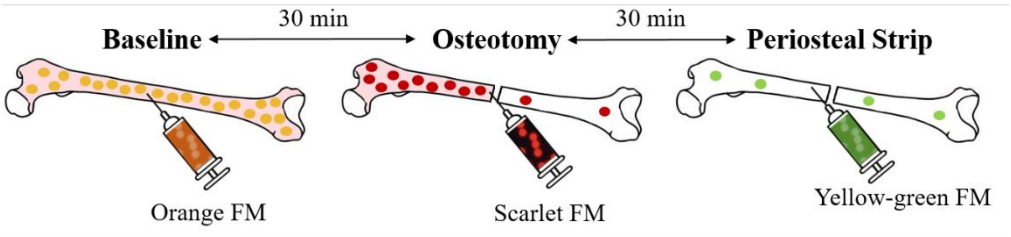

Figure 3.1: Conceptual diagram of surgical procedures in animal study. FMs were injected via intra-atrial catheter. After each FM injection, there is 30 minutes waiting time for dye wash-out.

3.2.3. Dynamic contrast-enhanced imaging system

For each condition—baseline, transverse osteotomy, transverse osteotomy with periosteal stripping—ICG based DCE-FI images were acquired five minutes after the fluorescent microspheres were injected and collected, so that the physiological state of the animal is sufficiently similar. An in-house developed imaging system was used to capture the DCE-FI time-series of images. The system consists of a Zeiss OPMI 1-FC operating microscope head (Carl Zeiss Meditec AG, Jena, Germany) fitted with an F-200 mm objective lens. Attached to the dovetail interface of the top of the head is a custom form containing a 45-degree silver coated mirror directing the light to a SM-1 flange interface. Attached to this is a lens tube containing an acromat lens (Edmund Optics), a 770-nm dichroic filter to reject excitation light (T770lpxr, Chroma Technology Corp, Rockingham, VT) and a 780-nm long-pass filter to further reject any bleedthrough (et780lp, Chroma). Light is focused on a CMOS Panda 4.2 camera (PCO GmbH, Kelheim, Germany). Excitation is achieved with a 740-nm high-powered LED source (10 W, 22 mm Type B, Mightex, Toronto, Canada) fitted with a bandpass filter (et740/40x, Chroma). During each condition, 0.1 mg/kg of ICG was injected intravenously. The dynamic fluorescence was captured with a 200-ms exposure time, continuously for 5 minutes. A total of 20 minutes

was allowed between ICG injections to allow for elimination of the dye from plasma circulation.

3.2.4. Multi-channel cryo-macrotome imaging system

The custom-built cryo-imaging system [150] consists of a whole animal cryomacrotome Leica CM3600 (Leica Biosystems, Germany) fitted with a custom-built multi-channel hyperspectral optical imaging system. Frozen specimens are automatically sectioned with 100 μm thickness within the CM3600 cabinet at -20 °C. The optical imaging system consists of a mounting plate that accommodate four light sources: A 6500 K white light LED, a 470 nm LED, a 523 nm LED, and a 635 nm laser. Light emitted from the specimen is collected using a 500 mm focal distance objective lens (Thorlabs, Newton, NJ) and then split into two detection channels; a visible channel and a NIR channel, using a 750 nm short pass dichroic mirror (Thorlabs, Newton, NJ). Light transmitted through the visible detection channel is detect by on a cooled, 16-bit scientific CMOS camera (Edge 4.2, PCO, Bavaria, Germany). Light transmitted through the NIR channel is filtered by long pass filters (500 nm, 550 nm, and 650 nm cut-on, ThorLabs, Newton, NJ) before detection with a 2nd PCO scientific CMOS camera. The field of view is 93 × 93 mm and the depth of focus is 30 mm, with a lateral resolution of 71 μm.

3.2.5. Image pre-processing, processing, and volumetric rendering

A sequence of hyperspectral images from the cryo-imaging system were pre-processed to improve the image quality [245]. First, different NIR channels were unmixed according to different FM colors: 470 nm channel for yellow-green FM, 523 nm channel

for orange FM, and 635 nm channel for crimson and scarlet FM. Second, we corrected images by background subtraction, illumination field correction and radial distortion. Third, we performed spectral remixing [246], unmixing [247], and 'Next Image' correction [248] to separate background signals.

Following the pre-processing steps, image stacks for each NIR channel (**Figure 3.2(a)**), merged NIR channel (**Figure 3.2(b)**) as well as the bone from visible channel were processed using MATLAB (R2020b, MathWorks, Natick, MA). White top-hat filtering transform [249] was applied to each image slice, with a disk-shaped structuring element, to remove the background illumination from tissue auto-fluorescence. Following that, subcellular colocalization algorithm [250] was used to count the number of each color FM and produce the volumetric center-of-mass-of-FM map (**Figure 3.2(c)**) using ImageJ. Besides, the region of bone from image stack of visible channel was segmented by threshold and region growing methods, and then volumetric rendered using 3D Slicer software (version 4.11, Kitware Inc., Clifton Park, NY, USA).

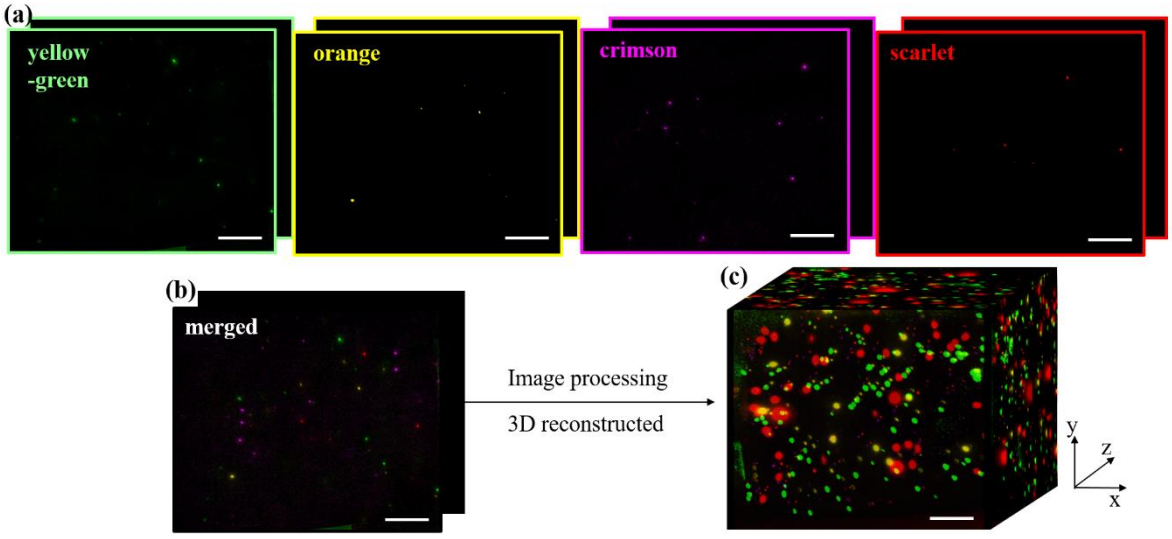

Figure 3.2: Image stacks from cryo-imaging of phantoms. Scale bars are 2 cm. (a) Image stacks of four FM colors from three NIR channels, from left to right: yellow-green (470 nm),

orange (523 nm), crimson (635 nm), and scarlet (635 nm). (b) Image stacks of merged all FM colors. (c) 3D reconstructed volumetric center-of-mass-of-FM map of all colors.

The volumetric center-of-mass-of-FM map of each color FM was then processed as followed to create volumetric density-of-FM maps: First, the size of single FM was determined according to phantom scans as 10 pixels. Second, spatially overlaid FMs were unmixed to number of that divided by 10. Third, the unmixed FMs were grouped into 8 bins according to their spatial density. Lastly, the FMs were color-coded according to the bins they belong to.

3.3. Results

3.3.1. Phantom study demonstrates the linear response of 3D microsphere detection in OCT phantom

Cryo-macrotome imaging system is capable of detecting FMs with high spatial resolution throughout 30 mm thickness. As we can see from **Figure 3.3(a)**, individual FM were clearly visualized and separated from each other in 3D. Image analysis for microspheres counting demonstrated linear dependence of detected (counted) numbers of microspheres from true (injected) numbers (**Figure 3.3(b)**). The optimal linear fitting equation is $y = 0.93x - 21.7$, with r^2 of 0.98. We also performed Bland-Altman analysis between detected microspheres of one individual color and their true number (**Figure 3.3(c)**), and observed that there is no difference among colors. We can then conclude that cryo-macrotome imaging system has a perfectly linear response to FMs in 3D.

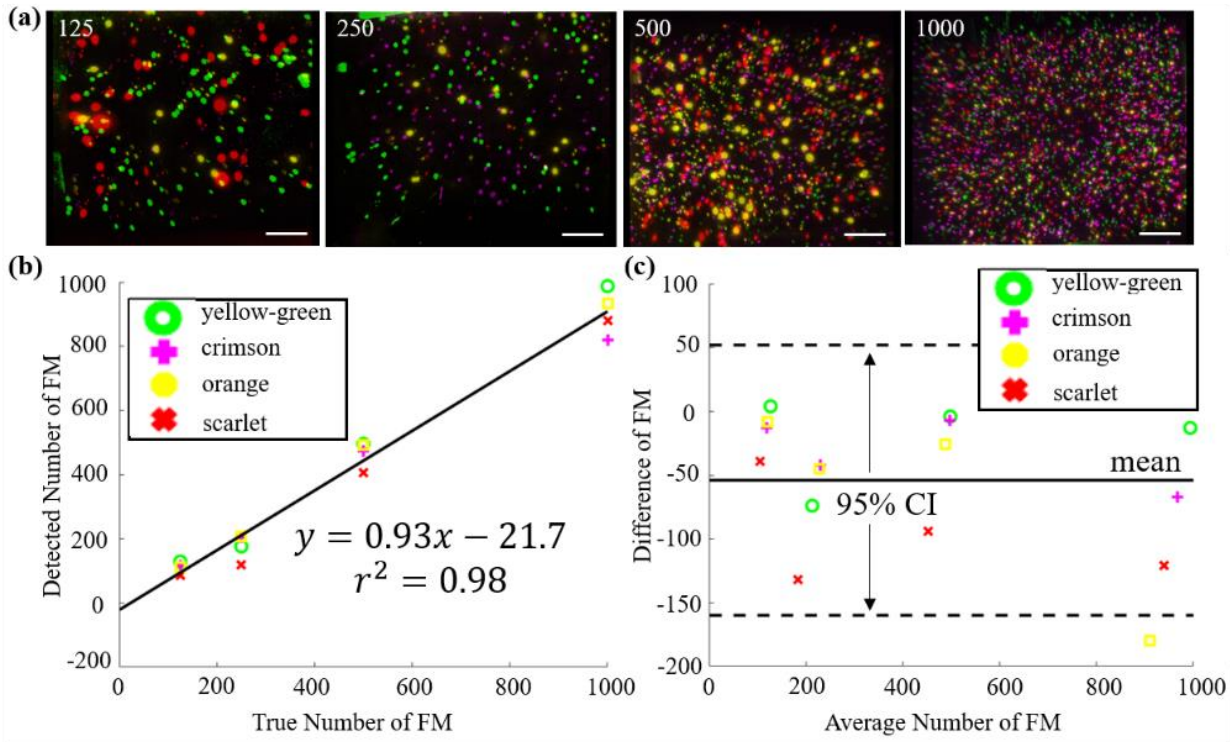

Figure 3.3: Fluorescence microsphere OCT phantom study. (a) 3D cryo-matrocome images of OCT compound frozen phantom with color coded FM of mixed four colors, ranges from 125 to 1000 beads per sample. Color dots are arbitrary colors not actual FM colors. Scale bars are 2 cm. (b) Linear relationship of detected number and true number. (c) Bland-Altman plot of detected microspheres of one color versus their true numbers. CI: confidence interval.

3.3.2. Development of calibration standard for accurate whole blood measurement

Whole blood study has shown that FM is a stable contrast agent that can be used in a blood sample and thus can be further applied in pre-clinical studies. After filtration, blood have been filtered out with only microspheres remaining on the filter membrane surface (**Figure 3.4(a)**). Fluorescent intensity detection and quantification of the released encapsulated fluorescent dyes after dissolving microsphere shells with organic solvent (**Figure 3.4(b)**) showed the linear increase in fluorescence proportional to true concentration of microspheres of each color to the blood (**Figure 3.4(c)**). Meanwhile, the measured fluorescence intensity-FM concentration slop k_i (i = 1, 2, 3, 4, in counts per

second (CPS)*mL/beads) for all color have been calculated (k_1 = 2800 for yellow-green, k_2 = 950 for crimson, k_3 = 1820 for orange, and k_4 = 226 for scarlet), and will be used as internal standard for the following animal study.

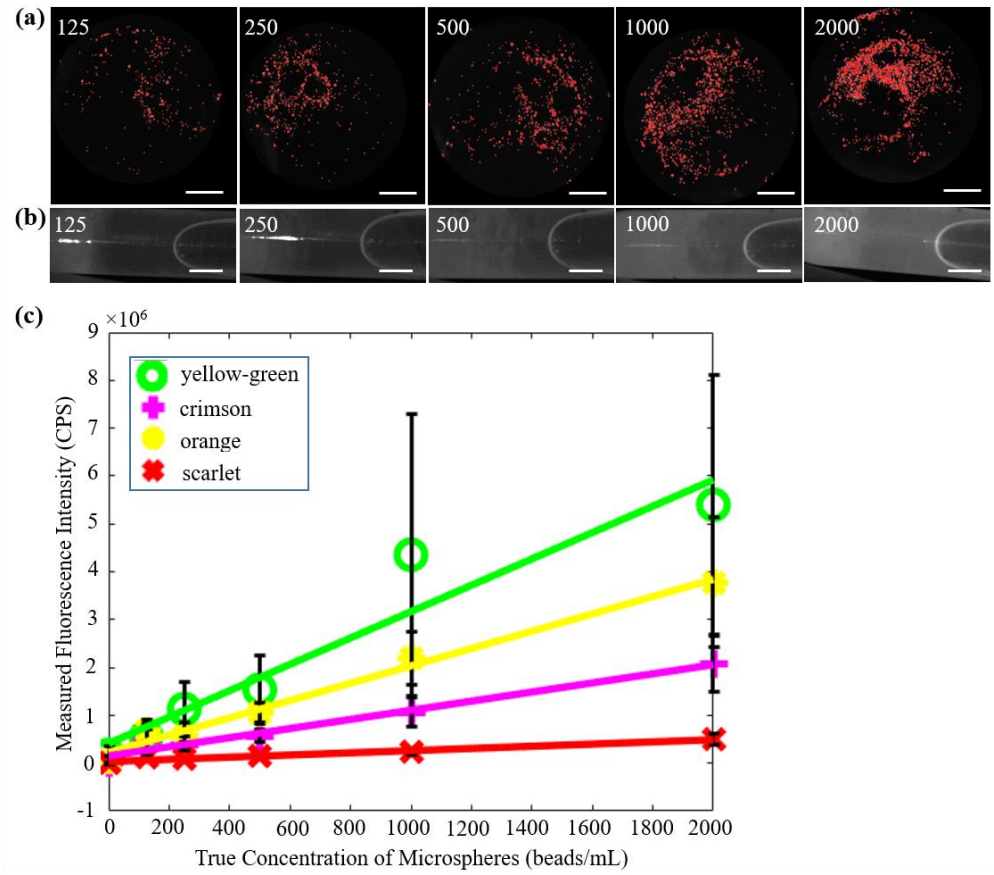

Figure 3.4: Fluorescence microsphere whole blood study. (a) Polypropylene filter membrane attached with "Scarlet" FMs (125 to 2000 beads per sample, FMs are labeled with red dots). Scale bars are 5 mm. (b) "Scarlet" FM dye extracted from polypropylene filter membrane (125 to 2000 beads per mL) in sample tubes. Scale bars are 4 mm. (c) Fluorescence intensity measured from each FM color dye extraction solution.

3.3.3. Color and monochrome images acquired with system

Color and monochrome images have been acquired by multiple channels of cryo-imaging system. RGB images (**Figure 3.5(a)**) and white light images from visible channel (**Figure 3.5(b)**) displayed the internal structures of femurs with and without surgery. Monochrome images from NIR channel (**Figure 3.5(c)**) showed the fluorescent signals

from FMs, as well as some auto-fluorescence from tissues. From cross-sectional views (**Figure 3.5(d)**), FMs were distributed evenly in bone and surrounding muscles.

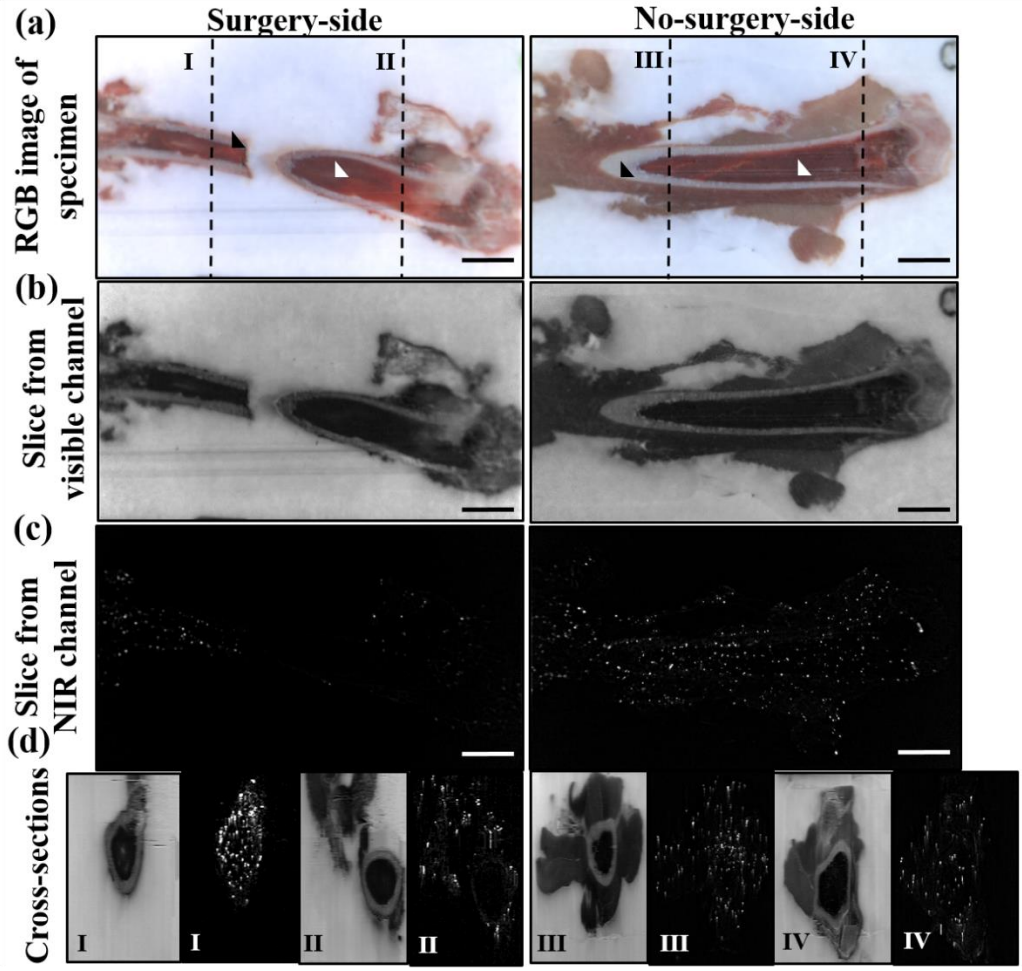

Figure 3.5: Color and monochrome images from cryo-imaging. Left: surgery-side femur, Right: no-surgery-side femur. Scale bars are 1.5 cm. (a) RGB images of specimen. Black dashed lines are axes (I ~ IV) of cross-sectional views in (d). Bone cortex and marrow are denoted by black and white arrow head, respectively. (b) Example slice from visible channel of cryo-imaging scans. (c) Example slice from 635 nm NIR channel. (d) Cross-sections of cryo-imaging scans, by axes I~IV from (a) on visible (left) and 635 nm NIR (right) channels.

3.3.4. Volumetric center-of-mass-of-FM maps after top-hat transform can visualize perfusion

Unlike in the OCT phantoms, signal from tissue auto-fluorescence obscured FMs and reduced the signal-to-noise ratio (**Figure 3.6(a)**). The regions of auto-fluorescence were often larger and less homogenous than those of FMs. Therefore, top-hat transform was employed to efficiently eliminate auto-fluorescence and only leave FM signals (**Figure 3.6(b)**).

Figure 3.6(b) shows the actual detected microspheres for the entire volume acquired on the surgery-side femur. From **left** to **right**, the images represent three serial injections under baseline, post-osteotomy and post-stripping conditions. Corresponding to these conditions of increasing severity, the number of FMs recovered from the volume decreases (5525, 2965, and 196, respectively). As expected, since the second condition (osteotomy) involves a disturbance of endosteal flow (*i.e.,* blood flow from within the middle of the bone), and some disturbance of the periosteum, whereas the third condition involves complete disturbance of both endosteal and periosteal supply for most of the femur, this increasing devascularization of the bone resulted in the number of FMs entrapped being reduced. The volumetric center-of-mass-of-FM map provides a visualization of this reduction in bone perfusion.

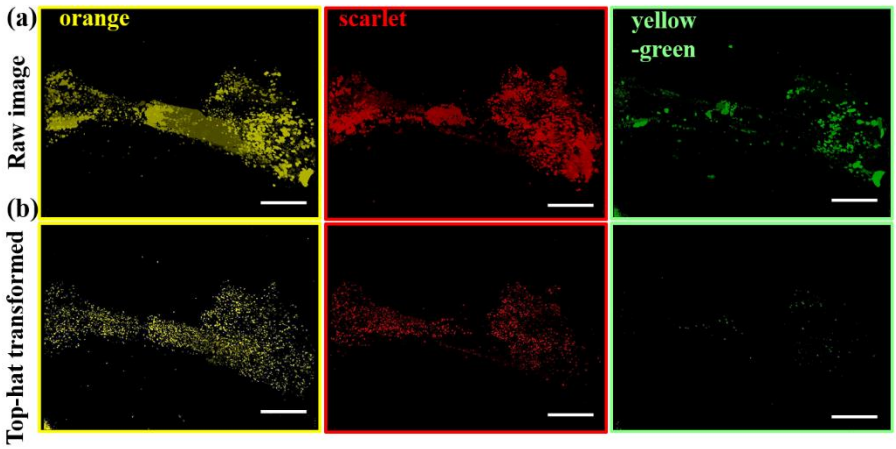

Figure 3.6: Volumetric center-of-mass-of-FM maps from surgery-side femur. Maps are displayed in three FM colors, corresponding to three bone conditions. Left: orange FM, baseline; Center: scarlet FM, osteotomy; Right: yellow-green FM, periosteal strip. Scale bars are 2 cm. (a) Raw map before processing. Tissue auto-fluorescence (in large and irregular shape) and FM signals (in small spherical shape) were overlapped. (b) Processed map after top-hat transform. Only FM signals were visualized.

3.3.5. Converting volumetric center-of-mass-of-FM maps into quantitative perfusion maps

To ensure the reproducibility of our technique, and account for any differences in the recovery of the different colors of microspheres from tissue imaging, we used the contralateral femur as a control (*i.e.*, no surgical procedures were performed on the contralateral side). In **Figure 3.5(a)**, the specimen of surgery-side is bone with a few muscles at femoral head, while the specimen of no-surgery-side is bone covered with a thick layer of muscle. In addition, the surgery-side bone was cut into two pieces with a disconnection in the middle and showed some degree of deformation, while the no-surgery-side bone was intact. The ipsilateral femur microsphere counts were adjusted by a correction factor based on the assumption that the recovered spheres on the contralateral side should be equal for each color.

Quantitative bone perfusion maps (**Figure 3.9**) were produced by image processing and visualization steps on NIR (**Figure 3.7(a)**) and visible (**Figure 3.7(b)**) channels

separately and then overlaying together. On NIR channel, volumetric center-of-mass-of-FM maps were firstly converted into volumetric density-of-FM point cloud maps by color-coded with spatial density (#/100 g, see details in section 3.2.5). Then the bone perfusion (in mL/min/100 g) were estimated by comparing with the withdrawal rate and fluorescence quantification of reference blood sample [244,251]. On visible channel, volumetric rendering was achieved on segmented bones. Sequentially, the perfusion-coded volumetric FM point cloud maps were overlaid with volumetric rendered bones to produce quantitative bone perfusion maps (**Figure 3.8**). Finally, the volumetric FM density map is converted to bone perfusion units (mL/min/100 g) using the reference organ technique (**Figure 3.9**).

In the surgery-side femur (**Figure 3.8(a)**), only endosteal perfusion was visualized because all periosteal tissue has been removed in specimen. In **Figure 3.8(a) top**, FMs were distributed in all endosteal area, with medium perfusion (0.4~1.2 mL/min/100 g) on the sides and higher perfusion (> 1.2 mL/min/100 g) in the middle. All blood vessels were intact; In **Figure 3.8(a) center**, FMs were distributed in two disconnected bone pieces, with medium perfusion (0.4~0.8 mL/min/100 g) on the sides and no perfusion in the middle. Endosteal blood vessels in distal bone have been cut off; In **Figure 3.8(a) bottom**, FM have lowest perfusion (< 0.4 mL/min/100 g), with only a few distributed at femoral head. All endosteal and periosteal blood vessels have been disrupted. In comparison, in the no-surgery-side femur (**Figure 3.8(b)**), both endosteal and periosteal perfusion was visualized. So FM is distributed inside the bone as well as outside the bone. Moreover, the FM density as well as bone perfusion (0.4~1.6 mL/min/100 g) stay constant among different FM color because all blood vessels were intact and unchanged. In summary,

volumetric FM point cloud maps can assess bone perfusion in both endosteal and periosteal, and the FM density can accurately reflect the level of perfusion.

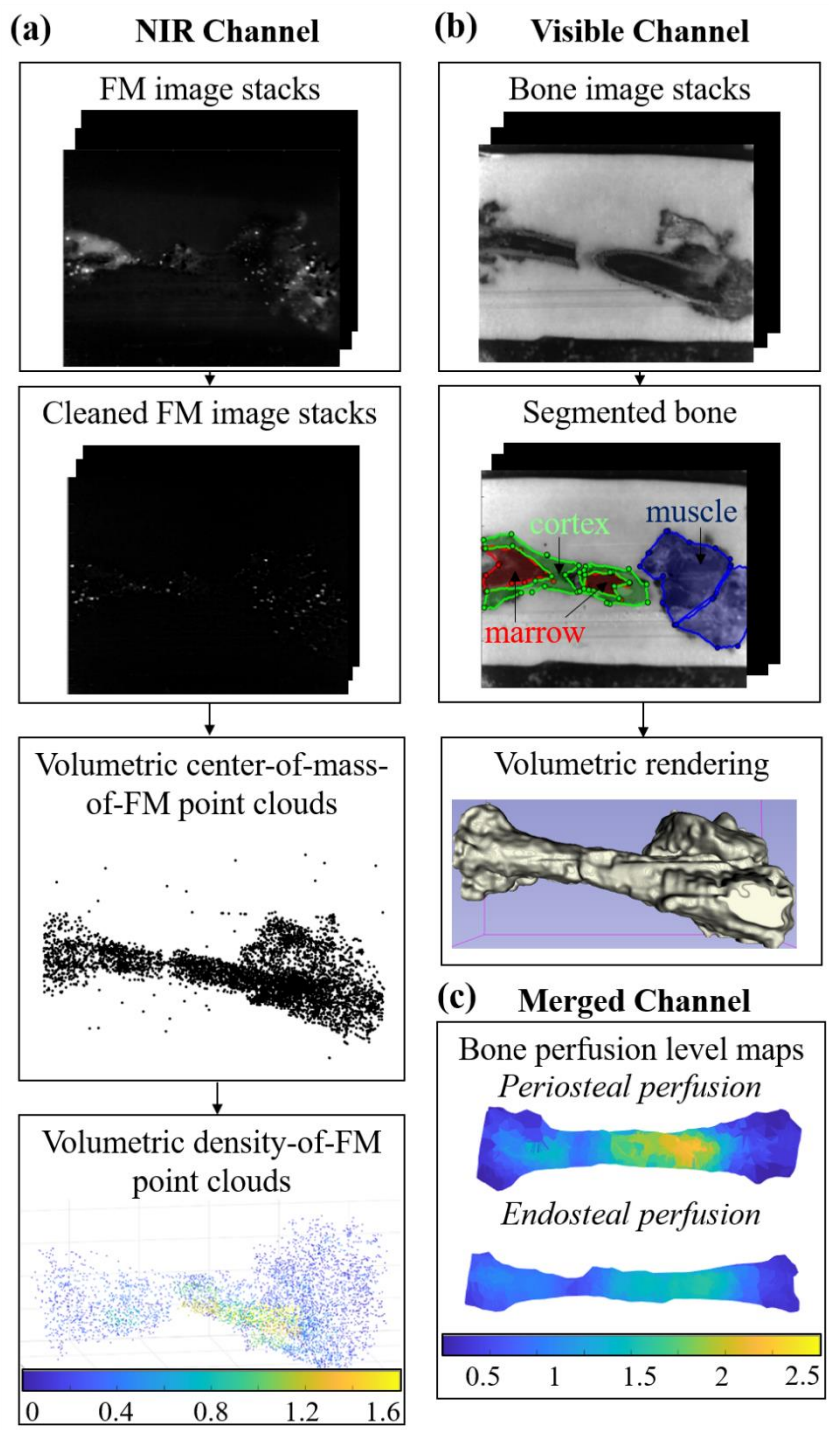

Figure 3.7: Flowchart of generation volumetric perfusion maps. (a) Flowchart of converting NIR channel image stacks into volumetric density point clouds. (b) Flowchart of converting

visible channel image stacks into volumetric rendering of segmented bone structures. (c) Merged quantitative perfusion level maps from NIR and visible channels.

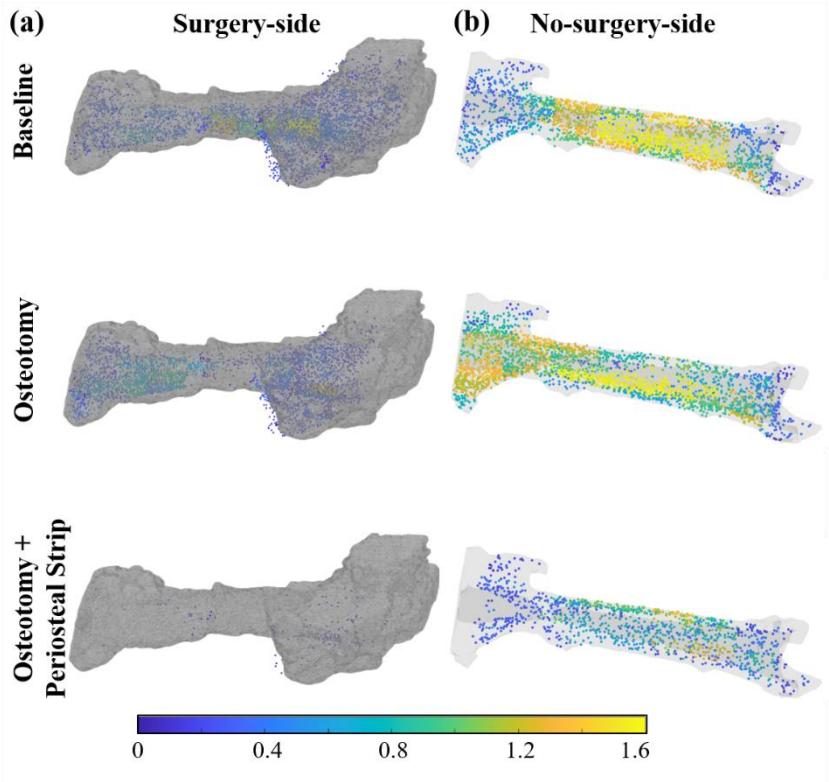

Figure 3.8: Perfusion-coded volumetric FM point cloud maps. Volumetric FM point cloud maps are overlaid on segmented bone (in gray), and color-coded with estimated perfusion (in mL/min/100 g). Top: orange FM, baseline; Center: scarlet FM, osteotomy; Bottom: yellow-green FM, osteotomy +periosteal strip. (a) Surgery-side femur. (b) No-surgery-side femur. Bones from all three colors were intact. (c) Bar graphs of average perfusion. Error bar = standard deviation.

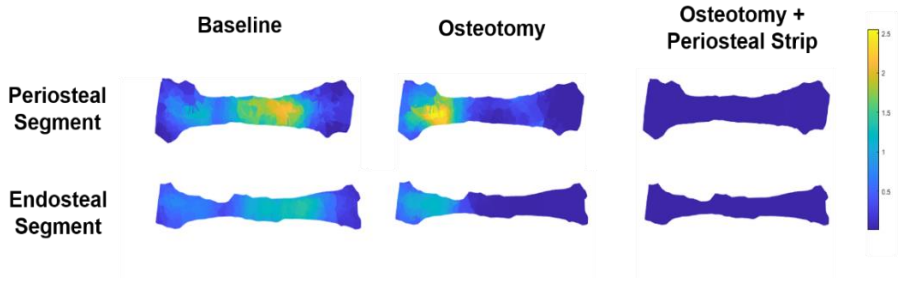

Figure 3.9: Volumetric perfusion maps. The maps are generated by mQUIC based on density of identified microspheres**.** Values are in $mL \cdot min^{-1} \cdot 100\ g^{-1}$.

3.3.6. Animal study modified FM technology for DCE-FI validation

In this pilot animal study, the FM technology has been modified from literature of other animal models [144,145,148] to rabbit femur, and used as a validation tool for our proposed DCE-FI kinetic model. In the DCE-FI model, we could interpret the level of perfusion by referring to the fluorescent intensities. By comparing the fluorescence images under three conditions (**Figure 3.10(a)**), we can see the fluorescence intensities of the femur decreased as more vasculature being disrupted. Besides, temporal profiles of two circular regions-of-interests (ROIs) under same conditions also showed this trend (**Figure 3.10(b)**). Furthermore, the fluorescence microsphere volumetric maps (**Figure 3.10(c)**) have validated this trend. The number of microspheres detected from three conditions are: 20002, 6523, 2361, respectively. According to Equation 3.1, the perfusion for three conditions are (in mL/min): 0.624, 0.502, 0.014. As a result, the FM technology has validated the accuracy of DCE-FI perfusion measurement.

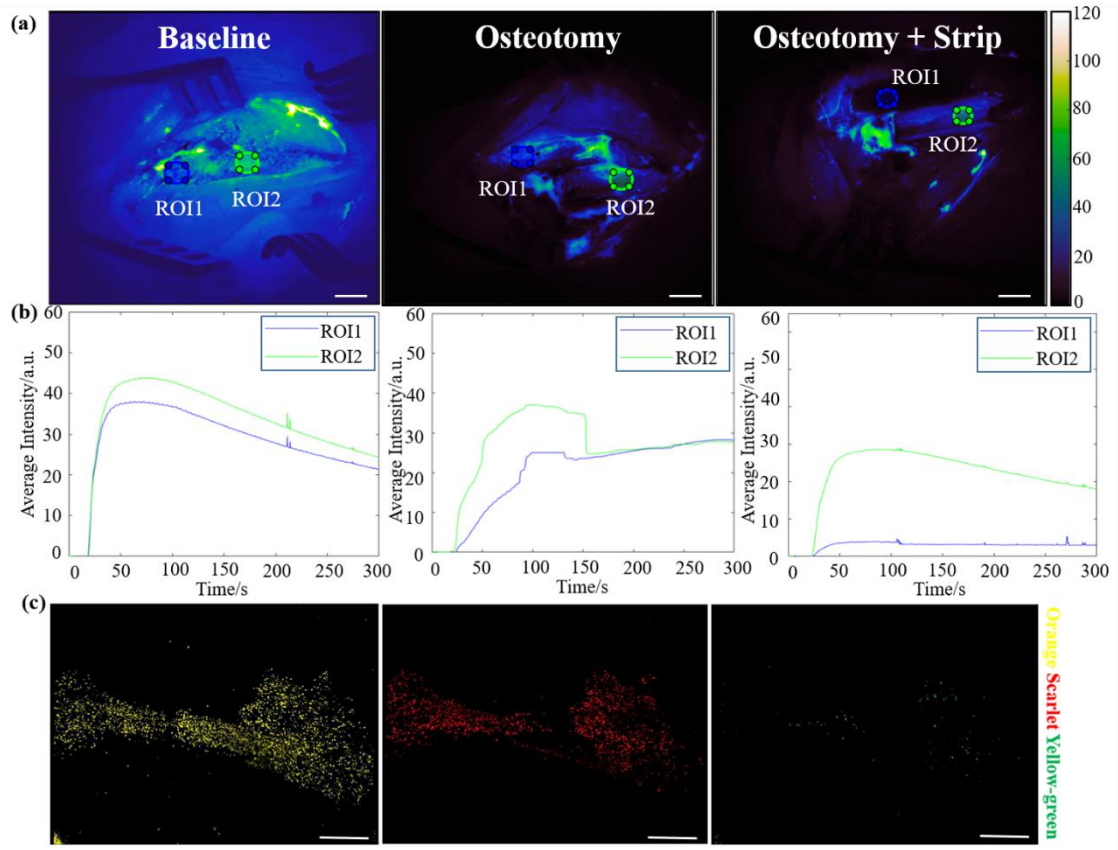

Figure 3.10: Fluorescence microsphere and DCE-FI animal study of three conditions. Left: Baseline, Center: Osteotomy, Right: Osteotomy and stripping. (a) Fluorescence images from DCE-FI at 200 s after imaging start time for each condition. Scale bars are 1 cm. (b) Temporal profiles of the average intensities of two ROIs for each condition. ROI1 is at distal side of the femur and ROI2 is at the proximal side. (c) 3D cryo-matrocome images of color-coded fluorescence microsphere volumetric density map for each condition. Scale bars are 2 cm.

3.4. Discussion and Conclusions

Assessing bone perfusion is important in orthopaedic surgery, because the success of procedures involving osteotomy and debridement are influenced by perfusion level. FGS utilizes the optical properties of fluorescent contrast agent to provide guidance. FM techniques have been developed to act as a 'gold standard' to measure perfusion in other FGS categories [252]. This study is the first one that applying FM technique in fluorescence-guided-orthopaedic-surgery. In this study, we aim to establish a repeatable

and accurate fluorescent microsphere-based blood flow measurement approach to validate our earlier developed dynamic contrast-enhanced fluorescence imaging technique for femur periosteal and endosteal blood flow detection. We successfully determined that fluorescent microspheres of four different colors could be accurately detected in controlled phantoms and evaluated their detection accuracy in real blood samples. Moreover, in the animal study, we have successfully segmented bone and its surrounding muscle, and then incorporated these volumetric renderings into the visualization. Meanwhile, FMs from bone segmentation as well as muscle segmentation has been recovered, their number has been counted, and they have been plotted in 3D space with color-coded spatial density. In this way, the bone perfusion level in both endosteal and periosteal regions can be estimated by converting from the FM density level based on the reference organ method. mQUIC direct comparison with DCE-FI technique have proved that FM technology is a useful validation tool, and DCE-FI technique is capable of accessing bone perfusion.

This study is the first animal study that can visualize bone perfusion in 3D. Compared to other fluorescence microsphere quantification methods such as direct counting and fluorescence intensity measurement, cryo-macrotome can not only provide quantitative information, but also produce volumetric density map about the spatial distribution and thus visualize the vasculature. Fluorescence microsphere was examined as a stable and accurate contrast agent that can be used both *in vitro* and *in vivo*. This property ensures the repeatability and usability of our proposed FM technology in pre-clinical and clinical study. DCE-FI model was validated by FM technology to be an accurate measurement of bone perfusion. It is the first time that we can prove a gold standard for DCE-FI.

In the future, we hope to enroll more animals to update this preliminary study into full study. Unfortunately, due to the difficulty gaining access to the macrocyrotome during the COVID 19 pandemic, since the team operating the system were not operating at full capacity, we could not complete the full set of planned experiments. Once we have more animals enrolled, then the quantitative perfusion results from mQUIC will be used to validate the dynamic contrast-enhanced fluorescence imaging method we have been developing in our lab. Establishing a reliable and high throughput FM technique based on mQUIC will also enable basic research into understanding the relationship between infection, trauma and perfusion in rodent models.

In conclusion, a mQUIC technique has been developed in this study, which used cryo-imaging system to produce 3D structural scanning and quantified perfusion by recovering FMs *in situ*. Bone perfusion can be visualized by FM distribution maps, and the level of FM density can reflect the level of bone perfusion. Therefore, mQUIC can work as a "gold standard" for bone perfusion measurement, and in particular, can validate the performance of DCE-FI derived perfusion-associated features.

Chapter 4

Low-Energy Fractured MRSA-Contaminated Rodent Femur Model for Correlating DCE-FI With Bioluminescent Imaging

This chapter is based on the work entitled "Dynamic contrast-enhanced fluorescence imaging characterization of MRSA-contaminated low-energy fracture model and correlated with bioluminescent imaging" by Han X, Demidov V, Sottosanti JS, Jiang S, Gitajn IL, and Elliott JT, which will be submitted to a peer-reviewed journal in the near future. Jonathan T. Elliott supervised the project and designed the experiments. I. Leah Gitajn and Shudong Jiang provided intellectual inputs. J. Scott Sottosanti designed 3D-printed hardware for phantom study. Valentin Demidov conducted the animal surgery, provided intellectual inputs, and assisted with data collection. The author of this thesis conducted phantom and animal experiments, collected and analyzed the data, and wrote the manuscript. This chapter has meet relevant copyright permissions.

This chapter presents the design of a low-energy fractured Methicillin-resistant *Staphylococcus aureus* (MRSA)-contaminated rodent femur model and its characterization by first-pass kinetics of dynamic contrast-enhanced fluorescence imaging (DCE-FI). Furthermore, the accuracy of DCE-FI analysis has been validated by correlation with the growth curves of bioluminescent labelled MRSA. This work extends from the characterization of bone viability in Chapter 5-6, and validates the clinical study of bone infection prediction in Chapter 7.

4.1. Introduction

Orthopaedic surgery is one of the most rapidly growing surgical procedure categories. One of the main post-surgery complications is bone infection that makes up 15.6% [4] of total complications. Bone infection can significantly reduce patient outcome and life quality, and may result in an amputation or even death. Furthermore, it is responsible for serious social and economic burdens [5]. Bones are more vulnerable to infection when nonviable regions and their surrounding tissues aren't sufficiently debrided, leaving behind non-viable tissues and foreign bodies. To provide guidance to surgical debridement for preventing bone infection, imaging modalities such as computed tomography and magnetic resonance imaging are used preoperatively. However, most of the current systems in imaging bone have complex systematic components that are difficult to be incorporated in surgical procedures, and acquiring images intraoperatively will lead to prolonged operational time [112].

Our group has been working on developing an intraoperative imaging modality, DCE-FI, that can provide precise debridement during orthopaedic surgery. DCE-FI works by administrating fluorescent contrast agent into patient's blood vessel and therefore blood perfusion can be traced and visualized. One advantage of DCE-FI is that it can provide both qualitative and quantitative information of perfusion. Tracer kinetic models such as adiabatic approximation to tissue homogeneity model [117,118] and Tofts model [90] have been developed to extract the quantitative information. Based on those models, our group has brought up with a bone specific model, hybrid plug/compartment (HyPC) model [21], to quantify endosteal and periosteal perfusion.

In this chapter, we propose a rodent osteomyelitis model, where we used bioluminescent imaging (BLI) to track the infection development of bone, and used DCE-FI to quantify perfusion changes before and after infection. Our central hypothesis is that DCE-FI can assess osteomyelitis-induced perfusion changes quantitatively in a predictable manner. Specifically, we will accomplish the following aims:

First, the technique to produce continuous growth of MRSA biofilm on titanium washer will be validate. A titanium implant will be used for fixing fractured bone pieces after trauma, which will receive MRSA inoculation. The goal of this part of the study is to validate that MRSA can form stable biofilm on titanium under the current laboratory setting. To achieve this goal, the formation of MRSA biofilm will be examined by measuring emitted bioluminescence signals from the titanium surface by BLI, which is further compared by the biofilm volume measured by optical coherence tomography (OCT), and the *in vitro* colony forming unit (CFU) counting.

Second, to establish a rodent osteomyelitis model after low-energy trauma. We have previously developed a new type of injury model-the blast overpressure tube injury to have a controlled level of trauma [253]. Here we propose to further incorporate the low-energy trauma injury with infection, due to its suitability for survival model. To complete this aim, we will 1) introduce low-energy fracture by the weight-dropped platform [254], 2) do surgery of bone stabilization, and 3) inoculate bioluminescent MRSA at fracture site.

Third, to develop the first-pass kinetic model for perfusion assessment in osteomyelitis. To complete this aim, we will 1) extract model-independent first-pass kinetic parameters including maximum intensity (Imax), time-to-peak (TTP), and ingress slope

(IS) from DCE-FI, 2) characterize the perfusion changes before and after osteomyelitis, and 3) compare with MRSA biofilm growth results from BLI.

4.2. Methods and Materials

4.2.1. Bacteria strain preparation

The bacterial strain used in this study is MRSA strain *SAP231* with bioluminescent protein *LuxCDABE*. The bacteria were firstly streak plated from frozen bacteria overnight on Tryptic Soy Agar (TSA) at 37 °C. Then a single colony was picked and incubated in 10 ml Tryptic Soy Broth (TSB) at 37 °C 200 rpm overnight. The optical density $(OD)_{600}$ of bacteria culture were measured for CFU estimation. A final OD_{600} of 1 were subsequently adjusted for resulting a 10^9 CFU.

4.2.2. Biofilm formation on titanium under static and dynamic condition

Autoclaved Titanium washers (0.14" inside diameter, 0.5" outside diameter) were first rubbed against sandpaper (grit 80, 3M Co.), cleaned with deionized water in an ultrasonic bath for 4 mins, and treated with 70% ethanol. For growth under static condition, Titanium washers were then transferred in a 24-well plate with flat bottom. Overnight bacteria culture was added to 1 mL of TSB to achieve the final concentration of approximately 10^8 CFU, and the culture were added into each well. The plate was then incubated at 37 °C, 5% CO_2 under static conditions. Bacteria culture media were changed every 24 hours for up to 3 days. For growth under dynamic condition, Titanium washers were then transferred in in-house designed 3D-printed microfluidic devices (**Figure 4.1**). Overnight bacteria culture was added to 1 mL of TSB to achieve the final concentration of

approximately 10^8 CFU, and the culture were added into each channel. The microfluidic channels were then incubated at 37 °C, 5% CO_2 under static conditions. Fresh broth was continuously pumped in at 1 µl/min, and waste solution was continuously pumped out at 1 µl/min.

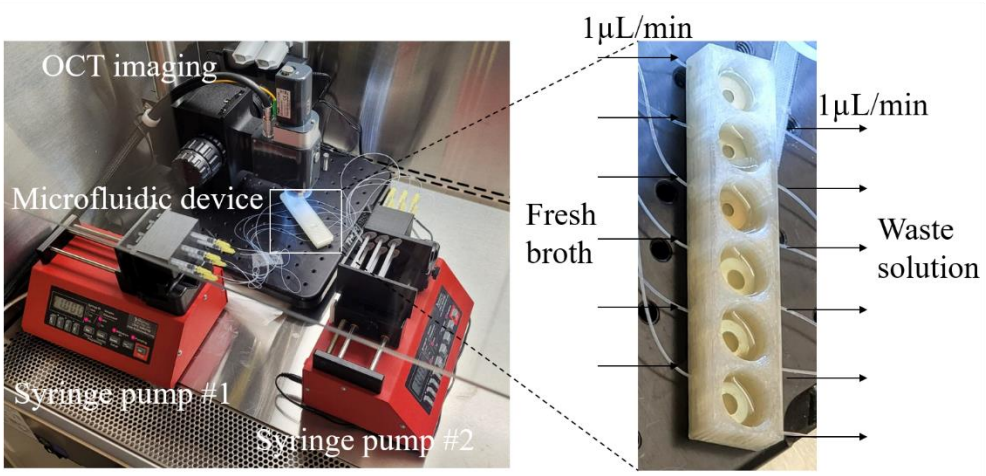

Figure 4.1. In-house built microfluidic device for biofilm growth under static condition. The device consists of an OCT system (Ganymede II, Thorlabs, Newton, NJ; 930 nm central wavelength, 36 kHz scan rate), a 3D-printed microfluidic channel with six repeated wells, and two programmable syringe pumps (BS-8000; Braintree Scientific, Braintree, MA). Fresh broth is continuously pumped in at 1 µL/min, and waste solution is continuously pumped out at 1 µL/min.

4.2.3. Bioluminescent imaging on titanium using IVIS system

At 0, 24, 48, and 72 hours after bacteria inoculation, bacteria culture media in one well was removed. Then the washer was washed by rinsing in Phosphate-buffered saline (PBS) to remove non-attached bacteria. The washers were then imaged by IVIS® Spectrum In Vivo Imaging System (PerkinElmer Inc. Waltham, MA) for measuring the radiance of bioluminescence (total flux, photons per second(s), [p/s]), using Living Image 4.7.3 software (PerkinElmer Inc. Waltham, MA). A circular region of interest with constant location and size over the washers was measured for its total bioluminescent signal.

4.2.4. OCT imaging

Microfluidic devices with titanium washers were imaged with commercial OCT system (Ganymede II, Thorlabs, Newton, NJ; 930 nm central wavelength, 36 kHz scan rate). OCT axial and lateral resolutions in air were 6 and 15 μm, respectively. White-light microphotographs of each well were taken prior to imaging with the camera built in the OCT probe. Three-dimensional images of each well containing 500 x 500 x 5000 voxels (1.4 mm deep x 1 mm wide x 10 mm long) were prepared for further processing by compensating for exponential depth-decay of the OCT signal and manually segmenting each well in MATLAB. Full details in OCT image processing and segmenting were stated in [255]. Biofilm volume was visualized by setting a 10% threshold to cut off the noise originating from the flowing medium.

4.2.5. In vitro colony forming units counting

The biofilm was removed by placing the washers into 10 ml of PBS in a 50 ml Falcon tube (Corning Inc.) and sonicating at a frequency of 35 kHz for 15 min in an ultrasonic water bath. Sonication was repeated three times with a 30 s interval for vortexing in between. A 10-fold dilution was prepared from the solution, and the diluted samples were plated onto a TSA for enumeration of MRSA CFUs after 24 h of incubation at 37 ˚C, 5% CO_2. The colonies were expressed on the basis of calculated washer area as CFU/cm^2.

4.2.6. Animal study

We seek to establish and refine a rodent osteomyelitis model following low-energy trauma (Institutional Animal Care and Use Committee (IACUC) number-00002265). This

model includes weight-dropped injury to the femur, surgical stabilization by plate fixation, and bacteria inoculation in trauma sites. This is a pilot proof-of-concept study and contains 2 animals.

At day of injury and survival surgery (Day 0), animals were induced and maintained with isoflurane. Animals were given a perioperative dose of analgesia to ensure uninterrupted analgesic coverage. The first bioluminescence imaging (**BLI #1**) was acquired. The rat legs were shaved and prepped for surgery. The first DCE-FI imaging (**DCE-FI #1**) was acquired. Animal legs were placed over the platforms of the fracture device (ventral side up). A blunted blade placed at the midshaft of the femur. The blade is carbon steel with a width of 15 mm and a thickness of 2 mm. The notch that fits over the femur measures 13.35 mm. A weight of 0.94 kg was dropped from 15.3 cm, which impacts the blunted blade delivering a calculated force of 104.80 Newtons. The legs were opened and blunt dissected to expose femur. Up to 8 mg/kg bupivacaine was injected subcutaneously at the site of planned incision. Under continuous anesthesia, the incision was made at the location of the penetrating wound, and the bones were exposed, taking care not to worsen the soft-tissue and periosteal damage. The second DCE-FI imaging (**DCE-FI #2**) was acquired. Bioluminescence-labelled MRSA inoculation was done at this time, and 10 uL of inoculum containing 10^8 CFUs was placed directly onto the wound by a 22-gauge Hamilton syringe after the ends of the fracture were exposed and left for 1 h. Then devitalized bones and tissues were removed. Debridement were conducted using a ronjuer, curette and pneumatic burr drill. Animals were fixed using titanium plates. A 4-hole plate, 23 mm long, 3 mm wide and 0.5 mm in thickness, was positioned on the anterolateral femoral shaft and held in place by 1.2-mm self-tapping bicortical screws in

proximal and distal holes. Holes were pre-drilled prior to placement of each screw. Animal legs were sutured closed and placed in post-operative recovery. The wound was then closed using the following suture material: for muscle or subcutaneous tissue, an absorbable suture of size 4-0 to 6-0 with a simple continuous closure pattern; skin was closed using a non-absorbable suture of size 4-0 to 6-0 with a simple interrupted suture pattern. Following closure, the wound was aseptically cleaned. The second bioluminescence imaging (**BLI #2**) was acquired. Rats were individually housed and allowed special chlorophyll-free rat chow water *ad libitum*.

At healing period (Day 1-6), analgesia doses were administered to the animals, and **BLI #3-5** were captured every three days from Day 1 to Day 6 to monitor bacteria growth.

At day of euthanasia (Day 7), animals were induced and maintained with isoflurane. **BLI #6** was acquired, and quantification of bacteria was compared with *in vitro* CFU. The legs were opened and blunt dissected to expose femur. After induction with anesthesia, the incision was made at the same site as the previous incision, and the femur was re-exposed. Hardware was removed, and imaging was performed (**DCE-FI #3**). Isoflurane was increased to cause overdose, and animals were euthanized.

4.2.7. DCE-FI imaging

In Vivo imaging was performed using a custom-built wide-field fluorescence imaging system. An operating microscope was modified to include two PCO Panda fluorescent cameras measuring emission at 700 nm and 800 nm, respectively. A color camera was also mounted, which can measure RGB under white-light illumination, and 780 nm emission from indocyanine green (ICG). Using this system, all three channels were

simultaneously recorded to allow for the in vivo imaging. RGB images are acquired throughout, allowing for motion correction, and co-registration to the static images of ICG. These occurred during the survival surgery (Day 0) and the non-survival surgery prior to euthanasia (Day 7).

Rodents were placed under a surgical plane of anesthesia with isofluorane (1-3% in O_2 at 0.5 – 1.0 L/min). They were placed on a heating pad (temperature will be checked and kept between 35.9 and 37.5 ˚C) and the above fluorescence imaging system was positioned over the imaging field. During image acquisition, 0.2 mL 0.1 mg/kg ICG was injected intravenously, given by catheter injection. Imaging was performed for approximately 5 minutes. To allow ICG to clear, approximately 20 minutes were allowed between each ICG Imaging session.

4.2.8. Image processing, kinetic analysis, and statistical analysis

Fluorescence images from fluorescence imaging system were exported as stacked .tiff files and processed by custom MATLAB (The MathWorks, Natwick, MA) programs: fluorescence images were normalized by subtracting the median intensity of images from the first 10 seconds, designed to remove the residual ICG signal from previous injections; Then fluorescence images and white-light images were co-registered using the modified Image Processing Toolbox of MATLAB.

Processed images were then analyzed of their first-pass kinetics. In each time series of fluorescence images, equal-sized regions-of-interest (ROIs) covering all exposed femur regions were selected. For each ROI, model-independent first-pass kinetic parameters (FI parameters): maximum intensity, time-to-peak, and ingress slope of dye wash-in phase

(denoted by *Imax*, *TTP,* and *IS*, respectively) were extracted from temporal fluorescence intensity (FI) curve that was averaged over the pixels covered by the ROI: *Imax* was obtained as the intensity at the time of peak of whole image series; *TTP* was obtained as the time from dye arrival time (*Ta*) to the time of peak of whole image series; *IS* were obtained by fitting a straight line to the ingress curve of wash-in phase.

Bioluminescent images from IVIS imaging were exported as DICOM files, and were processed by MATLAB. Total flux (p/s) of each ROI were recorded. For visualization purpose, same range of color bar should be used to represent the temporal changes in bioluminescent signals. For each ROI, total flux and FI parameters were compared using bar graph.

4.3. Results

4.3.1. MRSA biofilm growth on titanium washers

Under both static (**Figure 4.2**) and dynamic (**Figure 4.3**) culture conditions, the surfaces of MRSA-contaminated titanium washers showed increasing bioluminescent signals from 0-72 hours. *In vitro* CFU counting (**Figure 4.2(c)**) of 0 hour yields 0 CFU, and > 10,000 CFU after 24 hours, which proved the continuous growth of MRSA biofilm. OCT imaging (**Figure 4.3(c)**) also showed that biofilm has formed after 72 hours. The resulted MRSA growth curves (**Figure 4.2(b)** and **Figure 4.3(b)**) are consistent with the biofilm coverage curve from literature [256].

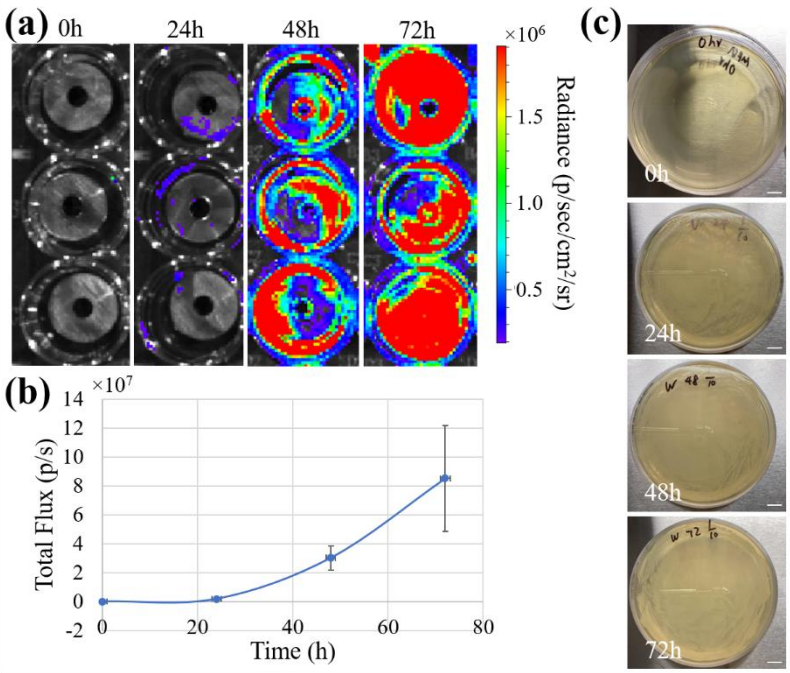

Figure 4.2. MRSA biofilm growth under static condition. (a) Bioluminescent images of three repeated experiments (Row 1~3) from 0, 24, 48, and 72 hours culture duration (Column 1~4). (b) MRSA biofilm growth curve. Averaged total flux over three repeated experiments is plotted against the culture duration. Scale bar is standard deviation. $n = 3$. (c) *In vitro* CFU counting. Samples were 10-fold diluted. Scale bar = 1 cm.

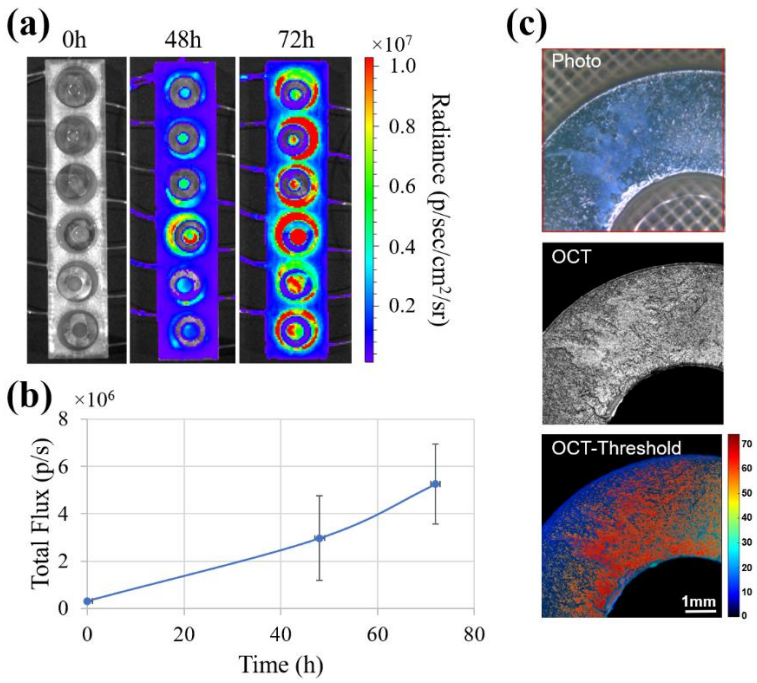

Figure 4.3. MRSA biofilm growth under dynamic condition. (a) Bioluminescent images of six repeated wells from 0, 48, and 72 hours culture duration (Column 1~3). (b) MRSA biofilm growth curve. Averaged total flux over three repeated experiments is plotted against the culture duration. Scale bar is standard deviation. $n = 6$. (c) OCT imaging. Top: photograph of one well after 72 hours culture; Center: OCT raw image of the same well; Bottom: 10% threshold OCT image of the same well. Scale bar = 1 mm.

4.3.2. MRSA biofilm growth on low-energy fractured femur

Before MRSA inoculation, the femur was judged to be free from MRSA and no bioluminescent signals were detected (**Figure 4.4(a)**, Column 1). Right after MRSA inoculation, bioluminescent signals were detected (**Figure 4.4(a)**, Column 2), demonstrating that MRSA has successfully attached to the surface of low-energy fractured femur. During the 1st to the 7th day after inoculation, a continuous increase of bioluminescent signals was detected from the femur (**Figure 4.4(a)**, Column 3-5, and **Figure 4.4(b)**), showing that a stable MRSA biofilm has grown on the low-energy fractured femur.

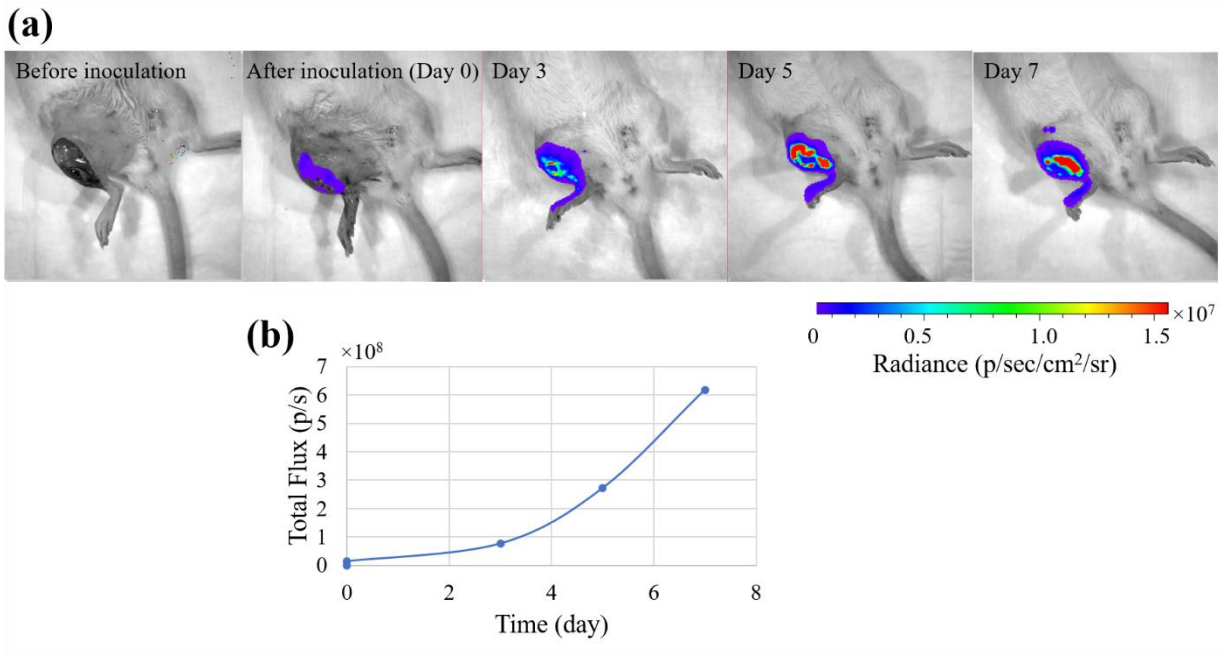

Figure 4.4. MRSA biofilm growth on low-energy fractured femur. (a) Bioluminescent images of rodent No. 1 before MRSA inoculation, and at 0, 3, 5, and 7 days after MRSA inoculation (Column 1~5, respectively). (b) MRSA biofilm growth curve. Total flux from the same region-of-interest covering the femur is plotted against the culture duration.

4.3.3. DCE-FI in low-energy fracture associated MRSA infection

As the rodent femur goes from baseline (**Figure 4.5**, Left) to low-energy fracture (**Figure 4.5**, Center) and then to MRSA infection (**Figure 4.5**, Right), the overall fluorescence intensity of DCE-FI was continuously decreased (**Figure 4.5(a)**), and the average intensity curves have changed from regular to irregular (**Figure 4.5(b)**). First-pass kinetic parameters—Imax, TTP, and IS—have also shown constant changes in these three conditions (**Figure 4.5(c)**). In details, Imax and IS are decreased, and TTP is increased (**Figure 4.5(d)**). This change in first-pass kinetic parameters is consistent with the results from the human fracture-associated infection study in Chapter 7. As a result, DCE-FI can quantitatively characterize the vascular changes in fracture-associated MRSA infection.

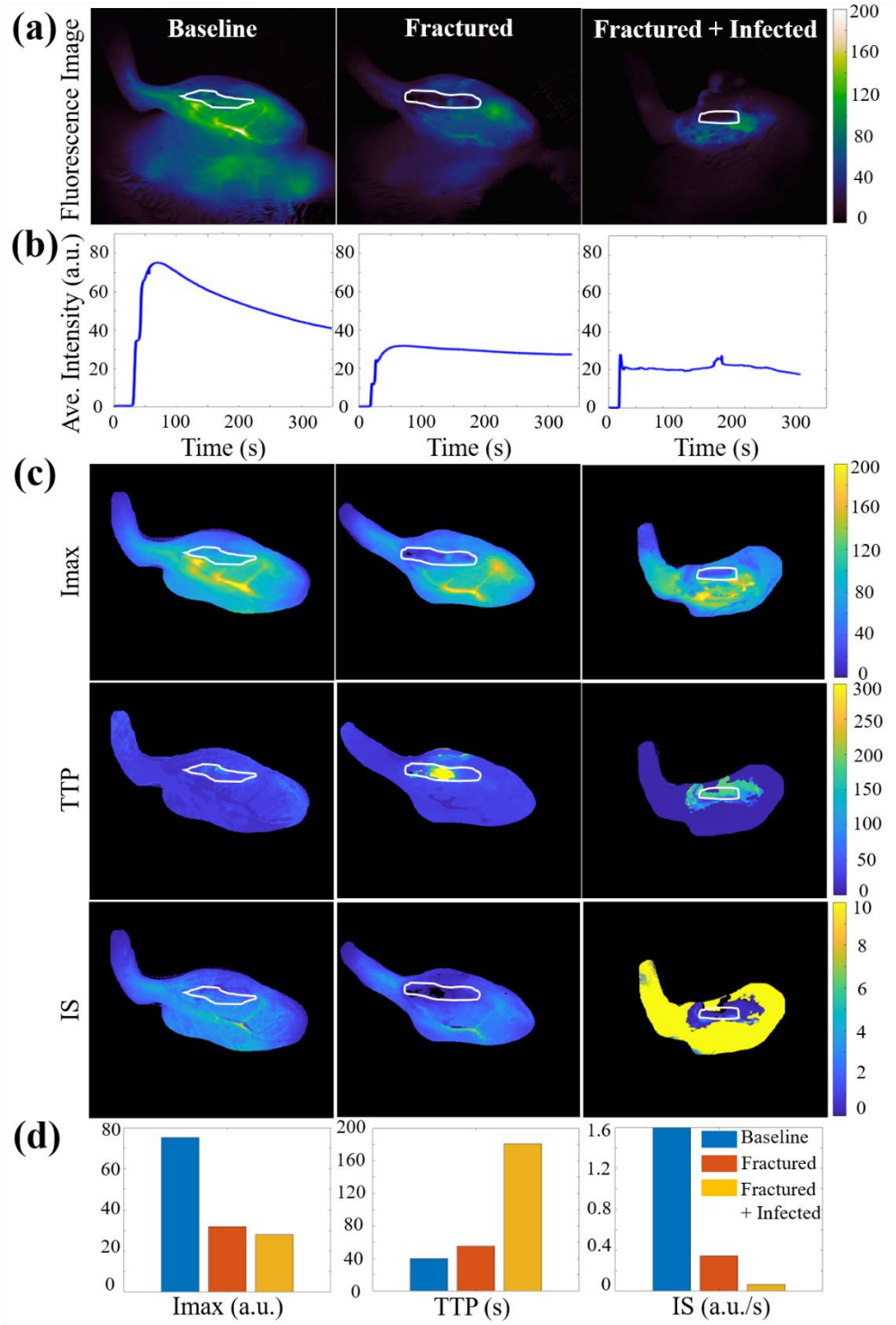

Figure 4.5. DCE-FI images, temporal curves, and first-pass kinetics in low-energy fracture associated MRSA infection from Rodent No. 1. (a) DCE-FI fluorescence images of three conditions. Left: Baseline, Center: Fractured, Right: Fractured + Infected. White solid lines denote the ROIs. (b) DCE-FI temporal curves of each ROI. (c) DCE-FI first-pass kinetics. Top: Imax, Middle: TTP, Bottom: IS. (d) Bar graph of comparing DCE-FI first-pass kinetic parameters

under three conditions. Blue = Baseline, Dark red = Fractured, Dart yellow = Fractured + Infected.

4.3.4. Perfusion decrease characterized by DCE-FI first-pass kinetics is correlated with infection

After MRSA contamination, the perfusion levels were decreased, as characterized by DCE-FI first-pass kinetic parameters (**Figure 4.6**, Column 1-3). In comparison, MRSA infection levels were increased, as demonstrated by BLI signals (**Figure 4.6**, Column 4). Therefore, perfusion decrease is correlated with infection development, and DCE-FI is able to quantify the change.

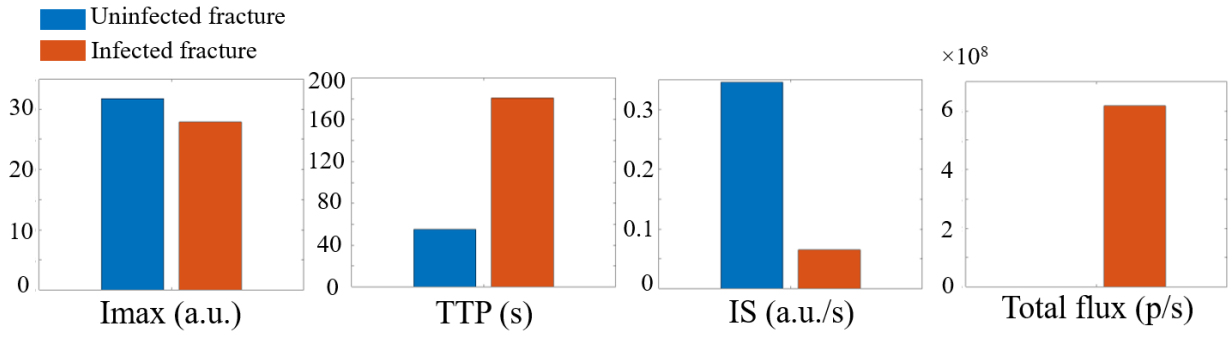

Figure 4.6. Changes in DCE-FI first-pass kinetic parameters and BLI signals after bone infection. Column 1-3: DCE-FI first-pass kinetic parameters Imax, TTP, and IS. Column 4: BLI signal in total flux. Blue = uninfected bone, Dark red = infected bone.

4.4. Discussion and Conclusions

This is the first pilot preclinical study to evaluate the performance of DCE-FI in assessing bone perfusion status related to infection. The study consists of two parts: phantom study and animal study. In the phantom study, we designed a MRSA biofilm growth model using titanium washers. Titanium is one of the prevalent metals in orthopaedic implants, due to its biocompatibility, high corrosion resistance and mechanical

properties [257]. Currently, many groups have studied the MRSA biofilm formation on titanium implants [258–260]. However, the MRSA growth curves have shown variations under different culture conditions. To establish a stable growth curve under the current laboratory settings, we conducted this titanium phantom study. A stable growth on titanium is the basis for the following animal study, because in the animal study we will inoculate MRSA on titanium implant and track the biofilm formation *in vivo*. For producing the MRSA growth curve, we used BLI for tracking the growth of MRSA biofilm, and validated it by *in vitro* CFU counting or OCT scan.

In the animal study, we demonstrated a DCE-FI quantitative first-pass analysis method in a rodent osteomyelitis model. In this model, the microvascular changes associated with osteomyelitis were captured by DCE-FI, and the infection development was tracked by BLI. A comparison of these two imaging modalities has demonstrated that perfusion level decreased as infection developed. Therefore, DCE-FI can be potentially used to track the status of osteomyelitis by the way of tracking the decrease in perfusion.

In the future, we will further develop the DCE-FI osteomyelitis model to segment the bones into infected/uninfected regions, and most importantly, will display accurate contours between the segments. These contours will provide guidance for debriding infected bones, which makes our proposed model a useful tool that has high clinical potential.

In conclusion, DCE-FI can quantify infection-induced perfusion decrease post bone fracture, by first-pass kinetic analysis.

Chapter 5

First-pass Kinetic Parameters and Arterial Input Function Characterization of Amputation

This chapter adapted from the content of work entitled "First pass kinetics of dynamic contrast-enhanced fluorescence imaging in lower limb amputations: model-independent characterization and classification in perfusion states" by Han X, Elliott JT, Tang Y, Sottosanti JS, Hall A, Jiang S, and Gitajn IL, submitted to *The Journal of Bone and Joint Surgery* in 2023. I. Leah Gitajn, Shudong Jiang, and Jonathan T. Elliott co-supervised the project, provided intellectual insights and reviewed the manuscript. Amy Hall assisted with clinical trial and data collection. J. Scott Sottosanti developed hardware and 3D-printed parts for the imaging system. Yue Tang contributed to image processing and arterial input function (AIF) processing. The author of this thesis analyzed the patient data, processed the images, wrote analytic software and wrote the manuscript. This chapter has met copyright permission requirements.

This chapter describes the development of first-pass kinetic analysis and AIF characterization on dynamic contrast-enhanced fluorescence imaging (DCE-FI) of orthopaedic amputation surgery. First-pass kinetic analysis approach is based on model-independent quantitative analysis of DCE-FI, where maximum intensity, time-to-peak, ingress slope, and egress slope were extracted from temporal intensity curves. To account for the intersubjective variations caused by AIF-associated factors, here we also proposed an AIF simple correction algorithm that will correct the first-pass kinetic parameters by average AIFs. This approach has shown high classification scores in respect of stratifying

bone injury levels. Therefore, this approach will have possible applications in assisting the orthopaedic amputation surgery with precise debridement.

5.1. Introduction

Adequate perfusion is necessary for the proper functioning of the skeletal system's physiological activities—including growth and strength, fracture repair and healing—by delivering oxygen, nutrients, antibiotics and immune cells to bone [14,33,34,36,37]. Inadequate perfusion, especially in the context of trauma, can lead to infection, necrosis and other complications [40–42]. Poorly perfused bones will form microbial biofilm and deficit function, which may lead to recurrent infection, repeat surgery and prolonged morbidity [6–9,40–42]. Therefore, quickly and accurately assessing bone perfusion is a key unmet need in orthopaedic surgery.

Dynamic contrast-enhanced (DCE) imaging modalities, such as DCE-computed tomography (DCE-CT), DCE-magnetic resonance imaging (DCE-MRI), and DCE-FI, are used in tumor detection [85] and characterization of vasculature [86]. DCE works by measuring the temporal intensity changes of injected contrast agent, and computing quantitative spatial and temporal information. Compared to MRI and CT, DCE-FI has the advantage of being non-ionizing, low-cost and providing real-time information in the operating room [112].

To assess bone perfusion and provide guidance for surgical debridement, a few research groups have explored DCE-FI using the contrast agent indocyanine green (ICG). While these have been described in recent preclinical studies [19,21,97,261–263], only a limited number of clinical investigations have demonstrated the method intraoperatively. Approaches commonly used in DCE-FI analysis include Tofts model [182] and Adiabatic approximation to the tissue homogeneity (AATH) model [117,118]. These explicit methods of analysis provide some additional quantitative information, but are limited in

their complexity, and therefore, do not account for differences between patients in the delivery of the dye to the tissue of interest. The lack of an AIF in most of these reports suggests a high amount of variance in the resulting data [128]. This variance will make it impossible to define threshold based on kinetic parameters.

In this paper, we propose a simple quantitative approach to analyzing DCE-FI data obtained from a clinical investigation of lower-limb amputations. Three surgical conditions were created in each patient's tibia who underwent amputation surgery, designed to mimic three levels of bone blood flow disruption: (1) *baseline* (intact bone, low blood flow disruption); (2) *osteotomy (*bone cut 15cm from the medial malleolus to disrupt endosteal blood flow, middle blood flow disruption); (3) *osteotomy and stripping* (extensive soft tissue stripping proximal and distal to the osteotomy to disrupt both endosteal and periosteal blood flow, high blood flow disruption). ICG was administered during each of three conditions, for correlating DCE-FI data to specific level of blood flow disruption. The approaches in this paper are using first-pass kinetic parameters [264–269] of DCE-FI data to characterize and classify bone perfusion, and using an AIF simple correction algorithm to reduce inter-subject variations. To our knowledge, this is the first published DCE-FI investigation in humans. This paper examined the application of DCE-FI in intraoperative bone state assessment, and will inspire future studies on DCE-FI in orthopaedic surgeries.

5.2. Methods and Materials

5.2.1. Patient study

The study design is prospective cohort study. The patient study was conducted at Dartmouth-Hitchcock Medical Center (DHMC), and approved by the Institutional Review Board of DHMC and listed on ClinicalTrials.gov as NCT04250558. Fifteen participants with confirmed below knee amputation (BKA) were included in this study. Eligible participants are selected as 18 years of age or older who present to DHMC and scheduled for a lower extremity amputation. Iodine allergy and pregnant or breastfeeding woman have been excluded from this study. Information about the recruited participants is listed in **Table 5.1**. 53.3% of participants have their foot removed prior to imaging (*i.e.,* Foot-off patients without retro blood supply). Recruitment, exposure, and data collection periods of participants were January 2020 to August 2022, and this study is a one-time imaging during the subject's surgery so no follow-up visits. Informed consent was obtained from the participants and/or their legal guardians. All methods were performed in accordance with the relevant guidelines and regulations.

Table 5.1: Study participants information. BKA – below knee amputation. pt-patient. BMI-body mass index, HR-heart rate, RR-respiratory rate, SaO2-oxyhemoglobin saturation, Hb-hemoglobin concentration, EF-ejection fraction.

	BKA patient cohort
Foot removal prior to imaging	
No	7 (pt1~7)
Yes	8 (pt8~15)
Gender	
Male	13
Female	2
Pre-operation diagnosis	
left BKA	3
Right BKA	12

Age (years)	55.2±13.2
BMI (kg/m^2)	30.9±8.0
HR (beats per minute)	79.3±14.4
RR (breaths per minute)	15.2±3.7
SaO_2 (%)	97.4±2.6
Hb (g/dL)	10.8±1.9
EF (%, if applicable)	55.7±11.1

In the study, three surgical conditions were created in each patient's tibia, designed to mimic three levels of bone blood flow disruption after low-to-high energy fracture. An intravenous injection of 0.1 mg/kg ICG was as administered during each of three conditions: (1) *baseline*; (2) *osteotomy (*bone cut 15cm from the medial malleolus to disrupt endosteal blood flow, similar to a low-energy fracture); (3) *osteotomy and stripping* (extensive soft tissue stripping proximal and distal to the osteotomy to disrupt both endosteal and periosteal blood flow, similar to a high-energy fracture). Imaging was performed during the wash-in and wash-out of contrast. These manipulations did not add appreciably to the duration of surgery.

5.2.2. Fluorescence imaging instrumentation and acquisition

Time series of fluorescence images were recorded from 20 seconds before to 4 minutes after ICG injection in each condition, using SPY Elite imaging system (Stryker Corp., Kalamazoo, MI, USA). After fluorescence images were acquired, a white-light image was taken. The working distance was 300 mm, and light intensity and integration times were kept constant during the whole imaging process. During each imaging session,

an in-house built ICG pulse dye densitometer has been placed on the patient's finger to acquire an AIF during ICG injection based on the pulse oximeter.

5.2.3. Image processing

5.2.3.1. Motion correction

DCE-FI images were exported as DICOM files from SPY Elite imaging system and loaded to custom MATLAB (The MathWorks, Natwick, MA) programs to correct for motion artifacts. The correction was achieved by finding the highest mutual information between every two reference-target frame pair, continuously from start frame to last frame. In detail, first, the start frame was located by skipping any earlier frames that have an average intensity of less than 10, and the start frame was set as the reference frame. Second, the next frame after the reference frame was set as the target frame, and was aligned to the reference frame by finding the maximum mutual information along x and y-axis using a 3 × 3 kernel search. Third, the aligned frame was set as the new reference frame, and repeated step 2~3 until reached the last frame. At the end, the whole series of aligned DCE-FI images were saved. Further details can be found at [270].

5.2.3.2. Image pre-processing

Motion corrected images were then pre-processed by custom MATLAB programs: Firstly, images were normalized by subtracting the median intensity of images from the first 10 seconds, for removing the residual ICG signal from previous injections. Secondly, images were trimmed by deleting the frames of the first 20 seconds, to account for the light

sources warm-up period. Thirdly, fluorescence images and white-light image were co-registered using Image Processing Toolbox.

5.2.3.3. First-pass kinetic analysis

For each time series of fluorescence images, six circular regions-of-interest (ROIs) with the same radius (1 ± 0.2cm, varied with bone width) were selected to startle the osteotomy proximally (P1-P3) and distally (D1-D3). For each ROI, model-independent first-pass kinetic parameters (FI parameters) were extracted from temporal fluorescence intensity (FI) curve that was averaged over all pixels in the ROI (**Figure 5.1(a)**): Maximum intensity (*Imax*) was obtained as the intensity at the time of peak of whole image series; Time-to-peak (*TTP*) was obtained as the time from dye arrival time (*Ta*) to the time of peak of whole image series (*Tp*); Ingress slope (*IS*) was obtained by fitting a straight line to the ingress curve of wash-in phase.

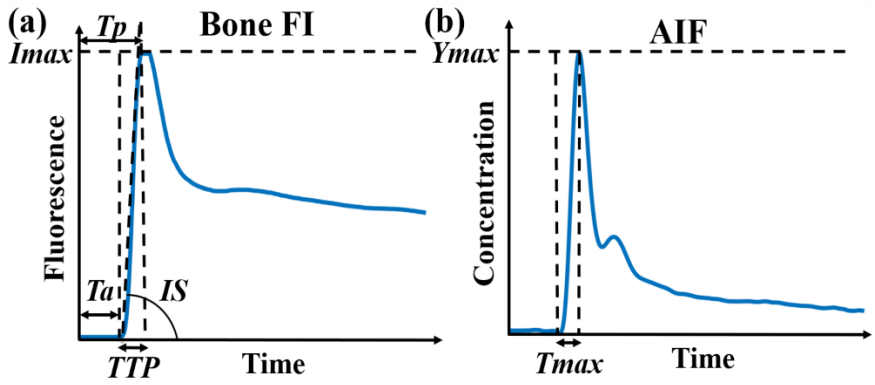

Figure 5.1: First-pass kinetic parameters extraction. (a) Extraction of FI parameters. Averaged fluorescence intensity of bone ROI is plotted over time. FI parameters-Imax, IS and TTP were extracted out of the curve as indicated. (b) Extraction of AIF parameters. AIF of an imaging session is plotted over time. AIF parameters-Ymax and Tmax were extracted out of the curve as indicated.

5.2.4. Arterial input function simple correction

5.2.4.1. AIF pre-processing

Arterial input functions were measured by in-house built ICG pulse dye densitometer based on the pulse oximeter. Within the densitometer, the AIFs were calculated from the ratio of amplitudes of two channels of the pulse oximeter, extinction coefficients of oxyhemoglobin, deoxyhemoglobin and ICG at given wavelengths, clinically-recorded arterial oxygen saturation, and total hemoglobin concentration. The raw AIFs were then preprocessed by subtracting the median of the baseline before the ICG injection, aligning the arrival time point to the origin and extrapolating if the length of recorded AIF was not long enough.

5.2.4.2. AIF parameter extraction and cleaning

Arterial input function first-pass parameters—maximum concentration and time-to-peak (denoted by *Ymax* and *Tmax*, respectively)—were extracted from AIF curves of each imaging session (**Figure 5.1(b)**). However, the AIF curves from some participants were partially or completely problematic due to the artifacts (*i.e.,* missing, low signal-to-noise ratio, or motion) in AIF acquisition process. To address this problem, we cleaned raw AIF parameters by the following method according to a previous study, which shown that substituting individual AIF with a population averaged AIF has no significant differences between pharmacokinetic parameters [271]. Standard AIF parameters (denoted by *Ymax'* and *Tmax'* respectively) were calculated by averaging over nine participants whose AIF curves were completely without artifacts. Then data falls outside the 95% confidence interval was regarded as outlier and replaced with standard AIF parameters.

5.2.4.3. AIF simple correction

Arterial input function perturbations caused by the variations of dye dose, dye dispersion time and injection fraction can result in 60% to 200% error in first-pass kinetic parameters [128]. Therefore, comparing raw first-pass kinetic parameters may introduce bias. To account for the AIF-dependent effects and allow intra- and inter-subject comparison, tissue temporal FI curves are usually processed by convolutional correction [128].

However, there are some limitations of the convolutional correction, such as prolonged computational time, sensitivity to de-convolution/re-convolution algorithm, and requiring complete AIF curve. To overcome the above limitations, here we proposed a model-free simple correction approach that correct only the first-pass kinetic parameters instead of the whole FI curves. The corrected bone first-pass kinetic parameters *Imax_c*, *TTP_c* and *IS_c* are computed by:

$$Imax\_c = Imax/Ymax \times Ymax' \tag{5.1}$$

$$TTP\_c = TTP - Tmax + Tmax' \tag{5.2}$$

$$IS\_c = Imax\_c/TTP\_c \tag{5.3}$$

Where *Imax*, *TTP* and *IS* are the raw first-pass kinetic parameters, *Ymax* and *Tmax* are the individual AIF parameters, and *Ymax'* and *Tmax'* are the standard AIF parameters acquired in section 5.2.4.2.

5.2.5. Statistical analysis and machine learning classification

First-pass kinetic parameters were grouped according to their ROI location and patients' foot removal status: *Group1-distal ROI, foot-on, Group2-distal ROI, foot-off,* and

Group3- proximal ROI, foot-on and foot-off. The three groups were determined as the foot removal status has influenced on the distal ROIs but not on the proximal ROIs. In each group, mean and standard deviation were calculated and compared within baseline, osteotomy, and osteotomy + stripping states. All results were statistically examined by paired student's t-test using MATLAB Statistics and Machine Learning Toolbox, and results with p-value less than 0.05 were regarded as statistically significant. Missing data and outliners were deleted from the dataset.

For machine learning classification in perfusion states, ROIs were labeled as "*Normal*", "*Minor Injured*" or "*Major Injured*" classes according to the degree of disruption to bone perfusion resulting from manipulations: "*Normal*" and "*Minor Injured*" ROIs were defined as having arterial and/or retrograde perfusion, resulted from no bone damage or bone damage from either osteotomy or foot cutting. ROIs from these two classes both have sufficient healing potentials. "*Major Injured*" ROIs was defined as having neither arterial nor retrograde perfusion, caused by any two co-occurring bone damages from osteotomy, soft tissue stripping and foot cutting. ROIs from this class have insufficient healing potentials due to reduced blood supply. Corrected first-pass kinetic parameters were statistically tested by two-sample student's t-test. Using corrected first-pass kinetic parameters as predictive variables, a one-vs-one three-class classification and two one-vs-rest binary-class classifications have been done by Gaussian Naïve Bayes classifier (Scikit-learn, Python 3.9). 10-fold cross-validation was used to evaluate the classifier. Accuracy, sensitivity, specificity and area-under-curve (AUC) from receiver operating characteristic (ROC) curves have been recorded and averaged over all cross-validation rounds.

5.3. Results

5.3.1. DCE-FI is able to demonstrate the vasculature changes both spatially and temporally

Dynamic contrast-enhanced fluorescence imaging can locate the vasculature changes. As shown in the fluorescence images (**Figure 5.2**), fluorescence intensities in baseline (**Figure 5.2** Column 1), osteotomy (**Figure 5.2** Column 2), and osteotomy + stripping (**Figure 5.2** Column 3) states was significantly decreased, consistent with the fact that blood flow by endosteal and periosteal supply has been increasingly disrupted during orthopaedic surgery. Moreover, perfusion at proximal and distal sites was the same in foot-on patients (**Figure 5.2 (a)**) who have retrieved perfusion from foot, while it was different in foot-off patients (**Figure 5.2 (b)**) who have no retrieved perfusion.

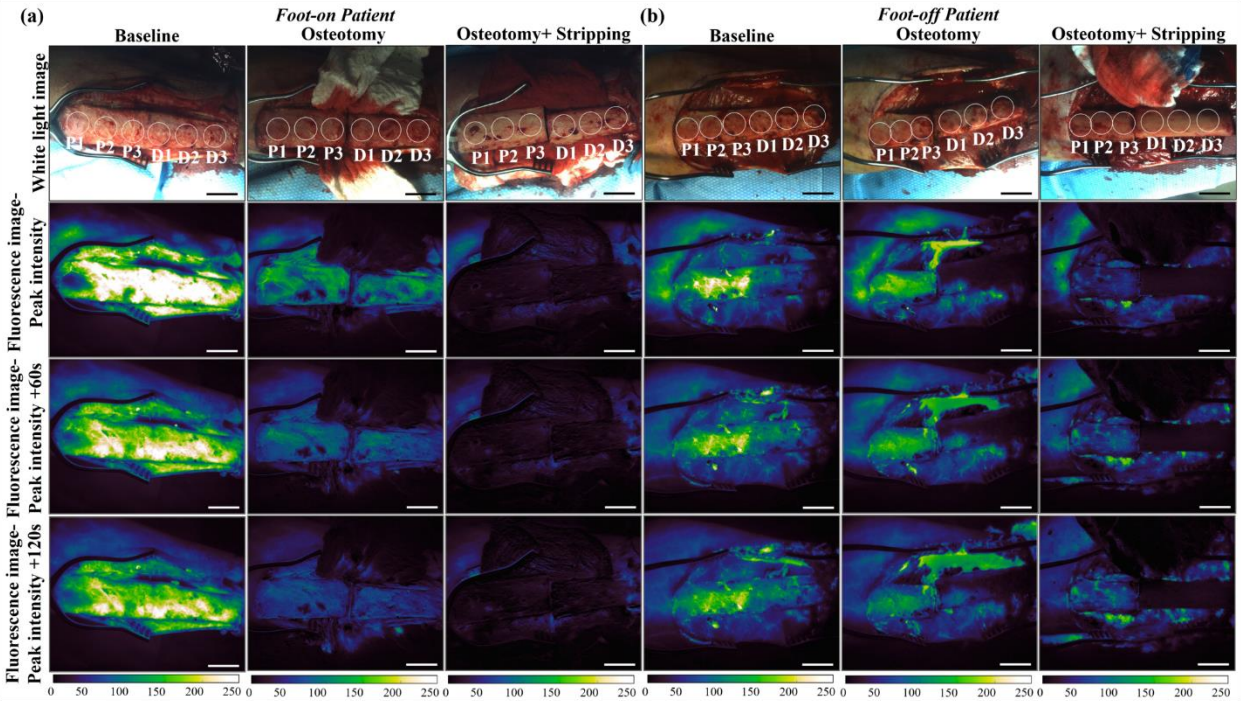

Figure 5.2: DCE-FI images. (a) A foot-on patient (pt4, a 52-year-old woman with right BKA) and (b) a foot-off patient (pt10, a 53-year-old woman with right BKA). Row 1: White light images from white light camera; Row 2-4: Fluorescence images from near infrared camera at global time of peak intensity (t = Tp), peak intensity plus 60 seconds (t = Tp + 60 s), and peak intensity plus 120 seconds (t = Tp + 120 s), respectively; Circles indicate the ROIs (P1~P3,

D1~D3, respectively). Column 1-3: Baseline, Osteotomy, and Osteotomy + Stripping. Scale bars = 3cm. P: Proximal, D: Distal.

Temporal intensity changes in DCE-FI can also reflect vasculature conditions. As shown in **Figure 5.3**, compared to baseline condition: *Imax* and *IS* showed continuously decreasing in osteotomy and osteotomy+stripping conditions, with the largest decreasing percentages in foot-off patients' distal bones (**Figure 5.3 (b)**); *TTP* showed no significant changes in osteotomy, but in osteotomy+stripping have increased. In comparison, averaged AIF keep constant in different states of both foot-on and foot-off patients (**Figure 5.3**, Row 7), demonstrating that AIF is independent of bone vasculature.

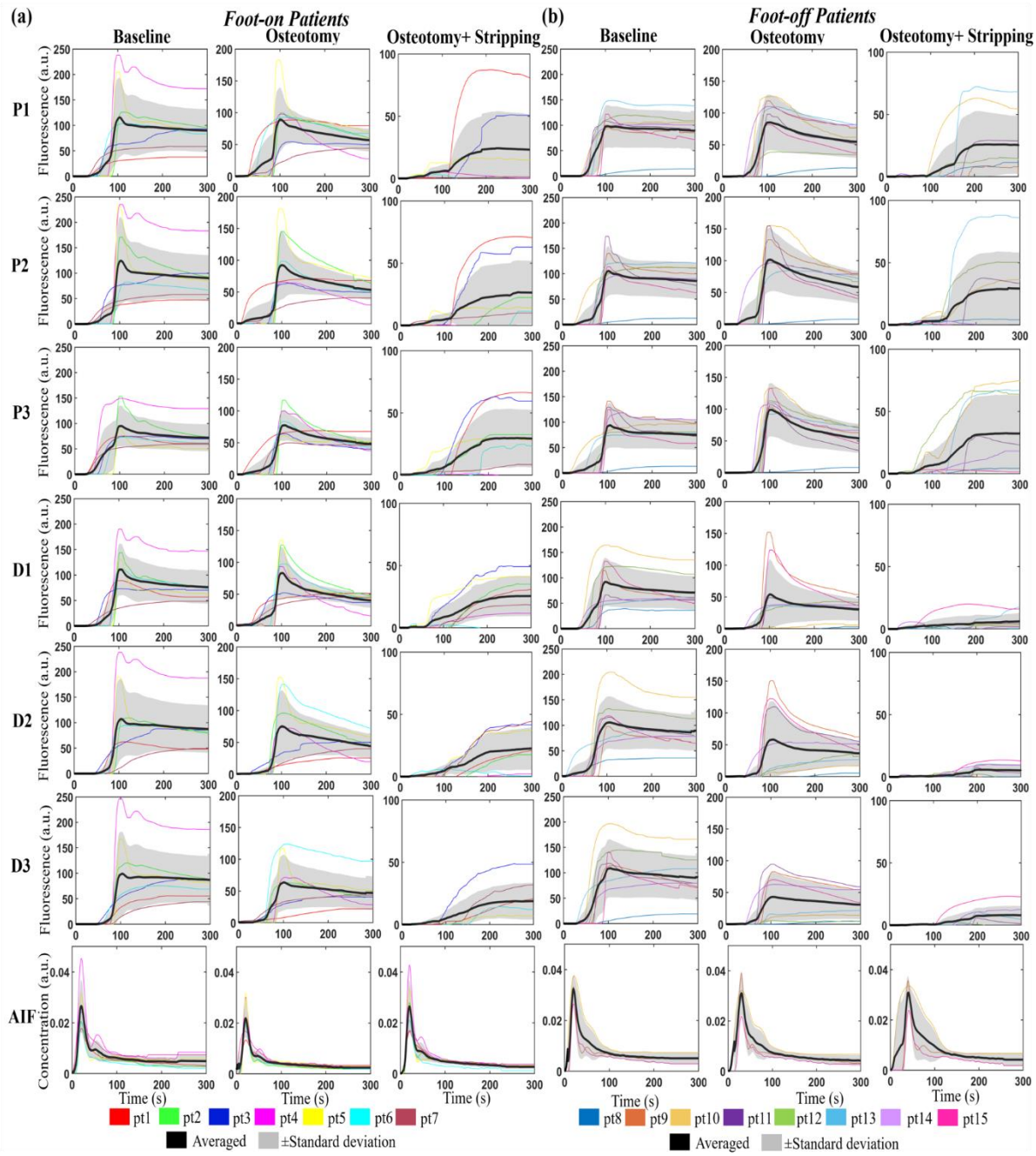

Figure 5.3: Bone fluorescence intensity temporal profiles and their arterial input functions. (a) Foot-on patients and (b) foot-off patients. Row 1~6: Fluorescence intensity temporal profiles of bone ROIs (P1~P3, D1~D3, respectively); Row7: Arterial input functions. Colored lines represent individual patients, black lines represent the averaged values over foot-on or foot-off patients, and gray shadows represent the standard deviation. Column 1-3: Baseline, Osteotomy, and Osteotomy + Stripping. P: Proximal, D: Distal, AIF: arterial input function, pt: patient.

5.3.2. AIF simple correction reduced the population variation

Arterial input function simple correction can efficiently eliminate the population variation. Comparing the distributions of *Imax* (**Figure 5.4 (a)**) and *IS* (**Figure 5.4 (b)**) before correction (in black) with after correction (in blue), the ranges in all three states have been reduced. The reduced standard deviations after correction (in 67% of dataset, **Table 5.2**) also showed that the population variation has decreased.

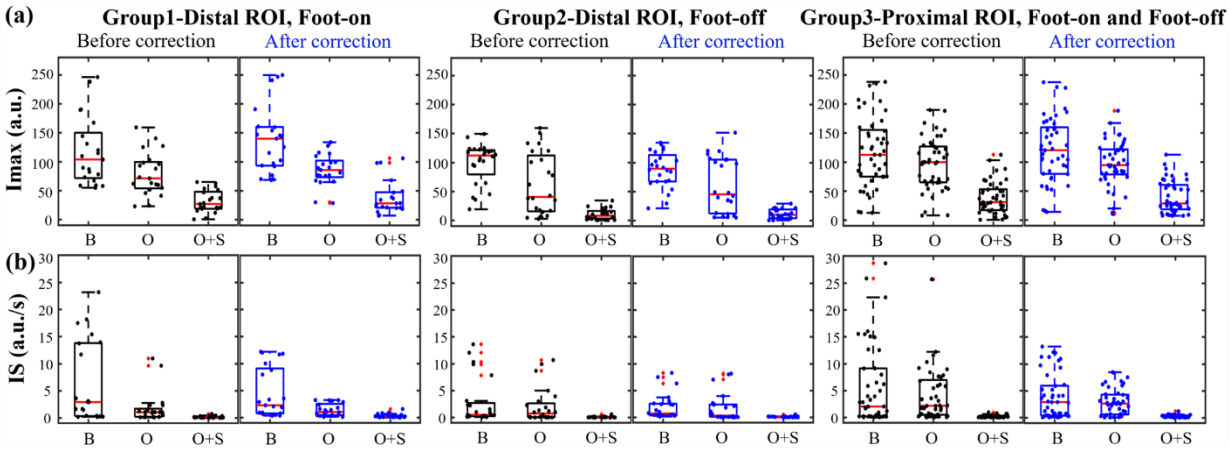

Figure 5.4: Distribution of first-pass parameters. (a) Imax and (b) IS. Column 1-3: Group 1-Distal ROI, Foot-on (n = 21), Group 2-Distal ROI, Foot-off (n = 24), Group 3-Proximal ROI, Foot-on and Foot-off (n = 45). Boxplots represent the min, first quartile, median, third quartile, and max of first-pass parameters in three perfusion states. Parameter values before AIF simple correction (black dots) are compared with those after AIF simple correction (blue dots). B: Baseline, O: Osteotomy, O+S: Osteotomy + Stripping.

5.3.3. Corrected first-pass kinetic parameters Imax_c and IS_c distributed differently with perfusion states, and they could classify bone perfusion according to healing potentials

From the baseline state to osteotomy and to osteotomy+ stripping state: *Imax_c* (**Figure 5.4(a)** in blue) and *IS_c* (**Figure 5.4(b)** in blue) were consistently decreasing in all groups, which reflected the importance of maximum capacity of blood volume and transit rate of ICG in blood vessel, respectively, in bone perfusion. Statistical tests showed that

TTP_c was not as significant as *Imax_c* and *IS_c* (**Table 5.2**), meaning that the transit time of ICG in blood vessel is not a determinant factor.

Table 5.2: Statistical analysis results after AIF correction. Mean, standard deviation and p-values of first-pass kinetic parameters in different groups, states and after simple correction. Group 1: Distal ROI, Foot-on (n = 21), Group 2: Distal ROI, Foot-off (n = 24), Group 3: Proximal ROI, Foot-on and Foot-off (n = 45). B: Baseline, O: Osteotomy, O + S: Osteotomy + Stripping. * Statistically significant.

Corrected First-pass parameters	Group #	B	O	O+S	p-value (B-O)	p-value (B-O+S)	p-value (O-O+S)
Imax_c	1	138±57	86±27	39±30	<0.01*	<0.01*	<0.01*
	2	98±31	61±47	11±8	<0.01*	<0.01*	<0.01*
	3	121±56	97±39	39±28	<0.01*	<0.01*	<0.01*
TTP_c	1	82±70	112±77	171±89	0.03*	<0.01*	0.04*
	2	106±76	112±85	103±83	0.57	0.90	0.66
	3	92±77	77±74	160±80	0.11	<0.01*	<0.01*
IS_c	1	4.6±4.6	1.4±1.1	0.3±0.4	<0.01*	<0.01*	<0.01*
	2	2.0±2.4	1.8±2.6	0.1±0.1	0.59	<0.01*	<0.01*
	3	4.0±4.2	2.9±2.4	0.3±0.2	0.04*	<0.01*	<0.01*

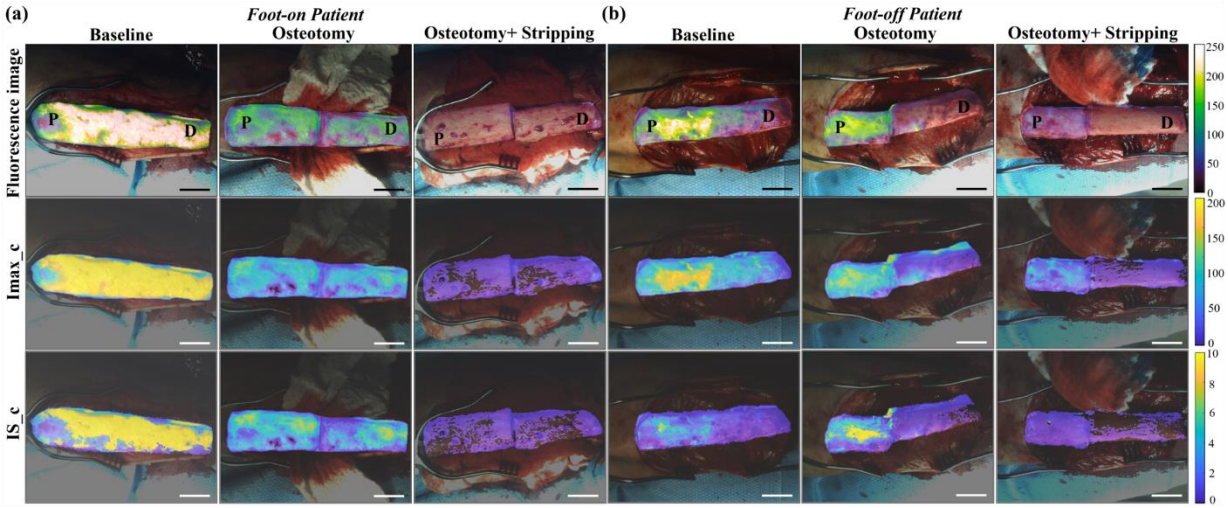

Figure 5.5: Overlaid fluorescence images and overlaid parametric maps of first-pass kinetic parameters after AIF correction. (a) A foot-on patient (pt4, a 52-year-old woman with right BKA) and (b) a foot-off patient (pt10, a 53-year-old woman with right BKA). Row 1: Overlaid fluorescence images at t = Tp with white light images; Row 2: Overlaid parametric maps of Imax_c with white light images; Row 3: Overlaid parametric maps of IS_c with white light images. Column 1-3: Baseline, Osteotomy, and Osteotomy + Stripping. Scale bars = 3cm.

Corrected *Imax_c* and *IS_c* in combination can classify bone perfusion states. The values of *Imax_c* and *IS_c* of baseline, osteotomy, and osteotomy + stripping bones are significantly different (**Figure 5.5**). Similarly, the values of *Imax_c* and *IS_c* of normal, minor injured, and major injured bones are also significantly different (**Figure 5.6(a, b)**). When using *Imax_c* and *IS_c* as machine learning predictors, the AUC is the highest (= 0.93) in Binary-class Classification 2 (**Figure 5.6(c)** and **Table 5.3**), which yields averaged metrics over 10-fold cross-validation as: accuracy of 0.81, sensitivity of 0.71 in *Normal/Minor injured* and sensitivity of 0.91 in *Major injured* (**Figure 5.7**). Due to the fact that normal, minor injured, and major injured bones are justified according to the increased blood supply damage levels, therefore first-pass kinetics can classify bone perfusion states.

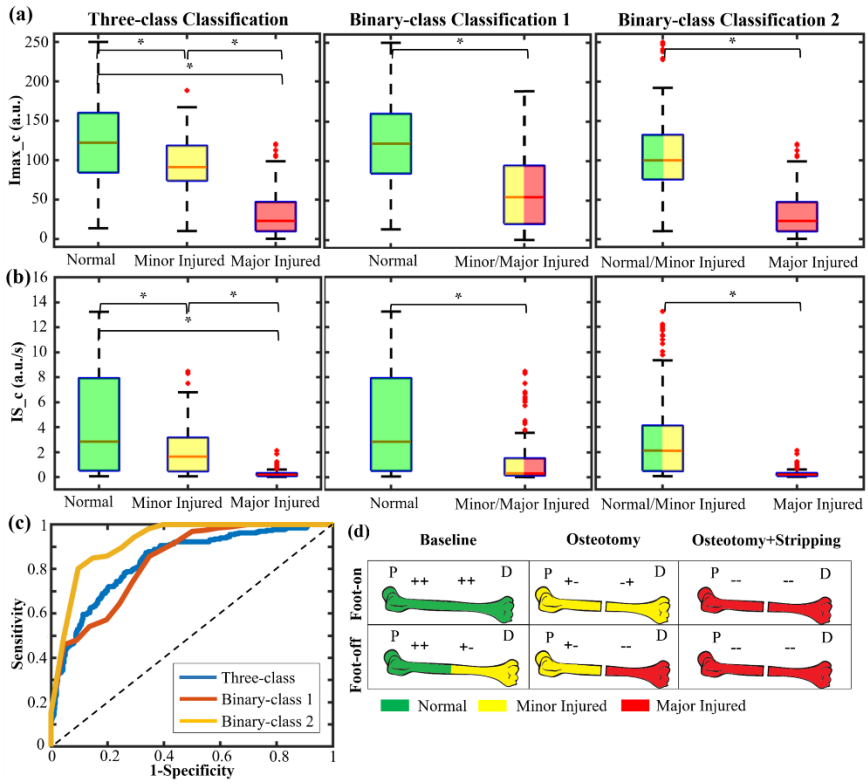

Figure 5.6: Corrected Imax_c and IS_c distribution in classified bone perfusion classes. (a-b) Corrected distribution of (a) Imax_c and (b) IS_c between classified bone perfusion classes of

different classification methods. Left: Three-class Classification, Center: Binary-class Classification 1, Right: Binary-class Classification 2. * P-values < 0.01. (c) ROC curves of three classifications. Black solid line = no method. Three-class classification used macro-averaged over classes. (d) Diagrams of labeling of bone regions-of-interest. From left to right: Baseline, Osteotomy, Osteotomy + Stripping. Top: Foot-on patient; Bottom: Foot-off patient. White line indicates the location of osteotomy. Green, yellow and red surface indicate the labels of Normal (++), Minor Injured (+-/-+) or Major Injured (--) blood supply, respectively. Left plus/minus sign: with/without arterial blood supply. Right plus/minus sign: with/without retrograde blood supply P: Proximal, D: Distal.

Table 5.3: Classification results from three classification approaches. Classification approaches include: Three-class classification (left), Binary-class classification 1 (center), and Binary-class classification 2 (right). Classification metrics include accuracy, sensitivity, specificity and AUC, which are all averaged over cross-validation rounds. Three-class classification used macro-averaged over classes for AUC calculation. Classifier is Gaussian Naïve Bayes.

	Three-class Classification			**Binary-class Classification 1**		**Binary-class Classification 2**	
Classes	**Normal**	**Minor Injured**	**Major Injured**	**Normal**	**Minor/Major Injured**	**Normal/Minor Injured**	**Major Injured**
Accuracy	0.65			0.74		0.81	
Sensitivity	0.35	0.54	0.92	0.60	0.88	0.71	0.91
Specificity	0.94	0.79	0.71	0.88	0.60	0.91	0.71
AUC	0.84			0.82		0.93	

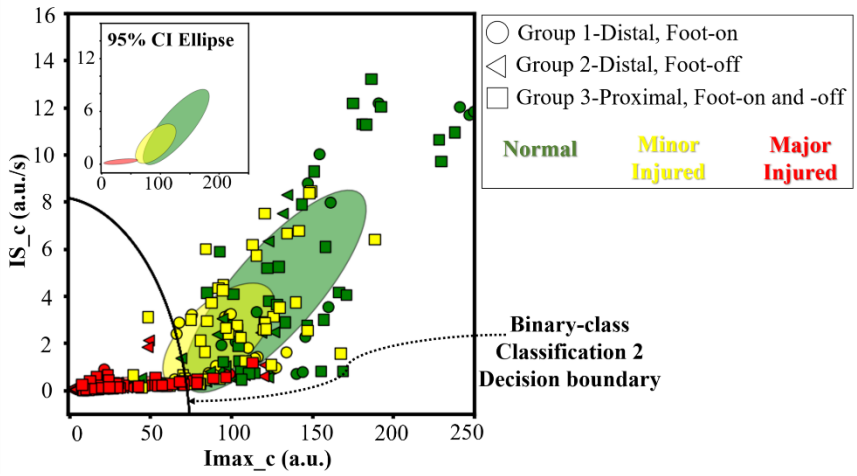

Figure 5.7: Binary-class Classification 2 results. Two-dimensional scatter plot of ROIs is plotted on axes of Imax_c and IS_c with decision boundary (solid black line). The shape of the marker indicates the group of the ROI: Circle = Group 1-Distal ROI, Foot-on patients, Triangle = Group 2-Distal ROI, Foot-off patients, Square = Group 3-Proximal ROI, Foot-on and Foot-off

patients. The color of the marker indicates the true perfusion state of the ROI: Green = Normal, Red = Injured. Background and top-left corner are the 95% confidence interval (CI) ellipses of each true perfusion state.

5.4. Discussion

Determining the location and degree of debridement is challenging in orthopaedic surgery. The most common way of making the determinations is by looking at the "clinical signs" [12]. However, this visual determination is subjective and highly dependent of surgeon's experience. To solve this problem, fluorescence-guided surgery (FGS), which has been utilized in multiple clinical applications such as tumor imaging [272–275], sentinel lymph node mapping [276–280], and nerve imaging [281,282], has been developed in orthopaedic surgery as well. FGS is able to visualize the spatial distribution of fluorescent dye, while DCE-FI, which adds temporal changes on FGS, can reflect quantitative information about perfusion. The most common investigation of DCE-FI is by explicit kinetic models, such as Tofts model [182] and AATH model [117,118]. However, most models are based on well-defined physiological assumptions that are difficult to achieve in real patient data. To alternate model-dependent methods, we have developed a model-independent quantitative analysis method based on first-pass kinetic parameters. DCE-FI has shown perfusion differences in both space and time. Specifically, AIF corrected first-pass kinetic parameters from DCE-FI, *Imax* and *IS*, could characterize and classify bone perfusion states, which demonstrated that first-pass kinetics can reflect the level of bone vasculature damage.

The proposed method has several advantages over others: It is assumption-free, robust, fast and easy in clinical translation: Firstly, no prior knowledge of the physiology nor precise assumptions are needed. This approach uses parameters that are shape-of-curve

associated and have been investigated in DCE-MRI and DCE-CT perfusion studies as semi-quantitative methods [283–286]. Secondly, this approach will remain robust in various patient physiological conditions, because it includes correction of inter-subject variations. Thirdly, the simple correction approach developed in this study is 50 times faster than the convolutional correction, while maintaining the same performance. Lastly, this approach is easy to be translated to clinics. The imaging system of this study is commercially available, and the analysis does not interfere with the imaging system and not cause reduced image quality or prolonged imaging time.

This study has some limitations that are worth mentioning. Firstly, the size of study is limited and convenience sampling is used, due to the natural difficulty in recruiting participants. Secondly, the quantitative analysis is sensitive to the quality of AIF measurement. Currently there is no commercially available intraoperative AIF device nationwide [128], and we used an early-stage in-house built AIF detector. Thirdly, noisy signals from surface blood or low-permeability tissues can reduce the accuracy of first-pass analysis. Lastly, the kinetic parameters selected in this study have not covered all possible ones. Other first-pass parameters such as AUC and egress slope are not included in this study. Future study will include recruiting more participants, improving the AIF detector, increasing signal-to-noise ratios in DCE-FI and including more kinetic parameters.

5.5. Conclusions

This is the first clinical study that investigated first-pass kinetic parameters from DCE-FI in differentiating bone perfusion states. AIF correction can further enhance the

analysis by reducing the between-patient variations. Maximum intensity and Ingress slope are decreased as bone perfusion is reduced, and can be used for perfusion classification according to bone's healing potentials.

In this chapter, first-pass kinetic analysis has been applied to clinical amputation models. It is demonstrated that the first-pass parameters, whether individually or in combination, can assess bone perfusion. Therefore, we have found first-pass parameters as one category of perfusion-associated features from DCE-FI. Parameters maximum intensity and ingress slope are the two most significant features correlated with perfusion. In addition, logistic regression model built on the two parameters has shown great probability as a debridement guidance tool. In the future, first-pass parameters will be combined with other perfusion-associated features to further improve the current fluorescence-guided surgery model.

Chapter 6

First In-human Use of Dynamic Contrast-Enhanced Texture Analysis for Orthopaedic Trauma Classification

This chapter has been adapted from the journal article published in 2022, entitled "Spatial and temporal patterns in dynamic-contrast enhanced intraoperative fluorescence imaging enable classification of bone perfusion in patients undergoing leg amputation" by Han X, Demidov V, Vaze VS, Jiang S, Gitajn IL, and Elliott JT in *Biomedical Optics Express* volume 13, issue 6. Jonathan T. Elliott supervised the project, made intellectual contributions, provided grant support and reviewed the manuscript. I. Leah Gitajn, Shudong Jiang, and Vikrant S. Vaze all provided intellectual inputs and assisted with the review of the manuscript. Valentin Demidov provided key intellectual contributions in methodology and assisted in manuscript writing. The author of this thesis was responsible for analyzing the data, writing programs and writing the manuscript. This chapter has met copyright permission requirements under Optica Publishing Group Open Access Publishing Agreement.

This chapter presents the first clinical study using texture analysis in dynamic contrast enhanced fluorescence imaging (DCE-FI) for orthopaedic trauma classification. Here a classification strategy for guiding proper surgical debridement according to bone perfusion levels has been developed. Bone perfusion levels have been classified by unsupervised machine learning based on spatiotemporal features extracted from DCE-FI images. The machine learning approach outperformed the standard method of using fluorescence intensity only to evaluate tissue perfusion by a two-fold increase in accuracy. The generalizability of the machine was evaluated in image series acquired in an additional

three patients, confirming the stability of the model and ability to sort future patient image-sets into viability categories. This chapter validated the performance of texture features in assessing bone perfusion, and opened up possibilities to use the spatiotemporal property in more complex clinical problems.

6.1. Introduction

Maintaining adequate bone and soft tissue perfusion is essential in orthopedic trauma surgery [14]. Poor bone and tissue perfusion promote bacterial biofilm formation and subsequent antibiotic treatment resistance [15,16]. Poorly perfused bone, also called devitalized bone, must be identified and debrided to remove bacterial biofilm, allow antibiotics and endogenous immune cells to enter, treat atrophic nonunion [10,11]. Currently, determinations regarding the extent of debridement relies mainly on the surgeon's visual inspection. Visual clues include stripped soft tissue, darkness and color of bone, presence of multiple drill holes and lack of "paprika" sign [12]. This subjective assessment places surgeons at a risk of debriding too much or too little tissue; at the present, there are many "gray regions" that do not fit nicely into the "black-or-white" clinical decision around sparing tissue or removing it [13].

To inform and improve treatment methods, bone vascularization and necrosis can be assessed using imaging. While other modalities have been traditionally used for imaging tissue perfusion [287–289], dynamic contrast-enhanced (DCE) imaging based on optical fluorescence (either visible or infrared emission) is becoming increasingly popular in other clinical applications such as tumor detection [85], vasculature evaluation [86] and perfusion assessment [89]. Furthermore, it is well suited to novel application in orthopaedic surgical guidance because of challenges obtaining sufficient contrast-to-background in computed tomography (CT) and magnetic resonance imaging (MRI) of bone. The DCE-FI method proposed in this paper uses near-infrared (NIR) fluorescent light (700-900 nm), that has good penetration through blood and tissue. Compared to other imaging modalities, DCE-FI does not use ionizing radiation and updates in real-time, making it a safe and

versatile imaging technique for continuous intraoperative use. Furthermore, additional contrast based on tissue perfusion is obtained by deconvolving the concentration of contrast agent over time in tissue with an arterial input function that is measured from a finger detector. Compared to pure intensity-based methods, DCE-FI can not only provide qualitative information that can be captured by human eyes, but also provide quantitative information such as blood flow and blood volume. Indocyanine green (ICG) contrast agent-based DCE-FI techniques on bone perfusion have been developed by several preclinical studies [19,21,97,261–263]. Among these, maximum fluorescence intensity (FI) at the peak intensity time is the most commonly used parameter [97,261,262], but it cannot always significantly differentiate bone perfusion [97,263]. From our previous *in vivo* animal studies [19,21], kinetic parameters such as total bone perfusion and late perfusion fraction have been proved to be capable of quantitatively evaluating bone perfusion changes. However, those parameters of DCE-FI have not been evaluated in human clinical applications.

In this study, we explore the capability of DCE-FI to predict bone perfusion in patients undergoing surgery. The surgical procedure is amputation of the leg; however, the study allows for intermediary steps before amputation (transverse osteotomy and periosteal stripping) to create artificial conditions representing fracture and degloving injury. In addition to acquiring the first DCE-FI dataset on 12 patients each with 3 conditions (total 36 image series), this paper develops a classification strategy to predict whether a particular region is damaged or not. Specifically, we propose a fast unsupervised machine learning approach to predict the perfusion or viability level of any bone region-of-interest (ROI) based on spatiotemporal features. This was accomplished by obtaining the 36 series of

fluorescence images from patients undergoing limb amputation surgery and manipulation; 2.5×10^6 segmented ROIs at bone region were included to train the model; 1×10^6 ROIs were used for testing the model using a cross-validation approach where output labels were compared to model predictions and to a benchmark fluorescence intensity thresholding-based label.

The reported unsupervised classification approach, using a combination of extracted spatial features—which have been utilized in multiple image classification studies microscopically [290] and macroscopically [291,292]—and temporal features from DCE-FI fluorescence images, demonstrated the ability to reliably stratify ROIs into three perfusion levels: "appearing normal", "appearing suspicious" (further attention warranted) and "appearing compromised" (debridement recommended to completely remove the devitalized bone), and produce outlines that are comparable to segmentation boundaries performed by an experienced surgeon. The classification is fast (accelerated by including principal component analysis for dimension reduction), robust and straight-forward (simple to train because *k*-means clustering classification is used which need fewer data and no input labels), and can be applied with commercially available intraoperative imaging systems without any additional hardware. This first translational bone perfusion classification approach, applied to a highly unique patient dataset, can be readily deployed in other centers and has significant clinical potential not only in lower-limb amputation but in a wide variety of orthopaedic trauma settings.

6.2. Methods and Materials

6.2.1. Patient Study

The patient study was approved by the Institutional Review Board of the Dartmouth-Hitchcock Medical Center and listed on ClinicalTrials.gov as NCT04250558. Informed consent was obtained from twelve participants with confirmed below knee amputation (BKA) and/or their legal guardians. Imaging occurred between January 2020 and March 2022. Information about these participants is listed in **Table 6.1**. In six subjects (50%), the foot distal to the site of amputation was removed prior to imaging. All methods were performed in accordance with the relevant guidelines and regulations. Before the definitive lower leg osteotomy, the limb to be amputated was manipulated to create three conditions, designed to mimic low energy and high energy fracture, and time series of fluorescence images were acquired in each condition: (1) *baseline*; (2) *osteotomy (*bone cut 15cm from the medial malleolus to disrupt endosteal blood flow, similar to a simple low energy fracture); (3) *osteotomy and debridement* (extensive soft tissue stripping proximal and distal to the osteotomy to disrupt both endosteal and periosteal blood flow, similar to a higher energy fracture). These manipulations did not add appreciably to the duration of surgery.

Table 6.1: Patient information. BKA – below knee amputation. Patients 1-9 were used for machine cross-validation, and Patients 10*-12* were used to evaluate generalizability

Patient ID	Age	Gender	Pre-operation diagnosis	Foot removed prior to imaging
1	53	Male	Amputation: left BKA	No
2	62	Male	Amputation: right BKA	Yes
3	66	Male	Amputation: left BKA	Yes
4	40	Male	Amputation: right BKA	No
5	33	Female	Amputation: left BKA	No
6	51	Male	Amputation: right BKA	No
7	53	Female	Amputation: right BKA	Yes
8	73	Male	Amputation: right BKA	Yes
9	51	Male	Amputation: right BKA	Yes
10*	27	Male	Amputation: right BKA	Yes
11*	62	Male	Amputation: right BKA	No
12*	52	Female	Amputation: right BKA	No

6.2.2. Image acquisition by DCE-FI

For 20 seconds before and for 4 minutes after 0.1 mg/kg intravenous injection of ICG, fluorescence images of surgical areas were recorded using SPY Elite imaging system (Stryker Corp., Kalamazoo, MI, USA) equipped with 805 ± 10 nm laser diode for ICG excitation and NIR charge-coupled device camera with pre-installed 820-900 nm band pass filter (**Figure 6.1(a)**) for fluorescence detection (**Figure 6.1(b)**). The working distance was approximately 300 mm, and light intensity and integration times were kept constant. Additional white light camera connected through the beam splitter was used to capture white light photographs (**Figure 6.1(c)**). Image sequences recorded in DICOM format had the following specifications: 1024 frames; frame size – 1024 × 768; frame rate – 4.25 frames per second; image depth – 8 bits per pixel; field of view – 19 × 14 cm^2; lateral resolution – 223 µm.

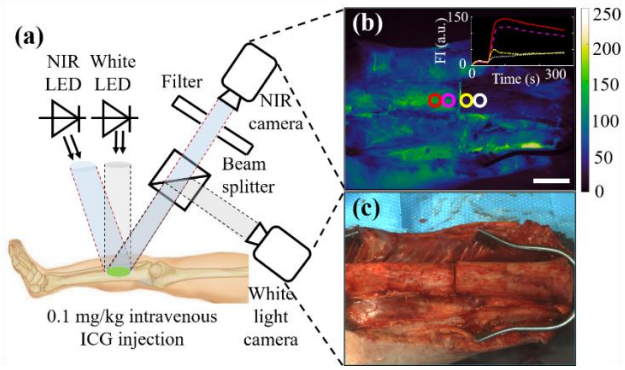

Figure 6.1: Dynamic contrast-enhanced fluorescence imaging. (a) Imaging setup. (b) NIR image from NIR camera on the tibia bone after osteotomy at the peak time of fluorescence intensity. Scale bars are 3 cm. Top right corner are ICG kinetic curves in the four regions of interest shown in (b) - proximal ROI1 (red curve), proximal ROI2 (magenta dashed curve), distal ROI3 (yellow dash-dotted curve), and distal ROI4 (white dotted curve). (c) White light image from white light camera on the same bone shown in (b).

6.2.3. Training and validating the spatiotemporal classification machine with an unsupervised learning approach

After acquisition, images were transferred to a local computer and processed using the MATLAB (The MathWorks, Natwick, MA) software. The proposed bone perfusion classification method is based on spatiotemporal feature extraction and unsupervised machine learning, shown schematically step-by-step in **Figure 6.2**.

*Image normalization and ROI selection (step **1** in **Figure 6.2**):* Images were first normalized and then ROIs were selected. For this, raw fluorescence images (step **1** in **Figure 6.2**, **left**) associated with each ICG injection were converted to relative changes in fluorescence (step **1** in **Figure 6.2**, **right**) by subtracting the median fluorescence in the initial 10 seconds of image recording. Images selected for training are all frames from global peak intensity time to 120 seconds after (step **1** in **Figure 6.2**, **top**). After that, the relevant part of the image corresponding to the tibia bone (**red dashed rectangle** in step **1** in **Figure 6.2**, **right**) was selected and split into approximately 320-400 ROIs (depending on the bone size) of 20 × 20 pixels (**black squares** in step **1** in **Figure 6.2**, **right**, side = 4.5 mm). The size of ROIs was determined to achieve an optimal balance between the high classification performance and the low computational time. Each ROI represented one data point in the subsequent analysis, and total number of data points in training dataset is 2.5×10^6.

*Feature extraction (step **2** in **Figure 6.2**):* After data preprocessing, 21 first and second order spatiotemporal features (f1~f21) summarized in **Appendix B, Table B.1** were extracted from each ROI. They included six intensity-based features, thirteen gray-level co-occurrence matrix (GLCM)-based features and two Gamma distribution parameters. First-order image intensity features were important to consider because of their dependence on distribution of pixel intensities within regions of interest and reflection of local intensity

changes. GLCM features provided information on different scale of interest, describing how joint probability of paired gray levels of neighboring pixels was distributed along specific image directions [209]. Gamma distribution fitting parameters were considered among other features because of their excellent sensitivity to local changes in optical properties of imaged tissues [293–295], such as tissue effective scatterer number density and size [296,297]. Detailed parameters in computing each feature were stated in **Appendix B**.

*Principle component analysis (step **3** in **Figure 6.2**):* Features extracted from each fluorescence image in series for three conditions of all training patients created a large dataset, which would require long computational time. In order to reduce the number of variables while preserving most of the information, we used principle component analysis (PCA). PCA reduced the high number of predictor variables by linearly transforming them into fewer principle components (PC), at the same time preserving the information (*i.e.*, data variance) provided by the features without significant loss, while consolidating redundant information across variables into a more manageable number of features [235,298]. Top principle components with cumulative percentage of explained variance larger than 85% were retained, yielding three PCs (PC1~PC3), in order to prioritize computational speed while still maintaining sufficient proportion of data variance. Linear transformation coefficients (*i.e.*, PC coefficients) of each feature-PC pair were recorded and plotted on axes of three PCs (step **3** in **Figure 6.2**). The values in three PCs (PC scores) of each ROI were defined as a new $n \times 3$ data matrix $\boldsymbol{Y}$ for the next step of machine learning classification.

*K-means clustering (step **4** in **Figure 6.2**):* *K*-means clustering algorithm was applied to the data ***Y*** to separate it into three clusters to obtain a reasonable and clinically meaningful level of stratification in bone status (*normal, suspicious,* and *compromised*). Each PC was weighted by its importance (*i.e.*, square root of variance explained) for scaling the axes. Every data point from the testing set was allocated to the one cluster which corresponds to shortest Euclidean distance from the cluster centroid (**black crosses** in step **4** in **Figure 6.2**) to that data point. Each PC value of the centroid was defined by taking the average values on the corresponding PC values over the data points within the cluster. Then algorithmically generated labels were generated as: Among three clusters, by comparing the ranges of feature values and referring to their physical interpretations, the relationship between clusters (*Cluster 1*, *Cluster 2* and *Cluster 3*) and perfusion levels (*normal*, *suspicious* and *compromised*) was established.

*Feature statistical significance evaluation and ranking (step **5** in **Figure 6.2**):* After all ROIs were partitioned into three clusters, each feature's input into each cluster was analyzed statistically using the one-way three-group ANOVA test. Features with P-value < 0.05 were considered statistically significant and selected. Features were then ranked based on the absolute values of their respective PC coefficients for the first principal component (denoted by $PC1_{coeff}$): Features with absolute $PC1_{coeff} > 0.3$ were considered to have high rank, with absolute $0.1 < PC1_{coeff} < 0.3$ were considered as middle ranks, and those with absolute $PC1_{coeff} < 0.1$ were considered low rank. Significantly contributing features (features contributing most significantly to the components) were also selected by their respective PC coefficients for the three PCs (absolute $PC1_{coeff}$ or $PC2_{coeff}$ or $PC3_{coeff} > 0.1$).

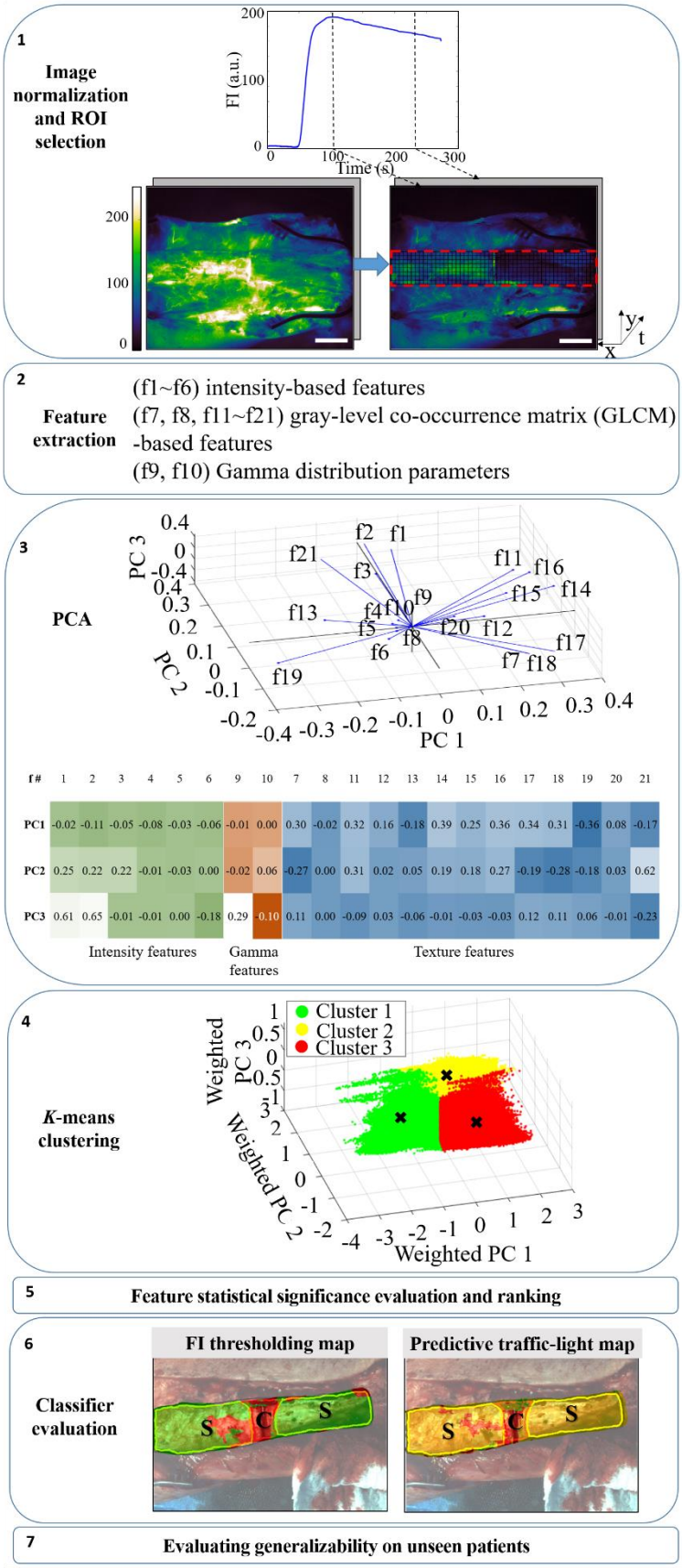
1
Image normalization and ROI selection
FI (a.u.)
Time (s)
2
Feature extraction
(f1~f6) intensity-based features
(f7, f8, f11~f21) gray-level co-occurrence matrix (GLCM) -based features
(f9, f10) Gamma distribution parameters
3
PCA
PC 1
PC 2
PC 3
f# 1 2 3 4 5 6 9 10 7 8 11 12 13 14 15 16 17 18 19 20 21
PC1 -0.02 -0.11 -0.05 -0.08 -0.03 -0.06 -0.01 0.00 0.30 -0.02 0.32 0.16 -0.18 0.39 0.25 0.36 0.34 0.31 -0.36 0.08 -0.17
PC2 0.25 0.22 0.22 -0.01 -0.03 0.00 -0.02 0.06 -0.27 0.00 0.31 0.02 0.05 0.19 0.18 0.27 -0.19 -0.28 -0.18 0.03 0.62
PC3 0.61 0.65 -0.01 -0.01 0.00 -0.18 0.29 -0.10 0.11 0.00 -0.09 0.03 -0.06 -0.01 -0.03 -0.03 0.12 0.11 0.06 -0.01 -0.23
Intensity features
Gamma features
Texture features
4
K-means clustering
Cluster 1
Cluster 2
Cluster 3
Weighted PC 1
Weighted PC 2
Weighted PC 3
5
Feature statistical significance evaluation and ranking
6
Classifier evaluation
FI thresholding map
Predictive traffic-light map
S
C
S
7
Evaluating generalizability on unseen patients

Figure 6.2: Workflow of bone perfusion classification. Step **1**: Image normalization and ROI selection. **Left**: Representative raw image at peak fluorescence time from patient No.3 under osteotomy conditions. **Top**: Images selected for training are all frames from global peak intensity time to 120 seconds after. **Right**: Normalized fluorescence image from the same patient. In order to compensate for possible residual fluorescent signal from previous injections, median fluorescence of the first 10 seconds were subtracted from all images. The region of the tibia bone (**red dashed rectangle**) was split into 20 × 20-pixel ROIs (**black squares**). Scale bars are 3 cm. Step **2**: Feature extraction. Twenty-one extracted features were listed. Step **3**: PCA. PC coefficients of 21 texture features (f1 to f21) were plotted. Bottom is color-coded table of PC coefficients showing three categories of features separately. Step **4**: *K*-means clustering. *K*-means clustering partition training data points into three clusters. Each data point (**green, yellow** or **red dot**) represents the corresponding PC scores, weighted by the square root of total variance PCs explained and assigned to a given cluster closest to the corresponding centroid (**black crosses**). Step **5**: Feature statistical significance evaluation and ranking. Step **6**: Classifier evaluation. Predictive traffic-light map by *k*-means classifier (**right**) were compared with FI thresholding map (**left**). *Normal*-**green**, *Suspicious*-**yellow**, *Compromised*-**red**. Labels are ground truth by surgeon's delineation of bone perfusion status. **N**-*normal*, **S**-*suspicious*, **C**-*compromised*. Step **7**: Evaluating the generalizability of the method on unseen patients (Patients 10-12).

*Classifier evaluation using leave p out cross validation (step **6** in **Figure 6.2**)*: In order to evaluate the performance of the *k*-means classifier, the resulting predictive maps produced on testing data (step **6** in **Figure 6.2, right**) were compared to benchmark classification method (step **6** in **Figure 6.2, left**). The 'ground truth' labels were defined by an experienced orthopedic surgeon according to clinical signs. In this case, the leave-p-out cross-validation (p = 2 and n = 9) was used in order to keep the training data and testing data separate from different patients in each iteration. The machine performance across all patients—and representing 3.5 million ROIs— was evaluated in 36 validation rounds so that all possible combinations of training (n = 7) and testing (n = 2) data were covered: First, 3 × 3 confusion matrices (**Figure 6.3(a)**) from two classifiers were computed by comparison to ROI labels from ground truth map. Then, classification performance was evaluated by comparison of a pre-determined set of metrics (**Figure 6.3(b)**) including four penalty terms, computed from the confusion matrices: (i) accuracy, (ii) sensitivity, (iii) specificity, and (iv) cost functions consisted of F1-scores and surgeon's burden (SB). Each

of them reflects one type of clinical cost, respectively: (i) overall error rate, (ii) the penalty associated with inappropriate tissue sparing leading to potential infection, (iii) unnecessary tissue removal resulting in larger deficit and increased recovery time, and (iv) F1-scores: harmonic means of detection precision and sensitivity; SB: inappropriately assigning pixels to 'suspicious' when they are 'normal' and 'compromised', resulting in a greater-than-needed burden to the surgeon's attention.

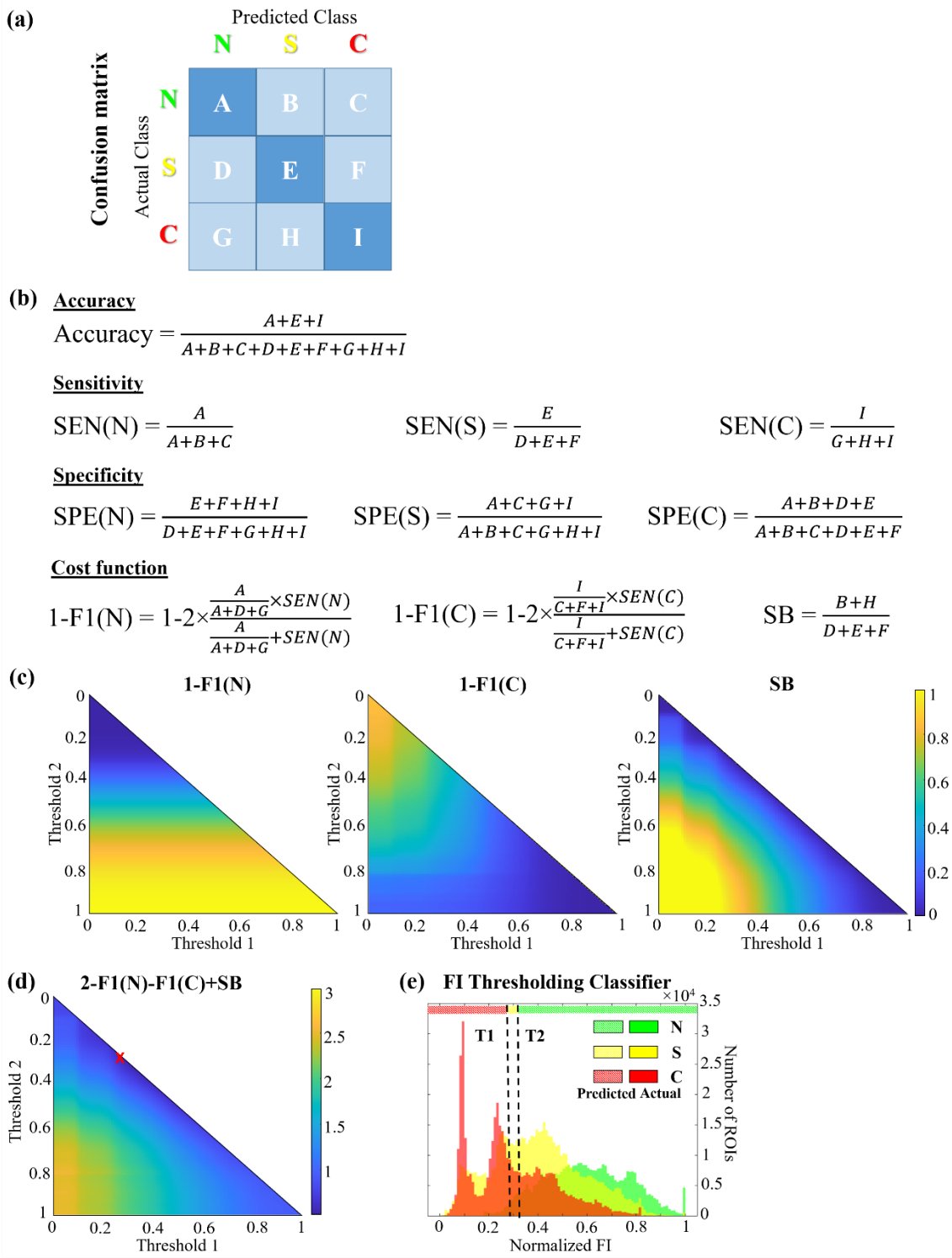

Figure 6.3: Classification metrics and benchmark classification method. (a) Confusion matrix for classifier evaluation and testing. N-normal, S-suspicious, C-compromised; (b) Pre-determined metrics. SEN(N)-sensitivity to normal class, SEN(S)-sensitivity to suspicious class, SEN(C)-sensitivity to compromised class, SPE(N)-specificity to normal class, SPE(S)-specificity to suspicious class, SPE(C)-specificity to compromised class, F1(N)-F1 score for normal class,

F1(C)-F1 score for compromised class, SB-Surgeon's burden that examines the ratio of incorrectly predicted as suspicious class over the actual suspicious class; (c) Results of three cost functions from all the combinations of two thresholds. **Top left**: 1 - F1(N), **Top right**: 1 - F1(C), **Bottom right**: SB. (d) Results of total cost functions (2 - F1(N) - F1(C) + SB) from all combinations of two thresholds. The optimal threshold combination that yields lowest total value was found to be T1 = 0.29, T2 = 0.32, indicated by the red ***X***; (e) FI thresholding classifier. Histogram of normalized FI from three bone perfusion levels of training set is showed with optimal thresholds indicated by black dashed lines. Predicted classes and actual classes are indicated by diagonal faces and solid faces, respectively.

The benchmark classification method used fluorescence intensity thresholds applied to images of fluorescence intensity acquired at the peak intensity—the typical approach used in fluorescence guided surgery. Two FI thresholds approach were established, to enable classification into three categories as in the machine learning (ML) approach (normal, suspicious, and compromised). It was accomplished by firstly normalizing FI of ROIs into [0,1] within each patient, and then searching the optimal FI threshold combination (0 < T1 < T2 < 1) that yielded lowest total cost function (2 - F1(N) - F1(C) + SB, **Figure 6.3(d)**). The cost functions were selected to ensure equally high F1-scores to normal and compromised class as well as low surgeon's burden (**Figure 6.3(c)**). From all possibilities, the optimal threshold combination was: T1 = 0.29 and T2 = 0.32 (indicated by red ***X*** in **Figure 6.3(d)**). As a result, the FI thresholding classifier (**Figure 6.3(e)**) worked by: Range 0 < FI < 0.29 was predicted as *compromised*, 0.29 < FI < 0.32 - as *suspicious*, and 0.32 < FI < 1 - as *normal*.

*Evaluating the generalizability of the classification method on unseen patients (step **7 in Figure 6.2**)*: Finally, a final evaluation round including three additional unseen patients' data was conducted (**Figure 6.4**), using the classification parameters (*i.e.,* PC coefficients and centroid coordinates) averaged from the top 10% of the cross-validation rounds. In this way, the generalization ability of the proposed classifier can be evaluated.

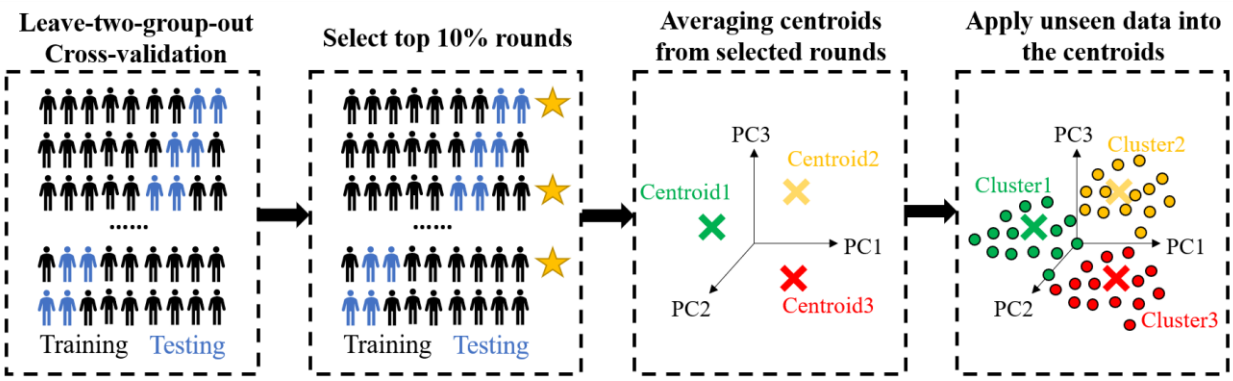

Figure 6.4: Flowchart of testing model generalizability. Step 1: Loop through all 36 possible training/testing combinations of leave-two-group-our cross-validation. Step 2: Select the top 10% rounds. Step 3: Take the average PC coefficients and centroids of selected rounds. Step 4: Apply the three unseen patients' data into the average PC coefficients and centroids.

6.3. Results

6.3.1. Extracted spatiotemporal features provide additional information beyond fluorescence intensity alone

Fifteen out of total 21 significantly contributing features are shown in the **Figure 6.5,** which was acquired during a bone osteotomy condition (**Figure 6.5(a)).** They represent image properties not visible to the naked eye from conventional fluorescence images, such as homogeneity, uniformity, linearity, coarseness and dependency, based on the spatial distribution and statistics of pixel intensities [209,299]. These properties are influenced by the dynamic behavior of fluorescence, which distributes both spatially and temporally according to underlying perfusion characteristics.

In the case of normal perfusion (green box in **Figure 6.5(b)**), where the vasculature is intact and blood flow is efficient, fluorescence intensities are spatially distributed more evenly and consistently. Therefore features describing similarities (f1~3, f11, f14~16, f21 in **Figure 6.5(b)**) have high values in normal perfusion regions. In contrast, tissue with compromised perfusion (red box in **Figure 6.5(b)**), having damaged vasculature and

disrupted blood flow, exhibits a markedly different distribution of fluorescence intensity which is lower in value and temporally delayed and disorganized. So features describing differences (f7, f12, f17~19 in **Figure 6.5(b)**) have high values in compromised regions. In summary, extracted spatiotemporal features allow for quantification of these differences, containing more information than fluorescence images alone.

6.3.2. K-means classification is fast and reproducible, resulting in boundaries that are physiologically meaningful

Principle component analysis resulted in a 56% reduction in computational time, by the way of reducing the dataset size by 7-fold while keeping 88.2% of the data information, compared to scenario without PCA. Considering each PC as a linear transformation of extracted features, before linear transformation (**Figure 6.6(b)**), 21 spatiotemporal features display patterns that can differentiate the three clusters, where features with higher ranking show clearer patterns. While after linear transformation (**Figure 6.6(a)**), 3 PCs display patterns that can partition the three clusters as well. The first three PCs (total variance explained: 46.1%, 32.9%, 9.2%, respectively, **Figure 6.6(a), bottom**) represented most of the information of the training dataset. Therefore, using 3 PCs instead of 21 spatiotemporal features as classification predictors can significantly speed up the method, while meantime reserve most of the data information. As a result, k-means classification predictions can be provided to the surgeon in less than 5 minutes (1~2 min to global peak intensity plus 2~3 min image processing and classification).

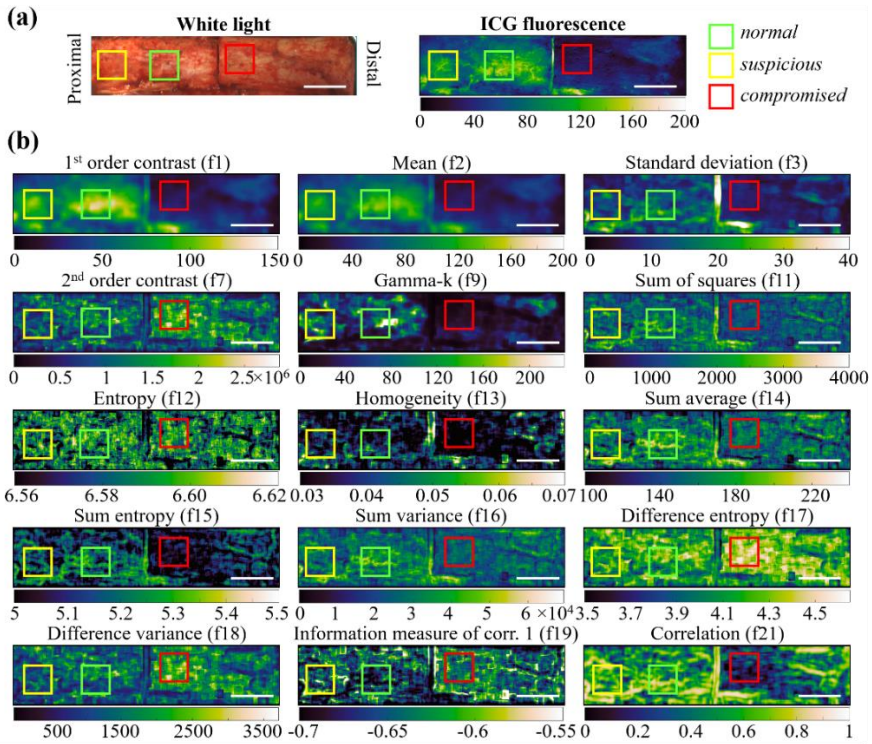

Figure 6.5: Feature parametric maps. Colored boxes are regions with labels from ground truth map: Green box-*normal*, yellow box-*suspicious*, red box-*compromised*. (a) White light (left) and ICG fluorescence (right) images of bone in the osteotomy condition. Right site of the bone is proximal and left is distal. (b) Color-scaled parametric maps of 15 significantly contributing features, extracted from the ICG fluorescence image shown in (a). Scale bars are 3 cm.

By *K*-means clustering, all training dataset ROIs (represented by weighted PC scores) were partitioned into three clusters, each assigned to the closest centroid. This classification method is simple because no input labels are required, while each cluster can be straightforwardly explained as corresponding to perfusion level by referring to its PC scores and feature ranges: *Cluster 1* (green in **Figure 6.6**, left column) has the lowest PC1 scores (**Figure 6.6(a)**) thus having the lowest average values of high-ranked features (**(Figure 6.6(b)**, left bracket); *Cluster 2* (yellow in **Figure 6.6**, left column) has the highest PC2 scores (**Figure 6.6(a)**) and, hence, the highest average values in middle-ranked features (**Figure 6.6(b)**, middle bracket); *Cluster 3* (red in **Figure 6.6**, left column)

comprises high PC1 scores and low PC2 scores (**Figure 6.6(a)**), thus having lowest average values in low-ranked features (**Figure 6.6(b)**, right bracket). High-ranked features are mostly related to spatial variation, middle-ranked features to spatial uniformity, and low-ranked features are a mix of both variation and uniformity. As normally perfused bones have low spatial variation and bones with compromised perfusion have low spatial uniformity, the clusters were tagged with perfusion levels as followed: *Cluster 1* represents *normal perfusion, Cluster 2 - suspicious perfusion,* and *Cluster 3 - compromised perfusion*.

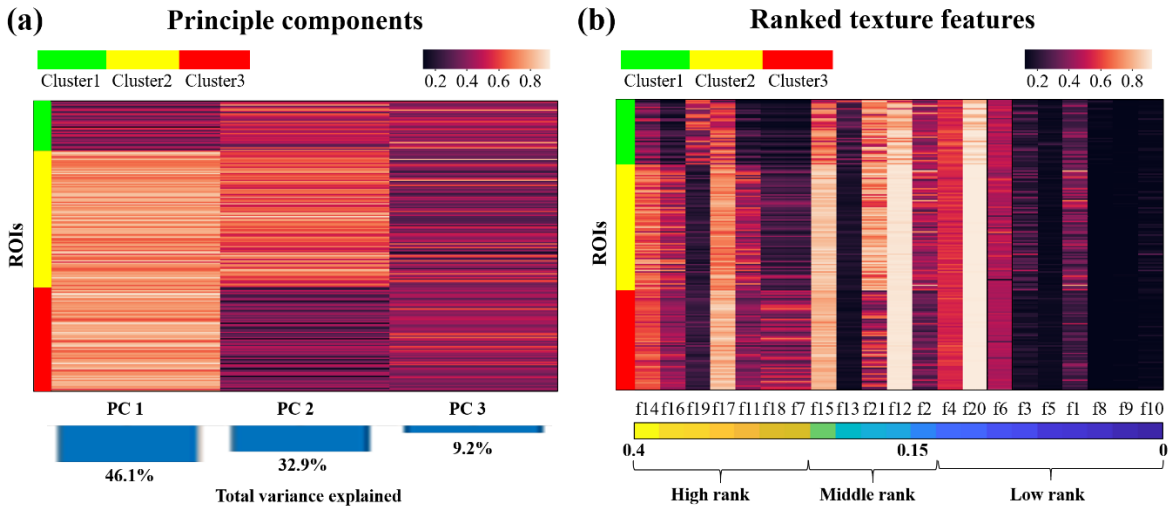

Figure 6.6: Heatmap of principle components and ranked features. (a) Heat map of the first three principle components (PC1-PC3) rescaled to [0,1] range and partitioned into three clusters (labeled with green, yellow and red on the left). PC values of each data point are represented by its weighted scores on PC axes. The percentage of total variance explained by each PC is shown in the bar graph at the bottom. (b) Heat map of extracted texture features rescaled to [0,1] range and arranged in the descending ranking order in reference to the absolute value of $PC1_{coeff}$ (see color bar at the bottom). Three clusters visualize feature patterns, being most prominent at the higher-ranked region and hardly distinguishable at the lower-ranked region.

6.3.3. Spatiotemporal k-means classification outperformed the fluorescence intensity-only benchmark

At every cross-validation round, *K*-means clustering-based bone perfusion classification was tested on ROIs from two patients completely unseen in the training

cohort. **Figure 6.7(a)** showed an example testing round of round 1, where the classifier was trained by ROIs from patient 1~7, and tested by ROIs from the *baseline* and *osteotomy* cases of patients 8 and 9 (**Figure 6.7(a)**, column 1). The resulted four perfusion classification maps (**Figure 6.7(a)**, column 4) were compared to three-level FI-thresholding classification maps (**Figure 6.7(a)**, column 3), with ground truth maps (**Figure 6.7(a)**, column 2) to be three-level clinical signs-based delineations by an experienced orthopaedic surgeon. FI thresholding classifier appears to be extremely sensitive to fluorescence intensity variations caused by systematic and environmental settings, thus prone to visually distinguishable errors (compared to ground truth) in bone perfusion classification. In contrast, *K*-means clustering classifier predicts bone perfusion levels more accurately, regardless of fluorescence intensity variations.

Quantitative comparison using pre-determined set of metrics (**Figure 6.3(b)**) further demonstrates differences in performance. **Figure 6.7(b)** compared these metrics, averaged over all cross-validation rounds (all results from two classifiers were statistically different): *K*-means clustering consistently reported high overall accuracy (0.72 ± 0.10), high sensitivity of all classes (normal = 0.88 ± 0.15, suspicious = 0.63 ± 0.22, compromised = 0.62 ± 0.22), high specificity of two classes (normal = 0.88 ± 0.08, compromised = 0.87 ± 0.09), and high F1-scores (normal = 0.82 ± 0.14, compromised = 0.55 ± 0.17); In comparison, the FI thresholding classifier had lower overall accuracy (0.37 ± 0.07), lower sensitivity of all classes (normal = 0.74 ± 0.18, suspicious = 0.09 ± 0.06, compromised = 0.44 ± 0.12), lower specificity of two classes (normal = 0.44 ± 0.19, compromised = 0.73 ± 0.16), and lower F1-scores (normal = 0.53 ± 0.08, compromised = 0.32 ± 0.09). Despite the fact that *K*-means clustering demonstrated slightly lower metrics than FI thresholding

classifier in specificity to suspicious pixels (*k*-means = 0.81 ± 0.12 VS FI = 0.90 ± 0.05) and surgeon's burden (*k*-means = 1 - 0.82 ± 0.10 VS FI = 1 - 0.88 ± 0.07), *K*-means had overall much superior performance because its generality and its absence of bias, which is very important clinically. On the other hand, FI thresholding classifier exhibited high bias against the suspicious class.

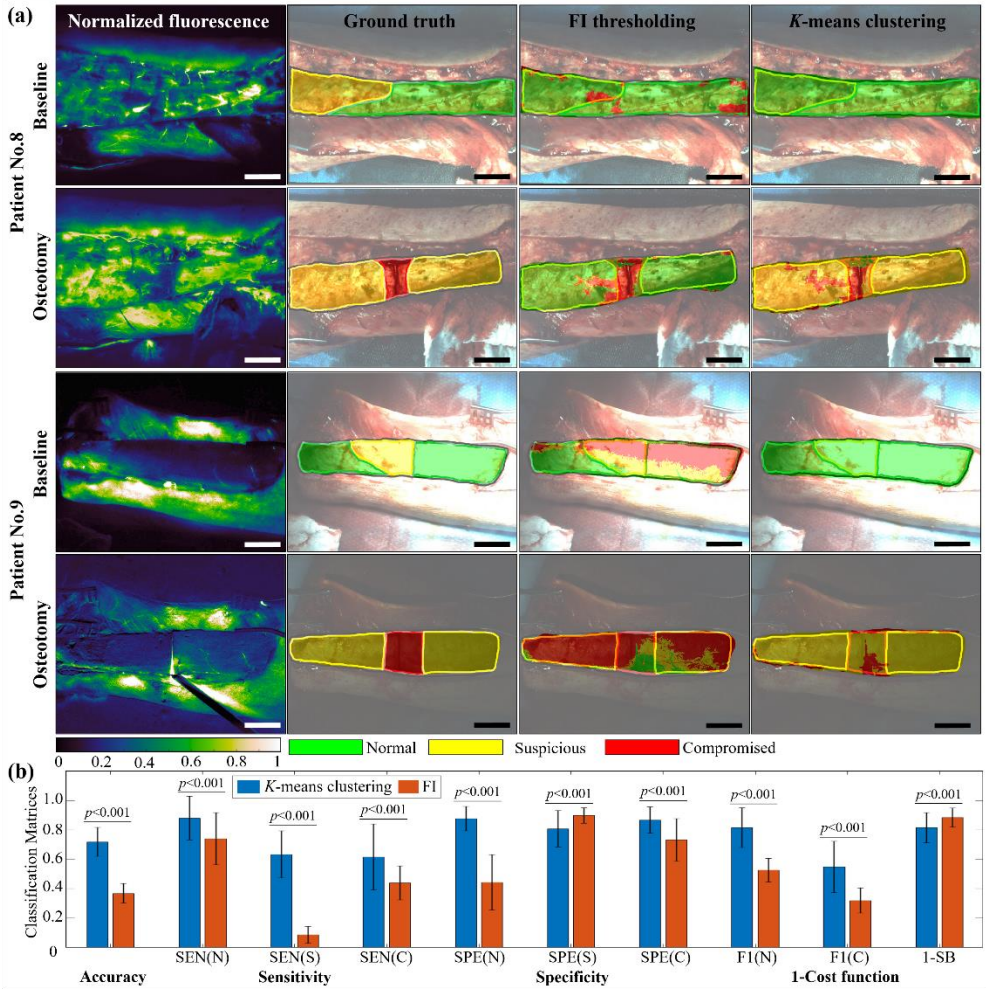

Figure 6.7: Cross-validation results. (a) Cross-validation round 1. Comparison of tibia bone perfusion maps for patients 8 and 9 before and after osteotomy. Column 1: Normalized fluorescence image at peak intensity time; Column 2: Ground truth maps delineated by experienced surgeon: green are outlines the bone region with normal perfusion, yellow – suspicious region, red - compromised region; Column 3: Perfusion map predicted by FI thresholding classifier; Column 4: Perfusion map predicted by *K*-means clustering classifier. Scale bars are 3 cm. (b) Averaged accuracy, sensitivity, specificity and 1-cost functions over all cross-validation rounds of *K*-means clustering-based and FI thresholding classification. Each round was tested on approximately 1×10^6 pixel-to-pixel ROIs. Error bars = mean ± standard

deviation of 36 rounds. All results from two classifiers are statistically different with p-values < 0.001.

6.3.4. The trained classification machine exhibited generalizability when applied to a blind set of newly collected surgical datasets

To confirm the generalizability of the classification machine when applied to new imaging data representing a 'blind set' that model had not seen. This was done to rule out overfitting, also referred to as "developing to the test set" during the initial model evaluation and selection. The classification model defined in the first nine patients, and evaluated using cross-validation, was tested on a blind set of nine image series acquired in three additional patients. Finalized centroids defining the classification model were determined to be: centroid of normal = (-1.378, -0.167, 0.014), centroid of suspicious = (0.175, 0.472, -0.014), and centroid of compromised = (0.718, -0.449, 0.007). In the additional 'blind set' patients, label predictions using the *k*-means clustering model defined by these centroids was able to reliably classify the ROIs into "normal", "suspicious" and "compromised" categories that were consistent with their clinical conditions (**Figure 6.8**): As the manipulation of blood flow became more severe, the predicted categories changed to more severe conditions, demonstrating good generalizability. Note that, for half of the patients who received a removal of the distal foot before baseline imaging, it is not expected that baseline will be completely "normal".

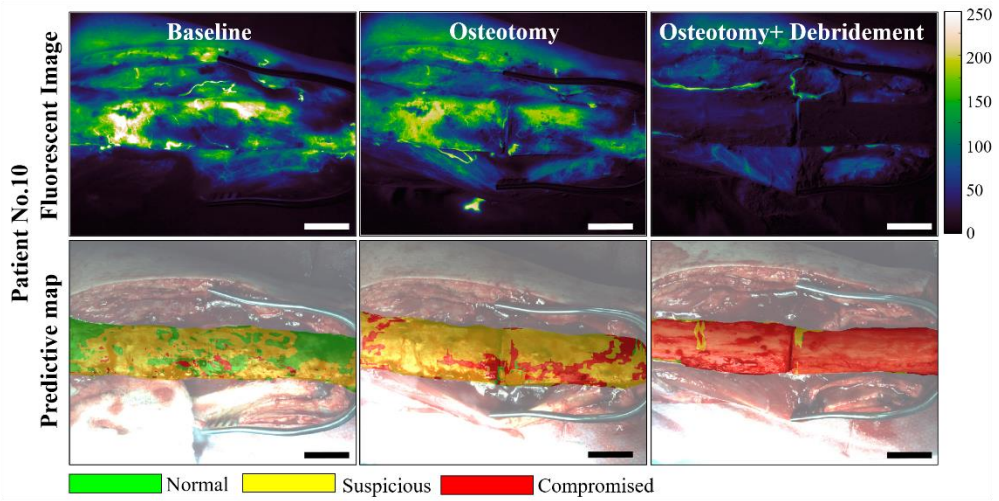

Figure 6.8: Evaluating classification generalizability on an additional unseen patient (Patient 10). Left: Baseline, **Center**: Osteotomy, **Right**: Osteotomy+Debridement. Row 1: Fluorescent images, Row 2: Perfusion predictive map. Green-normal perfusion, yellow-suspicious perfusion, red-compromised perfusion. Scale bars are 3 cm.

6.4. Discussion

Contrast-enhanced fluorescence imaging is being deployed across surgical specialties, including surgical oncology [300], gastrointestinal surgery [301] and plastic surgery [302], but only recently have there been attempts to use quantitative methods to guide orthopaedic surgery [19,21,128,303]. Kinetic analysis requires continuous fluorescence imaging and advanced mathematical computation which is not available in the software of current commercial imaging units. For this reason, the most common implementation of ICG imaging is to simply use the maximum or single time-point intensity image to assess perfusion [304]. Another reason why explicit kinetic models may be challenging in all but a handful of well-defined pathologies, is the common scenario where regions of tissue are supplied by multiple vascular inputs and where a variety of disease processes may act together to produce competing effects. For these reasons, it is useful to explore alternative approaches to both simple parameters and explicit kinetic

models. To this end, we leverage texture-based and kinetic-driven features as part of a machine learning classification. The exact kinetic mechanisms of the underlying pathophysiology need not be known, so long as the spatiotemporal behavior in diseased or compromised tissue is distinct from normal tissue. In this paper, we deploy unsupervised *K*-means clustering of principle components reduced from twenty-one spatiotemporal features, and report its performance as a classifier of bone viability, but also regard this approach as paradigmatic of a class of approaches that could be brought to bear on this problem-space.

The proposed approach is simple, fast, works well intraoperatively with high generalizability, and can be easily translated to the clinic: No input labels are required, and features are a subset of well-defined radiomic features [210,305], thus this approach is easy-to-use and easy-to-interpret; This approach relies on first-pass wash-in and early wash-out process, as opposed to kinetic modelling methods that require longer imaging to capture wash-out [19,21]—an important consideration for intraoperative use. Additionally, the computational speed has been accelerated by PCA-based feature dimensional reduction, resulting in a rapid and timely read-out which could be used to guide surgeon decision-making. Compared to classification by fluorescence-intensity alone (*i.e.*, a single continuous variable), with optimal thresholds that are fast but less accurate, *K*-means clustering shows superior performance in all important benchmarks. It has high sensitivity to bone across all perfusion levels, while FI thresholding has very low sensitivity to low-to-moderately perfused bones. Likewise, the specificity of *K*-means clustering is consistently high across perfusion levels, while FI thresholding has high specificity to only moderately perfused bones. More importantly, *K*-means clustering increases the surgeon's

burden (number of pixels labeled 'suspicious' which must be examined closely by the surgeon) only modestly and without bias while FI thresholding classifier demonstrates high bias against middle level bones. Moreover, when centroids defined by the first 9 patients were used to classify a 'blind set' of 9 image series from 3 additional patients, the performance was reproducible showing strong generalizability to future cases of real-world data. Cross-validation using testing patients excluded from training also proves the high generalization ability of this approach (**Table 6.2**). Utilizing the clinically well-used SPY Elite imaging system further increases the possibility of clinical translation, and since the classification is performed independent program of the imaging system, has no effect on the imaging performance or workflow. Taking all the above metrics into account, the unsupervised model has the potential to enhance the identification and removal of devitalized bone during debridement surgery, which could reduce ongoing infection, minimize unnecessary tissue removal and subsequent deficit, and reduce cognitive burden on the surgeon.

Table 6.2: Summary of validation procedures.

Validation Approach	Patient IDs	No. of injections	No. of Training ROIs	No. of Testing ROIs	Result
Leave *p* out Cross-Validation	01-09	27	2.5×10^6	1×10^6	Accuracy of 72%, Sensitivity of 62-88%, and Specificity of 87-88%
Blind Validation	10-12	9	n/a	8×10^5	Generalizability and Stability confirmed.

There are a few limitations, however, that are important to mention. First, while this is the largest ICG imaging study of amputation patients to date, with twelve patients undergoing imaging during three conditions each (containing 3.5×10^6 ROIs from 27 time-

series of 1020 images), from machine learning perspective, the data from each pixel is not perfectly independent. Nevertheless, this study focused mainly on 1) a novel framework to combining spatial and temporal features of DCE-FI to classify bone viability and 2) showing its generalizability in a very unique human clinical dataset. Evaluation of this approach in a larger and more independent dataset is forthcoming.

Second, the feature-set and size of the dataset only supported the stratification of bone state into three perfusion levels, resulting in some ambiguity in diagnostic classification. This could be especially important when applying the approach to less controlled scenarios, such as infected fractures and repeat debridement, where bone is already tampered with. In these cases, patient group specific models will need to be defined, or additional sources of information obtained (*i.e.*, fluorophores that target infection and/or new bone modeling).

Third, there is unfortunately no gold standard for determining whether the tissue in these patients is actually compromised, since no such clinical technique is available (the motivation for this work); ground truth was provided by subjective evaluation of an experienced surgeon. Given that this subjective approach is known to be deficient, the assessed accuracy is confounded by any human error in region identification (*i.e.*, the model could correctly predict the classification while the human 'ground truth' could be wrong).

Finally, the features selected for this study emphasized the spatial variations over the temporal ones, and a more exhaustive evaluation of temporal dynamics is warranted. However, it was beyond the scope of this initial report, and we selected the variation from

global peak intensity to 120 seconds post-peak, because this time window is believed to be the best representation of the whole fluorescent video.

Future work will incorporate model-independent parameterization of kinetic information using deconvolution and statistical moments, as additional features. Furthermore, since data was analyzed off-line in this *observational* clinical study, we focused on development of the analytic pipeline without concern for computational time. However, to provide on-line intraoperative predictions, we will port the in-house developed code to python and utilize the well-established optimization methods available for image processing, feature extraction, PCA and classification to greatly improve computational speed. We conservatively estimate a reduction in computational time to under 1 minute, which can be tolerated by the constraints of surgical workflow.

6.5. Conclusions

This chapter demonstrates a model-independent approach to classification of bone into normal, suspicious, and compromised states; it is trained on 27 image series acquired in nine amputation procedures, and evaluated with cross-validation as well as on imaging data acquired from three additional patients. The amputation procedure offers a unique opportunity to image baseline and two manipulated conditions in a carefully controlled manner in humans, to build a classification machine. This unsupervised approach can reduce the artificial error, accelerate the training process, and appeal to larger group of non-expert users. However, future work will apply this approach to other types of surgical procedures with larger patient datasets, will consider additional temporal features such as empirical kinetic-related parameters, and improve the classification precision in further

investigation of the utility of *k*-means clustering algorithm as a decision-making tool for bone debridement.

In this chapter, the usage of DCE-FI texture analysis has been evaluated in bone injury classification. The spatial and temporal features have demonstrated high accuracy and sensitivity in classifying bone ROIs according their perfusion levels. This study examined our central hypothesis of this thesis that DCE-FI can provide features highly correlated to perfusion in real patient data. Therefore, future work can utilize this property of DCE-FI and apply to more complex clinical problems.

Chapter 7

Risk prediction on orthopaedic trauma patients for fracture-associated infection using DCE-FI

This chapter describes the work from "Risk prediction on orthopaedic trauma patients for fracture-associated infection using dynamic contrast enhanced-fluorescence imaging" by Han X, Bateman LM, Werth PM, Jiang S, Gitajn IL, and Elliott JT, *in press* in *Proc. SPIE*, Molecular-Guided Surgery: Molecules, Devices, and Applications IX in 2023. Jonathan T. Elliott supervised the project, provided intellectual inputs and reviewed the manuscript. I. Leah Gitajn and Shudong Jiang provided intellectual inputs and reviewed the manuscript. Paul M. Werth offered suggestions on statistical analysis and machine learning. Logan M. Bateman assisted with data collection. The author of this thesis designed the study, analyzed the patient data and images, wrote analytic software, and wrote the manuscript. This chapter has meet relevant copyright permission requirements.

In this chapter, a post-trauma infection risk prediction method has been developed and evaluated in orthopaedic trauma patients. Based on a previous fracture-associated infection risk score system, we added image-based features and kinetic features using dynamic contrast-enhanced fluorescence imaging (DCE-FI). In this way, we can not only predict the probability of the presence of infection, but also provide a color-coded predictive map that can visualize the boundaries among multiple levels of infection risks.

7.1. Introduction

Surgical site infection (SSI) following fracture and soft tissue repair can have devastating consequences, making SSI is one of the most challenging postoperative complications in orthopaedic trauma, and represents 15.6% of total postoperative complications in the field of orthopaedic surgery [4]. The cause of SSI is multifactorial, resulting from residual foreign bodies, injured and inflamed bone/tissue resulting from the mechanism of trauma, as well as incomplete primary surgical debridement that did not completely remove devitalized tissue. Treatment failure in the context of SSI results in increased morbidity, loss of function and even amputation [6]. Thorough debridement is considered critical in the management of SSIs, and it is the primary step before the definitive fixation for mechanical stability. However, thorough debridement is challenging because it is often difficult to determine the location and extent with which tissue should be debrided, using current clinical tools [10–13].

To guide surgical debridement and reduce the incidence of SSI, a functional intraoperative imaging system capable of visualizing the amount and location of infected tissue is needed. Dynamic contrast enhanced (DCE) imaging is an intraoperative imaging technique that can provide quantitative information [19,21,128], it works by analyzing the temporal intensity changes of injected contrast agent, so qualitative information of the location as well as quantitative information can be extracted. Compared to other imaging modalities, DCE-FI is safer by not using ionizing radiation, and is versatile by updating images in real-time [112]. DCE-FI with contrast agent of indocyanine green (ICG) have been developed recently by preclinical studies [19,21,97,261–263] to assess bone perfusion

while providing guidance for surgical debridement. The application of DCE-FI will achieve a more controllable SSI treatment and a better patient outcome.

The problem of infection prediction is an appropriate application for machine learning classification, with many aspects that make it well-suited. Infection predictive factors in this study are multidimensional, and include a number of imaging spatial features, kinetic features and informatic features. First, with regards to spatial features (also called 'imaging features' in radiomics), several recent studies on orthopaedic surgery have applied texture-based machine learning classification, including for bone age detection [240], osteoporosis detection [216], bone disorder classification [215] and fracture risk prediction [219]. Second, with respect to kinetic features extracted from tracer kinetic theory of fluorophore temporal curves, the predictive values of these features have been demonstrated by several pre-clinical studies [14,15,37] Third, informatic features include demographics, comorbidities, clinical and laboratory test results, and based on work done by the Shock Trauma team, a postoperative infection risk score model [18] showed good prediction on infection risks. Current applications using informatic features as predictive tools are mainly in periprosthetic joint infection prediction [241].

In this study, we developed a multidimensional, multilevel infection prediction model for orthopaedic trauma patients. Predictive features include non-parametric temporal variables and spatial texture variables extracted from DCE-FI images, and patient's risk of developing infection using the established metric. These features were evaluated for their ability to predict the composite outcome score, and have shown good predictive ability. This proposed post-traumatic infection predicting model has great

potential for clinical translation and will benefit both surgeons and patients by shortening surgery time and improving the postoperative outcomes.

7.2. Methods and Materials

7.2.1. Clinical investigation

This study (**Figure 7.1**) is approved by the Institutional Review Board of the Dartmouth-Hitchcock Medical Center (DHMC) and listed on ClinicalTrials.gov as NCT04403204. In this study, twenty-four participants undergoing open-fracture surgery with various levels of extremity trauma are included in this study. Eligible participants are selected as 18 years of age or older who present to DHMC and scheduled for an open-fracture surgery. Iodine allergy and pregnant or breastfeeding woman have been excluded from this study. Recruitment, exposure, and data collection periods of participants were January 2020 to August 2022, and the participants have one follow-up visit after 12 months. 25% participants have SSI confirmed by follow-up visits. Informed consent was obtained from the participants and/or their legal guardians. All methods were performed in accordance with the relevant guidelines and regulations. 0.1 mg/kg intravenous injection of ICG was injected intravenously. For 20 seconds before and for 4 minutes after the injection, fluorescence images of surgical areas were recorded using SPY Elite imaging system (Stryker Corp., Kalamazoo, MI, USA) equipped with 805 ± 10 nm laser diode for ICG excitation and NIR charge-coupled device camera with 820 – 900 nm band pass filter.

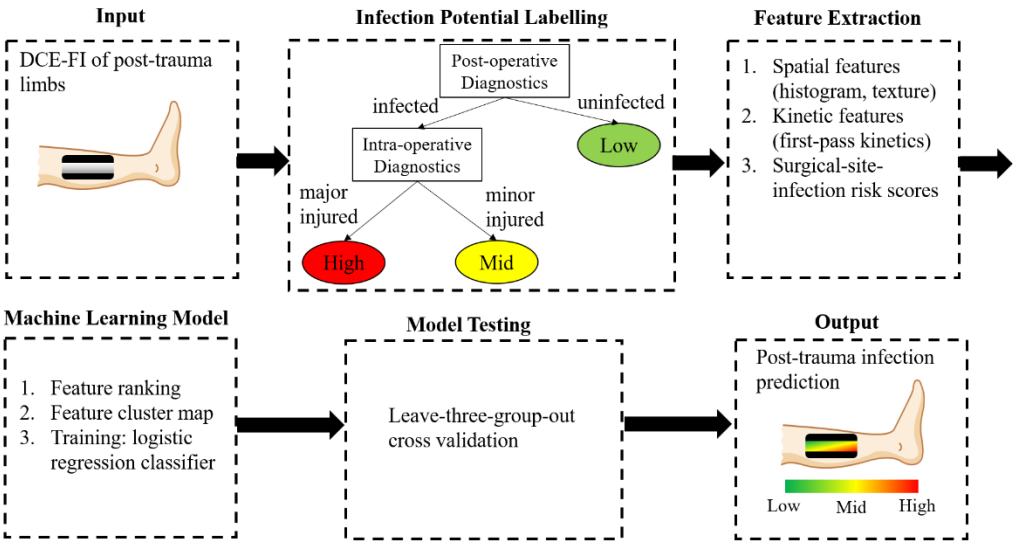

Figure 7.1: Pipeline of the study.

7.2.2. Image processing

Recorded images were processed using our own in-house developed MATLAB (R2022a, MathWorks, MA, USA) program. 400-800 square regions-of-interest (ROIs) of side 1 mm, located side-by-side, were selected from time series images of each participant. ROIs which are not within the region of bone were deleted, and one ROI was regarded as one data point.

7.2.3. Machine learning and statistical analysis

Predictive features were extracted from each ROI, including tracer kinetic parameters which we have previously evaluated in a controlled perturbation study [19] (f1-f8: Time-to-peak (TTP), Maximum intensity (Imax), Ingress slope (IS), Egress slope (ES), Area-under-curve (Iauc), Intensity at global peak (I_p), Intensity at 60 s following global peak (I_{60}) and Intensity at 120 s following global peak (I_{120})), spatial texture parameters (f9-f12: Contrast, Entropy, Correlation and Homogeneity) [20], and f13: SSI risk score

(SSI) [18]. A composite outcome label (infection potential low/mid/high) was assigned to each ROI. The composite outcome label was based on variables of (1) the pixel-level surgeon annotation of most- and least-damaged tissue, and (2) infection status after 12-month post-surgery. The composite outcome score system has combined pixel-level identification by the surgeon with patient-level infection outcome, allows for pixel-level predictions. Machine learning classification was done by logistic regression classifier (sklearn package, Python 3.9, hyperparameters are: *solver = "lbfgs", c = 1, penalty = "l2"*). Leave-p-groups-out cross-validation (p = 3. At each round, select 21 patients' data for training and 3 patients' data for testing) was used for evaluating the accuracy and sensitivities.

Features were evaluated for their ability, either independently or in combination, to predict a composite outcome score. Firstly, one-way ANOVA statistical analysis on individual features was performed to test the power of extracted features, with significant level of 5%. Secondly, Pearson correlation coefficient matrix of each feature pairs was computed on the normalized feature values to range 0~1. Thirdly, features were ranked according to how many times in total (min = 0, max = 3) they were selected as the top-five features, by any of the following three methods: Pearson correlation coefficient to labels, chi-square tests, and recursive feature elimination.

7.3. Results

7.3.1. Features distribute differently among different potentials of infection

According to feature ranking (**Table 7.1**), the top five ranked features are f13: SSI, f2: Imax, f1: TTP, f5: Iauc, and f11: Correlation (**Figure 7.2**), which have been selected

3/3/2/2/2 times, respectively. All these features distribute differently among different infection potentials. In detail, f13: SSI ranges have increased with increasing potentials, and have significant differences among low versus mid and high; others ranges have decreased with increasing potentials, and have significant differences among low and mid versus high. As a result, these extracted features can be used as predictive variables for infection potentials.

Table 7.1: Feature ranking. TRUE means the feature was selected by the method, and FALSE means not selected.

Feature	Pearson Correlation Coefficient	Chi-square Tests	Recursive Feature Elimination	Total Times Selected	Ranking
f13: SSI	TRUE	TRUE	TRUE	3	1
f2: Imax	TRUE	TRUE	TRUE	3	2
f1: TTP	TRUE	TRUE	FALSE	2	3
f5: Iauc	FALSE	TRUE	TRUE	2	4
f11: Correlation	TRUE	TRUE	FALSE	2	5
f3: IS	FALSE	FALSE	TRUE	1	6
f8: I_{120}	FALSE	FALSE	TRUE	1	7
f12: Homogeneity	TRUE	FALSE	FALSE	1	8
f6: I_p	FALSE	FALSE	FALSE	0	9
f7: I_{60}	FALSE	FALSE	FALSE	0	10
f10: Entropy	FALSE	FALSE	FALSE	0	11
f4: ES	FALSE	FALSE	FALSE	0	12
f9: Contrast	FALSE	FALSE	FALSE	0	13

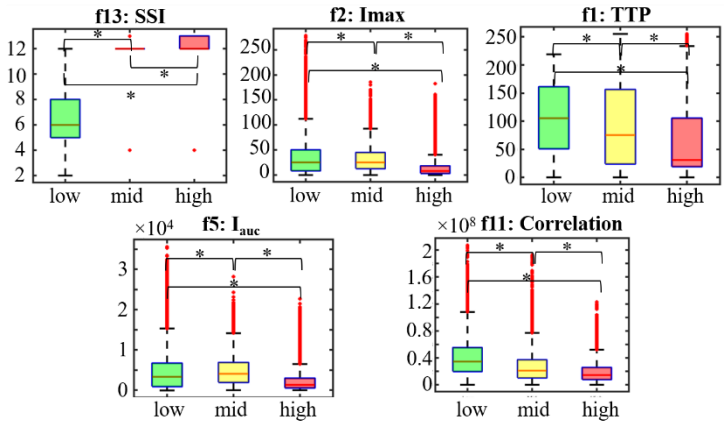

Figure 7.2: Boxplots of top-five ranked features. Box colors represent the infection potentials: Green = low potential, Yellow = mid potential, and Red = high potential. * P-values < 0.05.

7.3.2. Features showed spatial clustering in different potentials of infection

In addition to distribution, features also showed spatial patterns of clustering when the feature heatmap was plotted (**Figure 7.3**). In this heatmap, each row represents a feature and rows are sorted in order of increasing rank correlation to the Low/Mid/High label, from negative to positive correlation. For example, correlation showed a stronger negative correlation with low correlation being associated with the 'high' classification label, and high correlation being associated with the 'low' label. The higher a feature correlated to given labels, the clearer the clustering is. For example, f13: SSI at the first row showed a clear two-cluster pattern: low versus mid and high; Features in the second to 9th rows showed also a two-cluster pattern: mid versus high. Therefore, when combined all the features together in prediction, then three-level infection potentials: low versus mid versus high can be well-separated.

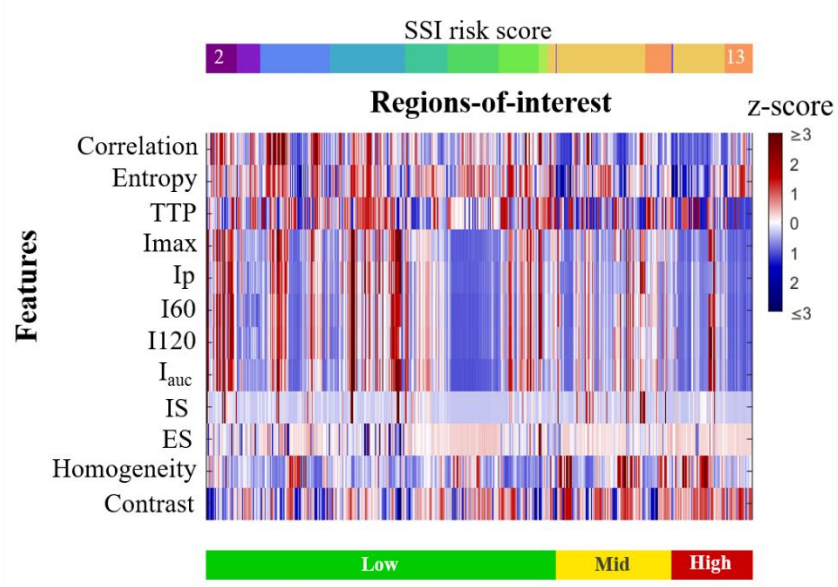

Figure 7.3: Feature z-score heatmap. First row is the f13: SSI risk score, which can be calculated prior to surgery from patient specific variables. Subsequent rows are imaging features, sorted according to spearman rank coefficient with the final row, the three clusters of given labels. Each column represents a single region-of-interest from the 24 patients, and colored according to normalized z-score for comparison across features and patients.

7.3.3. Machine learning classification has high performance in predicting infection potentials

By using leave-three-group-out cross-validation, the machine learning classifier yielded an average accuracy of 0.86, sensitivity of low potential of 0.98, mid potential of 0.77, and high potential of 0.51 (**Table 7.2**). These scores demonstrated the high performance this classifier has on classifying infection potentials in three-level (**Figure 7.4**).

Table 7.2: Cross-validation results at each round. Sensitivity of mid and high potentials are missing at some rounds, because the testing patients in such rounds contain only low potential ROIs.

#Round	Training patient IDs	Testing patient IDs	Accuracy	Sensitivity (low)	Sensitivity (mid)	Sensitivity (high)
1	4~24	1, 2, 3	0.89	1	0.74	0.42

2	1~3, 7~24	4, 5, 6	1	1	/	/
3	1~6, 10~24	7, 8, 9	0.71	1	0.73	0.57
4	1~9, 13~24	10, 11, 12	0.71	0.79	0.79	0.50
5	1~12, 16~24	13, 14, 15	0.83	0.99	0.83	0.49
6	1~15, 19~24	16, 17, 18	1	1	/	/
7	1~18, 22~24	19, 20, 21	0.96	0.96	/	/
8	1~21	22, 23, 24	1	1	/	/

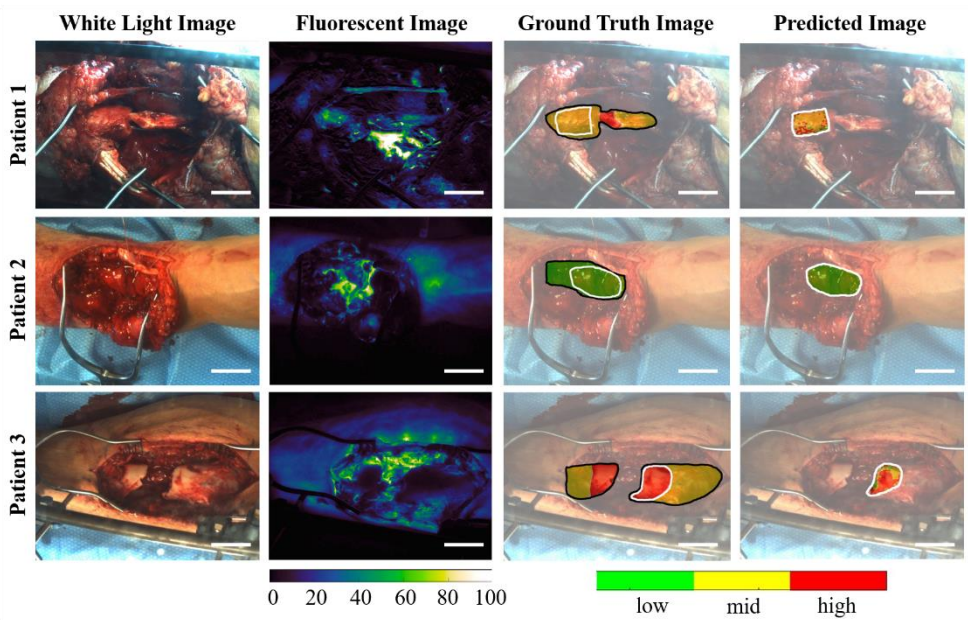

Figure 7.4: Predicted infection potentials by machine learning classification. Row 1: A male open-fractured lower extremity patient with confirmed infection; Row 2: A male open-fractured lower extremity patient with confirmed no infection; Row 3: A male open-fractured lower extremity patient with confirmed infection. Column 1: White light image; Column 2: Fluorescence image at peak intensity time; Column 3: Ground truth maps delineated by experienced surgeon: the solid black lines delineated the regions of bone, and the solid while lines delineated the regions of interest. Infection potentials were color-coded as: green - low infection potentials, yellow – mid infection potentials, red – high infection potentials; Column 4: Infection potential map predicted by machine learning. Scale bars are 3 cm.

7.4. Discussion

Predicting the potential of a given region of tissue to develop subsequent infection is an important task for orthopaedic surgeons. They must make a timely assessment of bone/soft tissue status and then either remove or spare the tissue during debridement. Removing too much tissue lengthens the recovery time; removing too little can lead to infection and its dire sequelae. This paper presents several key features, obtained from dynamic contrast-enhanced fluorescence images, that can indicate the presence, or future likelihood, of infection. These factors include imaging features, kinetic features and informatic features. These features reveal important clinical information through different mechanisms. Imaging and kinetic features can provide information of bone perfusion, which is a key indicator of bone viability [14,33,34,36,37]. Informatic features, as a previously established infection risk score model [18] indicated, can reflect the possibility of getting infection. In this study, a combination of these three feature categories has two main advantages in infection prediction. First, the prediction is in tissue-level. Every single tissue in bone, visualized as a few pixels in fluorescent image, can be predicted as low/mid/high in this study. Therefore, this study can provide a visual guidance for surgeons on the tissues that need their attentions. Second, the prediction is in real time. The imaging system in this study is intraoperative, and the prediction results can be calculated in minutes. As a result, this study opened up possibilities to efficiently predict bone infection intraoperatively.

One of the most promising ways that fluorescence-guided surgery could improve outcomes for patients, is in providing guidance to inexperienced surgeons who serve at small local hospitals, or are called upon during disaster or war. In fact, the recent war of aggression against Ukraine demonstrates the enormous burden placed on all levels of care

when attempting to triage and treat orthopaedic trauma—the most common injury in this scenario. Here, surgeons who are not used to treating Gustilo Type III fractures would benefit from a system that could be deployed to image, and then leverage the predictive models trained *a priori*. Such a tool has the potential to bring up the performance of the 'bottom'—those surgeons who are not experienced or accustomed to treating such injuries—thus having the largest marginal impact in terms of patient outcome.

7.5. Conclusions

In conclusion, a multidimensional predictive model has been developed for post-trauma patient at risk of fracture associated infection. The model is based on spatial and temporal variables from DCE-FI images, and patient demographics. This risk predictive model has high accuracy, and it will improve both research and clinical application of DCE-FI in bone infection.

This chapter demonstrates that DCE-FI derived image features and kinetic features can enable the prediction the risk of infection. Chapter 5-6 show how the texture features and kinetic features of DCE-FI related to bone perfusion levels, and in this chapter, the relationships are further expanded into predicting negative outcomes. This is consistent with our central hypothesis that DCE-FI measurements are not only reflective of perfusion, but also capable of prediction outcomes associated with bone devitalization.

Chapter 8

Conclusions and Future Studies

This chapter summarizes the thesis on intraoperative quantification of bone perfusion in lower extremity injury surgery. As the objectives of this thesis were addressed, firstly, we described two preclinical studies for validating bone perfusion quantification and infection assessment, respectively. In Chapter 3, a ground truth approach for measuring bone perfusion has been developed, by quantifying fluorescent microspheres (FM) *in situ.* This approach can visualize bone perfusion in 3D, and validate the following image-based analytical approaches. In Chapter 4, a dynamic contrast-enhanced fluorescence imaging (DCE-FI) characterization of bone infection development has been established in a rodent low-energy fractured Methicillin-resistant *Staphylococcus aureus* (MRSA) contaminated femur model. This model can validate the infection risk prediction in Chapter 7. Secondly, image-based analytical approaches on clinical assessing bone perfusion during orthopaedic trauma surgery has been developed in Chapter 5 and Chapter 6. Chapter 5 focuses on kinetic analysis on image-based data, and Chapter 6 mainly uses texture analysis on the same data. Finally, extended from bone perfusion assessment, clinical bone infection risk prediction has been accomplished by a multidimensional fracture-associated infection predictive method, as described in Chapter 7.

This chapter also discusses the future studies related to the thesis work. Future work includes improving kinetic analysis on dynamic contrast-enhanced imaging, clinical validation of bone infection risk prediction, and MRSA characterization in multi-level injured fracture.

8.1. Summary of Research Objectives

8.1.1. Development of ground truth approach for bone perfusion measurement

Lacking of objective instruments or techniques for bone perfusion measurement has been a major barrier in bone imaging study. In Chapter 3, We have proposed a novel approach that will provide *in situ* bone perfusion assessment, by exploring the possibility of applying FM technique in fluorescence-guided-orthopaedic-surgery. The approach is a modified FM quantification technique using custom-built multi-channel cryomacrotome, which we have termed "mQUIC". This approach will further enhance fluorescence-guided surgery (FGS) by validating it with a quantitative perfusion standard. In mQUIC, perfusion is computed by identifying the density of deposited microspheres in reconstructed imaging volumes, which are proportional to regional blood flow.

The methodology of this study involves phantom study, rabbit femur study, image processing, and volumetric analysis. The multi-channel cryo-imaging has been tested in phantom to have linear response to the number of microspheres, and independent of the color of microspheres. In the rabbit femur model, cryo-imaging was used to scan the femur injected with three colors of microspheres corresponding to three conditions: baseline, post-osteotomy and post-periosteal stripping. In near infrared (NIR) monochrome channels, image processing, such as top-hat transform and object-based colocalization analysis, was used to enable accurate counting of FMs to produce a volumetric map. In visible channel, we have successfully segmented bone and its surrounding muscle, and then incorporating these volumetric renderings into the visualization. Combined NIR and visible channel together, FMs from bone segmentation as well as muscle segmentation has been recovered, their number has been counted, and they have been plotted in 3D space with color-coded

spatial density. Finally, the volumetric FM density map is converted to bone perfusion units (mL/min/100 g) using the reference organ technique, and both endosteal and periosteal regions can be visualized separately. Therefore, mQUIC technique will be applied as a gold standard for measuring bone perfusion in orthopaedic surgery in planned validation studies.

8.1.2. Dynamic contrast-enhanced fluorescence imaging characterization of bone infection development in animal model

Dynamic contrast-enhanced fluorescence imaging can predict the risk of bone infection when combined with basic health information in the clinical study discussed in Chapter 7. Besides, when used alone, this imaging system has also demonstrated the characterization of bone infection development in rodent model as described in Chapter 4.

In particular, we established a rodent osteomyelitis study to examine the changes in perfusion before and after bone infection by first-pass kinetics of DCE-FI, and evaluated the growth of MRSA biofilm by bioluminescent imaging. We found that first-pass kinetic parameters—maximum intensity, time-to-peak, and ingress slope—has shown changes demonstrating the decrease of perfusion after MRSA contamination. This result shows that DCE-FI can quantify infection-induced perfusion changes, and therefore DCE-FI can be applied in assessing fracture-associated infection.

8.1.3. Image-based analytical approach on bone perfusion assessment

Image-based analytical approach of assessing bone perfusion was developed into two types, kinetic analysis and texture analysis, which are addressed separately below.

Chapter 5 highlighted the first-pass kinetic analysis in amputation patient characterization and classification. We conducted this study aiming at differentiating bone perfusion levels intra-orthopaedic-operatively. DCE-FI has been investigated clinically in eleven adult patients undergoing below knee leg amputation. This is the first clinical study of quantitative DCE-FI in orthopaedic surgery, which opens up new possibilities of intraoperative bone state assessment. The proposed quantification is based on analyzing the first-pass kinetic parameters of fluorescence image series acquired during the indocyanine green (ICG) wash-in and wash-out, such as maximum intensity, time-to-peak and ingress slope. More importantly, to address the intersubject variations, we corrected the above first-pass kinetic parameters by substituting subject specific- arterial input function (AIF) with population averaged AIF. AIF associated factors are the main source of error in quantitative analysis of DCE-FI. AIF correction can efficiently eliminate the population variation caused by AIF-related perturbations and improve the significance of the first-pass kinetic analysis. Furthermore, a bone state classification model has also been developed, by using machine learning classification with AIF-corrected first-pass kinetic parameters. Therefore, bone regions-of-interest (ROIs) can be classified as "major injured" and "minor or no injured" with high accuracy and sensitivity. This study evaluated the application of DCE-FI in orthopaedic surgery, and further improve the translation of quantitative analysis to clinics.

Chapter 6 described the dynamic contrast-enhanced texture analysis on orthopaedic trauma surgery. We conducted texture analysis of DCE-FI in clinical amputation data, and explored the capability of DCE-FI to predict bone perfusion in patients undergoing amputation surgery. This study created artificial conditions representing fracture and

degloving injury by transverse osteotomy and periosteal stripping, and acquired the DCE-FI images on each condition. The goal is to develop a classification strategy to predict whether a particular region is damaged or not. Specifically, we proposed an unsupervised machine learning approach to predict the perfusion or viability level of any bone ROI based on 21 spatiotemporal features. 2.5×10^6 segmented ROIs at bone region were included to train the model; 1×10^6 ROIs were used for testing the model using a cross-validation approach; output labels were compared to model predictions and to a benchmark fluorescence intensity thresholding-based label. The reported unsupervised classification approach, using a combination of extracted spatial features and temporal features from DCE-FI fluorescence images, demonstrated the ability to reliably stratify ROIs into three perfusion levels: "appearing normal", "appearing suspicious" (further attention warranted) and "appearing compromised" (debridement recommended to completely remove the devitalized bone), and produce outlines that are comparable to segmentation boundaries performed by an experienced surgeon. The classification is fast (accelerated by including principal component analysis for dimension reduction), robust and straight-forward (simple to train because *k*-means clustering classification is used which need fewer data and no input labels), and can be applied with commercially available intraoperative imaging systems without any additional hardware. This first translational bone perfusion classification approach, applied to a highly unique patient dataset, can be readily deployed in other centers and has significant clinical potential not only in lower-limb amputation but in a wide variety of orthopaedic trauma settings.

8.1.4. From bone viability classification to bone infection risk prediction

As discussed above, quantifying bone perfusion is essential for guiding orthopaedic surgery. We have described the application of bone perfusion quantification in bone viability classification in Chapter 5-6. Here we expand from bone viability classification to bone infection risk prediction, in respect to the fact that perfusion plays a determinant role in both bone viability and bone infection.

To understand the relationship between DCE-FI features and the propensity of that tissue to develop future infection, square regions-of-interest of side 1 mm from twenty-four open fracture patients were labeled by a composite outcome (low risk, mid risk and high risk). The label was assigned according to a composition of (1) surgeons distinguish of regions with ("most damaged") and without ("least damaged") obvious signs of pathology, and (2) infection status based on follow-up data of 12 months post-surgery. Predictive features extracted from each ROI include non-parametric temporal variables, parametric temporal variables, spatial texture variables extracted from DCE-FI images, and patient's risk of developing infection using the established metric. These features were evaluated for their ability to predict the composite outcome labels, and have shown good predictive ability (accuracy = 0.86). This proposed post-traumatic infection predicting model has great potential for clinical translation and will benefit both surgeons and patients by shortening surgery time and increasing the postoperative outcomes.

8.2. Suggested Future Studies

8.2.1. Improving kinetic analysis on dynamic contrast-enhanced imaging

In this thesis, we focused on model-independent kinetic analysis using first-pass parameters such as maximum intensity, time-to-peak, ingress slope, and egress slope.

Model-independent kinetic analysis benefits from no prior assumptions on physiological status, easy implement, and so on. However, there are some limitations along with such benefits. One obvious limitation is no direct relation with the physiology of the underlying system. Although the model-independent parameters reflect some physiological quantities such as fractional blood volume and blood flow [89,189], they cannot provide descriptive information about the physiological mechanisms [306]. Therefore, in future studies we are going to improve the kinetic analysis by making it more descriptive.

Compared to model-independent approaches, model-dependent ones are physiologically more accurate in describing the system. In model-dependent approaches, the system is modeled by mathematical equations that approximating the physiological reality [188]. Compartment modeling describe the physiological system into some individual compartments that interact with each other by diffusion and exchange. Therefore, the dynamic behavior of the system can be described and quantified through physiological parameters that explicitly incorporated into the compartment model. In the future, we are going to include model-dependent compartment models such as adiabatic approximation to the tissue homogeneity (AATH) and Hybrid plug/flow compartment (HyPC) model, as introduced in section 2.3. For the study described in Chapter 4, in addition to extract maximum intensity, time-to-peak and ingress slope from temporal curves of fluorescent intensities, we will further fit the curves by HyPC model, deconvolve to get the impulse residue function, and compare with the experimental data. And for the infection prediction study highlighted in Chapter 6, we will add parameters from HyPC and AATH model as another category of predictive features, and update the infection prediction model.

8.2.2. Clinical validation of bone infection risk prediction

Chapter 7 introduced an infection risk predictive method applying to open-fracture surgery patients. However, due to the limited accessible data, the evaluation process of the proposed method was by internal cross-validation, which cannot validate the generalizability and examine the overfitting problem. Although Chapter 4 developed an animal model to validate DCE-FI in characterizing bone infection status, clinical validation of the proposed method is necessary for pushing forward this method into further clinical trials or commercialization.

Firstly, we will enroll more open-fracture surgery patients in this study. Currently there were only twenty-four useable patient data. The small dataset size has limitations such as overfitting and lack of generalizability. Once we have more enrolled patients from the same patient cohort, we can validate the proposed infection prediction model by using the unseen patients as testing data. In this case, we can further ensure that our proposed model can be applied to general scenarios.

Secondly, we will expand the study in involving multiple institutes. One of the main characteristics of the proposed infection prediction model is that it can be incorporated into various dynamic contrast-enhanced imaging systems without interfering with the hardwires. In particular, the first-pass kinetic parameters are independent of system settings such as resolution, field-of-view, and so on, because the analysis has been normalized by the baseline intensities before the arrival of dye. In addition, the texture features can be adjusted corresponding to the camera settings, by the way of tuning the gray-comatrix parameters used for deriving texture features. Therefore, we can safely apply the proposed

model with minor adjustments in multiple institutes, and in the case, we can further validate the model in a broader application.

8.2.3. DCE-FI characterization of MRSA infection in multi-level injured fracture model

We have established a DCE-FI characterization approach in low-energy fracture MRSA contaminated model in Chapter 4. This model serves as a preliminary study for preclinical MRSA characterization by DCE-FI. We propose a complete animal study that will fully explore the performance of DCE-FI in characterizing MRSA infection development. In this study, we hypotheses that the severer the fracture is injured, the higher the degree of MRSA infection will be developed.

In detail, we will have four experimental groups of rodents with intact, low-energy, mid-energy, and high energy fractured femurs, respectively. We will inoculate same amount of MRSA, and then follow the same surgery and imaging procedures in Chapter 4. According to our hypothesis, we will observe more decreased fluorescence signals from post- to pre-infection as the fracture level is higher. Particularly at the same post-infection day, as the severities of injury increase, perfusion will more dramatically decrease, and DCE-FI first-pass kinetics will change as: maximum intensity be more decreased, time-to-peak be more increased, and ingress slope be more decreased. In addition, we will also observe higher volume of MRSA biofilm as injury levels increase. We will further validate the hypothesized fracture severity–infection development degree relationship by multiple imaging modalities including bioluminescent imaging and micro-computed tomography.

8.3. Conclusions

This thesis systematically presents fluorescence-guided techniques to quantify bone perfusion in lower extremity injury surgery, from benchtop to bedside. An animal model based on fluorescent microsphere technique was established to provide ground truth measurement of bone perfusion. Moreover, an animal fracture-associated infection model was developed to link the perfusion quantified by DCE-FI with the bacterial infection development. These above two preclinical studies provided a blueprint for the following translational studies on DCE-FI guided orthopaedic surgery. Image-based spatiotemporal and statistical features extracted from DCE-FI were used for classifying bone perfusion states in amputation surgery, which provided a visual guidance of debridement boundaries. Furthermore, these perfusion-associated features, when combined with patient demographic information, have been validated for their ability to predict risk of fracture-associated surgical site infections. In summary, fluorescence-guided techniques using DCE-FI can intraoperatively assess bone perfusion and predict bone infection. Applying fluoresce-guided techniques will potentially shorten operational duration, increase success rates, and improve patient outcomes.

Chapter 9

Appendices

Appendix A

Surgical Procedure for Microsphere Injection and Imaging Acquisition

A.1. Surgical preparation and catheterization

1. Anesthetize with 35 mg/kg ketamine, 5 mg/kg xylazine, or 0.1 mg/kg butorphanol.

2. Intubation and anesthesia continued with isoflurane, while being mechanically ventilated to a normocapnic $PaCO_2$ of ~40 mmHg with a mixture of air and oxygen.

3. An ear vein catheter will be placed for indocyanine green (ICG) injection.

4. The right femoral artery and femoral vein will be catheterized for blood collection / microsphere collection, and intravenous fluid infusion, respectively.

5. A femoral vein catheter will be inserted and advanced to the level of the right atrium, then advanced through the septum into the left atrium. The line is secured to the skin of the thigh to avoid catheter injury or movement.

6. Placement in the left atrium will be confirmed with fluoroscopy.

7. The left knee is shaved and scrubbed with chlorhexidine gluconate for non-survival, non-sterile surgery.

A.2. Surgery

1. We will perform the thoracotomy, and then insert a catheter into the left atrial appendage for the injection of fluorescent microspheres.

2. An incision is made on the dorsomedial surface of the leg superficial to the femur.

3. The soft tissue surrounding the femur is blunt dissected away, leaving the femur and intact periosteum exposed. Retractors are used to maintain view of the entire shaft of the femur when imaging.

A.3. ICG imaging and fluorescent microsphere injection

1. Prepare microsphere by vortexing thoroughly 5-15 seconds, placing in ultrasonic water bath for 4 minutes, and vortexing again for 5-15 seconds.

2. A fluorescence camera is placed directly in front of the surgical site for simultaneous imaging.

3. A dye densitometer (DDM) probe is placed on the hind paw of the non-affected leg.

4. Confirm the correct cuffs are inflated/deflated.

5. Microspheres of a unique color (2 ml/kg) are injected directly into the atrial line: Once the microspheres have been drawn into the injection syringe, start the withdrawal pump and make sure blood is flowing freely into the extension tubing. Slow and steady injection over 5-15 seconds, and then flush the dead space of the catheter with warmed saline of three times the volume of catheter.

6. During the injection and washout, blood is withdrawn from the femoral artery at an approximate rate of 0.333 ml/min, starting 1 minute before injection and continuing for 2 minutes after injection. (This blood draw represents the 'reference organ' which allows the fluorescence signal to be converted to units of flow (ml/min/g)) After the end of the withdrawal, the pump is turned off, the stopcocks are opened and the blood remaining in the extension tubing is drawn into the syringe.

7. ICG (0.1 mg/kg/injections, 0.8 ml stock ICG solution with 6 ml saline) is injected into the ear vein, while the fluorescent cameras are acquiring a time series of images. Imagine duration is approximately 5 minutes.

8. 30-minute stabilization period to allow ICG and microspheres to clear plasma. Transfer blood into labeled vials for ref blood sampling. Rinse syringes and extension lines with 2% Tween-80 using twice the volume of the blood and add this rinse to the blood samples.

9. Using a bone saw, two transverse cuts are made midway on the shaft of the femur, so that an approximately 1 cm section of bone is completely detached.

10. Repeat A.3.4 – A.3.8 for ICG imaging and microsphere injection

11. The periosteum proximal to the transverse osteotomy is removed completely from the bone, and hemostasis is achieved using cautery.

12. Repeat A.3.4 – A.3.8 for ICG imaging and microsphere injection

13. A medial parapatellar incision is made and the patella is dislocated laterally

14. A hole of 4.5 mm diameter is drilled with a titanium-coated drill bit from the intercondylar space to the medullary canal.

15. A metallic rod is tapped into the medullary cavity to fix the distal, proximal and 1 cm fragment of the femur.

16. Repeat A.3.4 – A.3.8 for ICG imaging and microsphere injection

A.4. Euthanasia and ex vivo processing

1. Animal is euthanized with euthasol

2. Femur bones or other reference organ are entirely removed, and put into separate containers made by fossil wrap (with least possible height). Fill the containers with optimal

cutting temperature (OCT) compound, and store at -20 °C overnight until cryomacrotome imaging.

3. Reference blood sampling is processed the same way as in the whole blood study.

Appendix B

Texture Analysis of Dynamic Contrast-Enhanced Fluorescence Imaging

B.1. Image texture features

Twenty-one first and second order spatiotemporal features (f1~f21) summarized in **Table B1** were included in this thesis. They included six intensity-based features, thirteen gray-level co-occurrence matrix (GLCM)-based features and two Gamma distribution parameters.

While intensity-based features were straightforward to calculate, GLCM features [211] depended heavily on the pre-set distance between paired neighbors, image rotation angle, aggregating method, the number of gray levels and the range of image intensities [299]. Offset between paired neighbors was set to 2 in order to approximate the ratio of camera resolution and pixel size. Image directions for GLCM calculation included 0-, 45-, 90-, and 135-degree angles. GLCM features were computed for each directional matrix and then averaged. As original fluorescence intensity images were saved in 8-bit format (256 intensity levels), GLCM gray level number was set to 256 to accurately capture information from all image intensities. To avoid overestimation in low vs high image intensity areas, matrices were created symmetrically, with truncated rows and columns containing all zeros, and normalized to the range of [0,1]. Gamma distribution-based features known to be related to tissue effective scatterer number density and size (shape parameter k and scale parameter θ, respectively) were derived by fitting each region-of-interest's histogram of pixel intensities by gamma-function [297].

Table B1. Fluorescence image texture features used for analysis.

#	Order	Texture feature	Physical Meaning	Expressions

f1	1st order	Contrast	Intensity difference between regions of bone and background tissue	$(\frac{1}{N}\sum_{i=1}^{N} Xi - \frac{1}{M}\sum_{j=1}^{M} Xj) \div \sqrt{\frac{\sum(Xj-\bar{X}j)^2}{M}}$ [a, b]
f2		Mean	Average fluorescence intensity of bone regions	$\frac{1}{N}\sum_{i=1}^{N} Xi$
f3		Standard deviation	Square root of intensity variance within the region of interest	$\sqrt{\frac{1}{N-1}\sum_{i=1}^{N} \lvert Xi - \bar{X}\rvert 2}$
f4		Skewness	Asymmetry of the intensity distribution	$\frac{\frac{1}{N}\sum_{i=1}^{N}(Xi-\bar{X})3}{\left(\sqrt{\frac{1}{N}\sum_{i=1}^{N}(Xi-\bar{X})2}\right)3}$
f5		Kurtosis	Bulging rate of intensity distribution within the region of interest	$\frac{\frac{1}{N}\sum_{i=1}^{N}(Xi-\bar{X})4}{\left(\frac{1}{N}\sum_{i=1}^{N}(Xi-\bar{X})2\right)2}$
f6		Variance	Temporal changes in fluorescence intensity	$\frac{1}{N}\sum_{i=1}^{N} Xi(t) - \frac{1}{N}\sum_{i=1}^{N} Xi(t_0)$ [c]
f7	2nd order	Contrast	Local intensity variation within the region of interest	$\sum_{i,j} \lvert i-j\rvert 2p(i,j)$ [d]
f8		Energy	Textural uniformity, local homogeneity	$\sum_{i,j} p(i,j)2$
f9		Gamma-k	Effective optical scatterer number density	PDF: $f(x) = \frac{1}{\Gamma(k)\theta^k} x^{k\,1} e^{-\frac{x}{\theta}}$ [e]
f10		Gamma-θ	Effective optical scatterer size	PDF: $f(x) = \frac{1}{\Gamma(k)\theta^k} x^{k\,1} e^{-\frac{x}{\theta}}$ [e]
f11		Sum of squares: variance	Distribution of neighboring intensity level pairs	$\sum_{i,j}(i-\mu)^2 p(i,j)$ [f]
f12		Entropy	Randomness of local intensity distribution	$-\sum_{i,j} p(i,j)\log(p(i,j))$
f13		Homogeneity	Uniformity of local intensity distribution	$\sum_{i,j} \frac{p(i,j)}{1+(i-j)2}$
f14		Sum average	Relationship between occurrences of pairs with lower intensity values and higher intensity values	$\sum_{i=2}^{2Ng} ip_{x+y}(i)$ [g, h]
f15		Sum entropy	Sum of neighborhood intensity value differences	$-\sum_{i=2}^{2Ng} p_{x+y}(i)\log\{p_{x+y}(i)\}$

f16		Sum variance	Relative smoothness	$\sum_{i=2}^{2Ng} i^2 p_{x+y}(i) - \left(\sum_{i=2}^{2Ng} i p_{x+y}(i)\right)^2$
f17		Difference entropy	Randomness/variability in neighborhood intensity value differences	$-\sum_{i=0}^{Ng-1} p_{x-y}(i) \log\{p_{x-y}(i)\}$ [i]
f18		Difference variance	Heterogeneity of local intensity values	$\sum_{i=0}^{Ng-1} i^2 p_{x-y}(i) - \left(\sum_{i=0}^{Ng-1} i p_{x-y}(i)\right)^2$
f19		Information measure of correlation 1	Correlation between the probability distributions, independency	$\frac{HXY-HXY1}{\max\{HX,HY\}}$ [j-m]
f20		Information measure of correlation 2	Correlation between the probability distributions, uniformity	$\sqrt{1-e^{-2(HXY2-HXY)}}$ [n]
f21		Correlation	Correlation of local intensity values	$\sum_{i,j} \frac{(i-\mu i)(j-\mu j)p(i,j)}{\sigma i \sigma j}$ [o, p]

[a] Xi be the gray level intensity of the ith pixel.

[b] N be the number of pixels within the region of interest, M be the number of pixels within the region of background.

[c] p(i,j) be the normalized co-occurence matrix and equal to $\frac{P(i,j)}{\sum P(i,j)}$, P(i,j) be the co-occurence matrix for an arbitrary δ and θ.

[d] t be the time of interest, and t_0 be the time at global maximum intensity.

[e] T(k) be the gamma function evaluated at k.

[f] μ be the grey level weighted sum of joint probabilities and defined as $\sum_{i=1,j=1}^{Ng} ip(i,j)$.

[g] Ng be the number of discrete intensity levels in the image.

[h] $p_{x+y}(k) = \sum_{i=1}^{Ng}\sum_{j=1}^{Ng} p(i,j)$, where i + j = k, and k = 2, 3, …, 2Ng, be the cross-diagonal probabilities.

[i] $p_{x-y}(k) = \sum_{i=1}^{Ng}\sum_{j=1}^{Ng} p(i,j)$, where |i − j| = k, and k = 0, 1, …, Ng−1 , be the diagonal probabilities.

[j] HX = $-\sum_{i=1}^{Ng} p_x(i) log_2(p_x(i) + \epsilon)$ be the entropy of p_x, $p_x(i) = \sum_{j=1}^{Ng} P(i,j)$ be the marginal row probabilities, ϵ be an arbitrarily small positive number ($\approx 2.2\times10^{-16}$).

[k] HY = $-\sum_{j=1}^{Ng} p_y(j) log_2(p_y(j) + \epsilon)$be the entropy of p_y, $p_y(j) = \sum_{i=1}^{Ng} P(i,j)$be the marginal column probabilities.

[l] HXY = $-\sum_{i=1}^{Ng} \sum_{j=1}^{Ng} p(i,j)\, log_2(p(i,j) + \epsilon)$ be the entropy of p(i,j).

[m] HXY1 = $-\sum_{i=1}^{Ng} \sum_{j=1}^{Ng} p(i,j)\, log_2(p_x(i)p_y(j) + \epsilon)$.

[n] HXY2 = $-\sum_{i=1}^{Ng} \sum_{j=1}^{Ng} p_x(i)p_y(j)\, log_2(p_x(i)p_y(j) + \epsilon)$.

[o] μ_x be the mean gray level intensity of p_x and defined as $\mu_x = \sum_{i=1}^{Ng} p_x(i)i$, μ_y be the mean gray level intensity of p_y and defined as $\mu_y = \sum_{j=1}^{Ng} p_y(j)j$.

[p] σ_x be the standard deviation of p_x, σ_y be the standard deviation of p_y.

Chapter 10

References

[1] Orthopedic Surgery-Global Trends & Opportunities. ResearchAndMarkets.com; 2018.

[2] Dischinger PC, Read KM, Kufera JA, Kerns TJ, Burch CA, Jawed N, et al. Consequences and costs of lower extremity injuries. Annual Proceedings/Association for the Advancement of Automotive Medicine, vol. 48, Association for the Advancement of Automotive Medicine; 2004, p. 339.

[3] Rasmussen TE, Souza JM, Eidt JF. Severe lower extremity injury in the adult patient. Up To Date 2021.

[4] Willhuber GC, Stagnaro J, Petracchi M, Donndorff A, Monzon DG, Bonorino JA, et al. Short-term complication rate following orthopedic surgery in a tertiary care center in Argentina. SICOT J 2018;4.

[5] CDC. Procedure-Associated Module Surgical Site Infections Events. 2023.

[6] Bosse MJ, MacKenzie EJ, Kellam JF, Burgess AR, Webb LX, Swiontkowski MF, et al. An analysis of outcomes of reconstruction or amputation after leg-threatening injuries. New England Journal of Medicine 2002;347:1924–31.

[7] Trampuz A, Zimmerli W. Diagnosis and treatment of infections associated with fracture-fixation devices. Injury 2006;37:S59–66.

[8] Pollak AN, Calhoun JH. Extremity war injuries: state of the art and future directions. Prioritized future research objectives. JAAOS-Journal of the American Academy of Orthopaedic Surgeons 2006;14:S212–4.

[9] Murray CK, Obremskey WT, Hsu JR, Andersen RC, Calhoun JH, Clasper JC, et al. Prevention of infections associated with combat-related extremity injuries. Journal of Trauma and Acute Care Surgery 2011;71:S235–57.

[10] Yun HC, Murray CK, Nelson KJ, Bosse MJ. Infection after orthopaedic trauma: prevention and treatment. J Orthop Trauma 2016;30:S21–6.

[11] Panteli M, Giannoudis P V. Chronic osteomyelitis: what the surgeon needs to know. EFORT Open Rev 2016;1:128–35.

[12] CIERNY III G. A clinical staging system for adult osteomyelitis. Contemp Orthop 1985;10:17–37.

[13] Parsons B, Strauss E. Surgical management of chronic osteomyelitis. The American Journal of Surgery 2004;188:57–66.

[14] Marenzana M, Arnett TR. The key role of the blood supply to bone. Bone Res 2013;1:203–15.

[15] Metsemakers W-J, Morgenstern M, McNally MA, Moriarty TF, McFadyen I, Scarborough M, et al. Fracture-related infection: a consensus on definition from an international expert group. Injury 2018;49:505–10.

[16] Stewart S, Barr S, Engiles J, Hickok NJ, Shapiro IM, Richardson DW, et al. Vancomycin-modified implant surface inhibits biofilm formation and supports bone-healing in an infected osteotomy model in sheep: a proof-of-concept study. J Bone Joint Surg Am 2012;94:1406.

[17] Han X, Demidov V, Wirth D, Byrd B, Davis SC, Gitajn IL, et al. Initial experience of perfusion assessment in a rabbit model of orthopaedic trauma surgery using fluorescent microspheres and hyperspectral imaging cryomacrotome. Clinical Biophotonics II, vol. 12146, SPIE; 2022, p. 44–50.

[18] Wise BT, Connelly D, Rocca M, Mascarenhas D, Huang Y, Maceroli MA, et al. A predictive score for determining risk of surgical site infection after orthopaedic trauma surgery. J Orthop Trauma 2019;33:506–13.

[19] Gitajn IL, Elliott JT, Gunn JR, Ruiz AJ, Henderson ER, Pogue BW, et al. Evaluation of bone perfusion during open orthopedic surgery using quantitative dynamic contrast-enhanced fluorescence imaging. Biomed Opt Express 2020;11:6458–69.

[20] Han X, Demidov V, Vaze VS, Jiang S, Gitajn IL, Elliott JT. Spatial and temporal patterns in dynamic-contrast enhanced intraoperative fluorescence imaging enable classification of bone perfusion in patients undergoing leg amputation. Biomed Opt Express 2022;13:3171–86.

[21] Elliott JT, Jiang S, Pogue BW, Gitajn IL. Bone-specific kinetic model to quantify periosteal and endosteal blood flow using indocyanine green in fluorescence guided orthopedic surgery. J Biophotonics 2019;12:e201800427.

[22] American Academy of Orthopaedic Surgeons. Musculoskeletal injuries report: incidence, risk factors and prevention. 2000.

[23] The American College of Surgeons. National Trauma Data Bank Report . 2002.

[24] The American College of Surgeons. National Trauma Data Bank Report . 2016.

[25] The American College of Surgeons. National Trauma Data Bank Report . 2012.

[26] Johnson BA, Carmack D, Neary M, Tenuta J, Chen J. Operation Iraqi freedom: the Landstuhl regional medical center experience. The Journal of Foot and Ankle Surgery 2005;44:177–83.

[27] Harris AM, Althausen PL, Kellam J, Bosse MJ, Castillo R, Group LEAP (LEAP) S. Complications following limb-threatening lower extremity trauma. J Orthop Trauma 2009;23:1–6.

[28] Rozycki GS, Tremblay LN, Feliciano D V, McClelland WB. Blunt vascular trauma in the extremity: diagnosis, management, and outcome. Journal of Trauma and Acute Care Surgery 2003;55:814–24.

[29] Scott RD. The direct medical costs of healthcare-associated infections in US hospitals and the benefits of prevention 2009.

[30] de Mestral C, Sharma S, Haas B, Gomez D, Nathens AB. A contemporary analysis of the management of the mangled lower extremity. Journal of Trauma and Acute Care Surgery 2013;74:597–603.

[31] Charkes ND, Brookes M, Makler PT. Studies of skeletal tracer kinetics: II. Evaluation of a five-compartment model of [18F] fluoride kinetics in rats. Journal of Nuclear Medicine 1979;20:1150–7.

[32] Gross PM, Heistad DD, Marcus ML. Neurohumoral regulation of blood flow to bones and marrow. American Journal of Physiology-Heart and Circulatory Physiology 1979;237:H440–8.

[33] Wootton R, Reeve J, Veall N. The clinical measurement of skeletal blood flow. Clin Sci Mol Med 1976;50:261–8.

[34] Fujikawa Y, Quinn JM, Sabokbar A, McGee JO, Athanasou NA. The human osteoclast precursor circulates in the monocyte fraction. Endocrinology 1996;137:4058–60.

[35] Mazo IB, von Andrian UH. Adhesion and homing of blood-borne cells in bone marrow microvessels. J Leukoc Biol 1999;66:25–32.

[36] Martin C, Burdon PCE, Bridger G, Gutierrez-Ramos J-C, Williams TJ, Rankin SM. Chemokines acting via CXCR2 and CXCR4 control the release of neutrophils from the bone marrow and their return following senescence. Immunity 2003;19:583–93.

[37] Eghbali-Fatourechi GZ, Lamsam J, Fraser D, Nagel D, Riggs BL, Khosla S. Circulating osteoblast-lineage cells in humans. New England Journal of Medicine 2005;352:1959–66.

[38] Levy BI, Schiffrin EL, Mourad J-J, Agostini D, Vicaut E, Safar ME, et al. Impaired tissue perfusion: a pathology common to hypertension, obesity, and diabetes mellitus. Circulation 2008;118:968–76.

[39] DeLano FA, Schmid-Schönbein GW, Skalak TC, Zweifach BW. Penetration of the systemic blood pressure into the microvasculature of rat skeletal muscle. Microvasc Res 1991;41:92–110.

[40] Fry DE, Marek JM, Langsfeld M. Infection in the ischemic lower extremity. Surgical Clinics of North America 1998;78:465–79.

[41] Garwood ER, Moore D, Ewing C, Hwang ES, Alvarado M, Foster RD, et al. Total skin-sparing mastectomy: complications and local recurrence rates in 2 cohorts of patients. Ann Surg 2009;249:26–32.

[42] Jacobson MD, Pedowitz RA, Oyama BK, Tryon B, Gershuni DH. Muscle functional deficits after tourniquet ischemia. Am J Sports Med 1994;22:372–7.

[43] Gitajn IL, Titus AJ, Tosteson AN, Sprague S, Jeray K, Petrisor B, et al. Deficits in preference-based health-related quality of life after complications associated with tibial fracture. Bone Joint J 2018;100:1227–33.

[44] Kildow BJ, Patel SP, Otero JE, Fehring KA, Curtin BM, Springer BD, et al. Results of irrigation and debridement for PJI with the use of intraosseous antibiotics. Orthopaedic Proceedings, vol. 102, The British Editorial Society of Bone & Joint Surgery; 2020, p. 3.

[45] Son M-S, Lau E, Parvizi J, Mont MA, Bozic KJ, Kurtz S. What are the frequency, associated factors, and mortality of amputation and arthrodesis after a failed infected TKA? Clin Orthop Relat Res 2017;475:2905–13.

[46] Poulsen NR, Mechlenburg I, Søballe K, Lange J. Patient-reported quality of life and hip function after 2-stage revision of chronic periprosthetic hip joint infection: a cross-sectional study. HIP International 2018;28:407–14.

[47] Wang Y-XJ, Griffith JF, Kwok AWL, Leung JCS, Yeung DKW, Ahuja AT, et al. Reduced bone perfusion in proximal femur of subjects with decreased bone mineral density preferentially affects the femoral neck. Bone 2009;45:711–5.

[48] Griffith JF, Yeung DKW, Tsang PH, Choi KC, Kwok TCY, Ahuja AT, et al. Compromised bone marrow perfusion in osteoporosis. Journal of Bone and Mineral Research 2008;23:1068–75.

[49] Lee JH, Dyke JP, Ballon D, Ciombor DM, Rosenwasser MP, Aaron RK. Subchondral fluid dynamics in a model of osteoarthritis: use of dynamic contrast-enhanced magnetic resonance imaging. Osteoarthritis Cartilage 2009;17:1350–5.

[50] Chen J, Hendriks M, Chatzis A, Ramasamy SK, Kusumbe AP. Bone vasculature and bone marrow vascular niches in health and disease. Journal of Bone and Mineral Research 2020;35:2103–20.

[51] Sinha B, François PP, Nüße O, Foti M, Hartford OM, Vaudaux P, et al. Fibronectin-binding protein acts as Staphylococcus aureus invasin via fibronectin bridging to integrin α5β1. Cell Microbiol 1999;1:101–17.

[52] Costerton W, Veeh R, Shirtliff M, Pasmore M, Post C, Ehrlich G. The application of biofilm science to the study and control of chronic bacterial infections. J Clin Invest 2003;112:1466–77.

[53] Stewart PS. Mechanisms of antibiotic resistance in bacterial biofilms. International Journal of Medical Microbiology 2002;292:107–13.

[54] Jauregui LE, Senour CL. Chronic osteomyelitis. INFECTIOUS DISEASE AND THERAPY SERIES 1995;16:37.

[55] Caputo GM, Cavanagh PR, Ulbrecht JS, Gibbons GW, Karchmer AW. Assessment and management of foot disease in patients with diabetes. New England Journal of Medicine 1994;331:854–60.

[56] Lew DP, Waldvogel FA. Osteomyelitis. The Lancet 2004;364:369–79.

[57] Dyke JP, Aaron RK. Noninvasive methods of measuring bone blood perfusion. Ann N Y Acad Sci 2010;1192:95–102.

[58] Dymling SO, Persson HW, Hertz CH. Measurement of blood perfusion in tissue using Doppler ultrasound. Ultrasound Med Biol 1991;17:433–44.

[59] Niclauss L. Techniques and standards in intraoperative graft verification by transit time flow measurement after coronary artery bypass graft surgery: a critical review. European Journal of Cardio-Thoracic Surgery 2017;51:26–33. https://doi.org/10.1093/ejcts/ezw203.

[60] Hasanin A, Mukhtar A, Nassar H. Perfusion indices revisited. J Intensive Care 2017;5:1–8.

[61] Dyke JP, Aaron RK. Noninvasive methods of measuring bone blood perfusion 2010. https://doi.org/10.1111/j.1749-6632.2009.05376.x.

[62] Weissleder R, Pittet MJ. Imaging in the era of molecular oncology. Nature 2008;452:580–9.

[63] Resnick D, Niwayama G. Diagnosis of bone and joint disorders 1987.

[64] Bassett LW, Gold RH, Reicher M, Bennett LR, Tooke SM. Magnetic resonance imaging in the early diagnosis of ischemic necrosis of the femoral head. Preliminary results. Clin Orthop Relat Res 1987:237–48.

[65] Beltran J, Herman LJ, Burk JM, Zuelzer WA, Clark RN, Lucas JG, et al. Femoral head avascular necrosis: MR imaging with clinical-pathologic and radionuclide correlation. Radiology 1988;166:215–20.

[66] Collier BD, Carrera GF, Johnson RP, Isitman AT, Hellman RS, Knobel J, et al. Detection of femoral head avascular necrosis in adults by SPECT. Journal of Nuclear Medicine 1985;26:979–87.

[67] Lee MH, Moon DH, Ryu JS, Na HW, Lee SH, Kim KY. Diagnosis of femoral head avascular necrosis by triple head high resolution SPECT. 대한핵의학회 학술대회 1992:1812.

[68] Lee MJ, Corrigan J, Stack JP, Ennis JT. A comparison of modern imaging modalities in osteonecrosis of the femoral head. Clin Radiol 1990;42:427–32.

[69] Sarikaya I, Sarikaya A, Holder LE. The role of single photon emission computed tomography in bone imaging. Semin Nucl Med 2001;31:3–16. https://doi.org/https://doi.org/10.1053/snuc.2001.18736.

[70] Naito M, Ogata K, Moriguchi H. Quantitative bone scanning of the hip. Int Orthop 1996;20:311–4.

[71] Wehrli FW. Structural and functional assessment of trabecular and cortical bone by micro magnetic resonance imaging. Journal of Magnetic Resonance Imaging: An Official Journal of the International Society for Magnetic Resonance in Medicine 2007;25:390–409.

[72] Grant FD, Fahey FH, Packard AB, Davis RT, Alavi A, Treves ST. Skeletal PET with 18F-fluoride: applying new technology to an old tracer. Journal of Nuclear Medicine 2008;49:68–78.

[73] Fox IJ. History and developmental aspects of the indicator-dilution technic. Circ Res 1962;10:381–92.

[74] Jhanji S, Dawson J, Pearse RM. Cardiac output monitoring: basic science and clinical application. Anaesthesia 2008;63:172–81.

[75] Kety SS, Schmidt CF. The determination of cerebral blood flow in man by the use of nitrous oxide in low concentrations. American Journal of Physiology-Legacy Content 1945;143:53–66.

[76] Lassen NA, Munck O. The cerebral blood flow in man determined by the use of radioactive krypton. Acta Physiol Scand 1955;33:30–49.

[77] Obrist WD, Thompson Jr HK, KING H, Wang HS. Determination of regional cerebral blood flow by inhalation of 133-xenon. Circ Res 1967;20:124–35.

[78] Zierler K. Indicator dilution methods for measuring blood flow, volume, and other properties of biological systems: a brief history and memoir. Ann Biomed Eng 2000;28:836–48.

[79] Barrett T, Choyke PL. Imaging of angiogenesis. Angiogenesis, Springer; 2008, p. 321–32.

[80] Loveless ME, Yankeelov TE. Dynamic contrast enhanced MRI: data acquisition and analysis. Quantitative MRI in Cancer 2011;144.

[81] Gribbestad IS, Gjesdal KI, Nilsen G, Lundgren S, Hjelstuen MHB, Jackson A. An introduction to dynamic contrast-enhanced MRI in oncology. Dynamic contrast-enhanced magnetic resonance imaging in oncology, Springer; 2005, p. 1–22.

[82] Frackowiak R, Lenzi G-L, Jones T, Heather JD. Quantitative measurement of regional cerebral blood flow and oxygen metabolism in man using 15O and positron emission tomography: theory, procedure, and normal values. J Comput Assist Tomogr 1980;4:727–36.

[83] Axel L. Cerebral blood flow determination by rapid-sequence computed tomography: theoretical analysis. Radiology 1980;137:679–86.

[84] Fletcher BD, Hanna SL, Fairclough DL, Gronemeyer SA. Pediatric musculoskeletal tumors: use of dynamic, contrast-enhanced MR imaging to monitor response to chemotherapy. Radiology 1992;184:243–8.

[85] Yankeelov TE, Gore JC. Dynamic contrast enhanced magnetic resonance imaging in oncology: theory, data acquisition, analysis, and examples. Curr Med Imaging 2007;3:91–107.

[86] Jackson A, O'Connor JPB, Parker GJM, Jayson GC. Imaging tumor vascular heterogeneity and angiogenesis using dynamic contrast-enhanced magnetic resonance imaging. Clinical Cancer Research 2007;13:3449–59.

[87] Furman-Haran E, Schechtman E, Kelcz F, Kirshenbaum K, Degani H. Magnetic resonance imaging reveals functional diversity of the vasculature in benign and malignant breast lesions. Cancer 2005;104:708–18.

[88] Cha S, Knopp EA, Johnson G, Wetzel SG, Litt AW, Zagzag D. Intracranial mass lesions: dynamic contrast-enhanced susceptibility-weighted echo-planar perfusion MR imaging. Radiology 2002;223:11–29.

[89] Dietrich CF, Averkiou MA, Correas J-M, Lassau N, Leen E, Piscaglia F. An EFSUMB introduction into Dynamic Contrast-Enhanced Ultrasound (DCE-US) for quantification of tumour perfusion. Ultraschall in Der Medizin-European Journal of Ultrasound 2012;33:344–51.

[90] Tofts PS, Brix G, Buckley DL, Evelhoch JL, Henderson E, Knopp M V, et al. Estimating kinetic parameters from dynamic contrast-enhanced T1-weighted MRI of a diffusable tracer: standardized quantities and symbols. Journal of Magnetic Resonance Imaging: An Official Journal of the International Society for Magnetic Resonance in Medicine 1999;10:223–32.

[91] Choyke PL, Dwyer AJ, Knopp M V. Functional tumor imaging with dynamic contrast-enhanced magnetic resonance imaging. Journal of Magnetic Resonance Imaging: An Official Journal of the International Society for Magnetic Resonance in Medicine 2003;17:509–20.

[92] Feinstein SB, Coll B, Staub D, Adam D, Schinkel AFL, Ten Cate FJ, et al. Contrast enhanced ultrasound imaging. Journal of Nuclear Cardiology 2010;17:106–15.

[93] Abdelmoneim SS, Bernier M, Scott CG, Dhoble A, Ness SAC, Hagen ME, et al. Safety of contrast agent use during stress echocardiography: a 4-year experience from a single-center cohort study of 26,774 patients. JACC Cardiovasc Imaging 2009;2:1048–56.

[94] Burtea C, Laurent S, Vander Elst L, Muller RN. Contrast Agents: Magnetic Resonance. In: Semmler W, Schwaiger M, editors. Molecular Imaging I, Berlin, Heidelberg: Springer Berlin Heidelberg; 2008, p. 135–65. https://doi.org/10.1007/978-3-540-72718-7_7.

[95] Hasebroock KM, Serkova NJ. Toxicity of MRI and CT contrast agents. Expert Opin Drug Metab Toxicol 2009;5:403–16.

[96] Turco S, Wijkstra H, Mischi M. Mathematical models of contrast transport kinetics for cancer diagnostic imaging: a review. IEEE Rev Biomed Eng 2016;9:121–47.

[97] Valerio I, Green III JM, Sacks JM, Thomas S, Sabino J, Acarturk TO. Vascularized osseous flaps and assessing their bipartate perfusion pattern via intraoperative fluorescence angiography. J Reconstr Microsurg 2015;31:45–53.

[98] Miles K, Charnsangavej C, Cuenod C. Perfusion CT–PET: opportunities for combined. Multi-Detector Computed Tomography in Oncology, CRC Press; 2007, p. 231–46.

[99] Weissleder R, Tung C-H, Mahmood U, Bogdanov A. In vivo imaging of tumors with protease-activated near-infrared fluorescent probes. Nat Biotechnol 1999;17:375–8.

[100] Choi HS, Gibbs SL, Lee JH, Kim SH, Ashitate Y, Liu F, et al. Targeted zwitterionic near-infrared fluorophores for improved optical imaging. Nat Biotechnol 2013;31:148–53.

[101] Olson ES, Jiang T, Aguilera TA, Nguyen QT, Ellies LG, Scadeng M, et al. Activatable cell penetrating peptides linked to nanoparticles as dual probes for in vivo fluorescence and MR imaging of proteases. Proceedings of the National Academy of Sciences 2010;107:4311–6.

[102] Ohnishi S, Lomnes SJ, Laurence RG, Gogbashian A, Mariani G, Frangioni J V. Organic alternatives to quantum dots for intraoperative near-infrared fluorescent sentinel lymph node mapping. Mol Imaging 2005;4:15353500200505128.

[103] Emerson DK, Limmer KK, Hall DJ, Han S-H, Eckelman WC, Kane CJ, et al. A receptor-targeted fluorescent radiopharmaceutical for multireporter sentinel lymph node imaging. Radiology 2012;265:186–93.

[104] Brouwer OR, Klop WMC, Buckle T, Vermeeren L, Van Den Brekel MWM, Balm AJM, et al. Feasibility of sentinel node biopsy in head and neck melanoma using a hybrid radioactive and fluorescent tracer. Ann Surg Oncol 2012;19:1988–94.

[105] Hyde D, de Kleine R, MacLaurin SA, Miller E, Brooks DH, Krucker T, et al. Hybrid FMT–CT imaging of amyloid-β plaques in a murine Alzheimer's disease model. Neuroimage 2009;44:1304–11.

[106] Pham W, Zhao B-Q, Lo EH, Medarova Z, Rosen B, Moore A. Crossing the blood–brain barrier: a potential application of myristoylated polyarginine for in vivo neuroimaging. Neuroimage 2005;28:287–92.

[107] Deguchi J, Aikawa M, Tung C-H, Aikawa E, Kim D-E, Ntziachristos V, et al. Inflammation in atherosclerosis: visualizing matrix metalloproteinase action in macrophages in vivo. Circulation 2006;114:55–62.

[108] Sosnovik DE, Nahrendorf M, Deliolanis N, Novikov M, Aikawa E, Josephson L, et al. Fluorescence tomography and magnetic resonance imaging of myocardial macrophage infiltration in infarcted myocardium in vivo. Circulation 2007;115:1384–91.

[109] Wunder A, Tung C, Müller-Ladner U, Weissleder R, Mahmood U. In vivo imaging of protease activity in arthritis: a novel approach for monitoring treatment response. Arthritis & Rheumatism: Official Journal of the American College of Rheumatology 2004;50:2459–65.

[110] Choi HS, Nasr K, Alyabyev S, Feith D, Lee JH, Kim SH, et al. Synthesis and in vivo fate of zwitterionic near-infrared fluorophores. Angewandte Chemie International Edition 2011;50:6258–63.

[111] Figueiredo J-L, Siegel C, Nahrendorf M, Weissleder R. Intraoperative near-infrared fluorescent cholangiography (NIRFC) in mouse models of bile duct injury. World J Surg 2010;34:336–43.

[112] Vahrmeijer AL, Hutteman M, Van Der Vorst JR, Van De Velde CJH, Frangioni J V. Image-guided cancer surgery using near-infrared fluorescence. Nat Rev Clin Oncol 2013;10:507–18.

[113] Dengel LT, More MJ, Judy PG, Petroni GR, Smolkin ME, Rehm PK, et al. Intraoperative imaging guidance for sentinel node biopsy in melanoma using a mobile gamma camera. Ann Surg 2011;253:774.

[114] Brouwer OR, Buckle T, Vermeeren L, Klop WMC, Balm AJM, van der Poel HG, et al. Comparing the hybrid fluorescent–radioactive tracer indocyanine green–

99mTc-nanocolloid with 99mTc-nanocolloid for sentinel node identification: a validation study using lymphoscintigraphy and SPECT/CT. Journal of Nuclear Medicine 2012;53:1034–40.

[115] Meier P, Zierler KL. On the theory of the indicator-dilution method for measurement of blood flow and volume. J Appl Physiol 1954;6:731–44.

[116] Tofts PS. Modeling tracer kinetics in dynamic Gd-DTPA MR imaging. Journal of Magnetic Resonance Imaging 1997;7:91–101.

[117] Lawrence KSS, Lee T-Y. An adiabatic approximation to the tissue homogeneity model for water exchange in the brain: I. Theoretical derivation. Journal of Cerebral Blood Flow & Metabolism 1998;18:1365–77.

[118] Lawrence KSS, Lee T-Y. An adiabatic approximation to the tissue homogeneity model for water exchange in the brain: II. Experimental validation. Journal of Cerebral Blood Flow & Metabolism 1998;18:1378–85.

[119] Morales MF, Smith RE. On the theory of blood-tissue exchange of inert gases: VI. Validity of approximate uptake expressions. Bull Math Biophys 1948;10:191–200.

[120] Schabel MC. A unified impulse response model for DCE-MRI. Magn Reson Med 2012;68:1632–46.

[121] Aaron RK, Dyke JP, Ciombor DM, Ballon D, Lee J, Jung E, et al. Perfusion abnormalities in subchondral bone associated with marrow edema, osteoarthritis, and avascular necrosis. Ann N Y Acad Sci 2007;1117:124–37.

[122] Boraiah S, Dyke JP, Hettrich C, Parker RJ, Miller A, Helfet D, et al. Assessment of vascularity of the femoral head using gadolinium (Gd-DTPA)-enhanced magnetic resonance imaging: a cadaver study. J Bone Joint Surg Br 2009;91:131–7.

[123] van Dijke CF, Peterfy CG, Brasch RC, Lang P, Roberts TPL, Shames D, et al. MR imaging of the arthritic rabbit knee joint using albumin-(Gd-DTPA) 30 with correlation to histopathology. Magn Reson Imaging 1999;17:237–45.

[124] Van Dijke CF, Kirk BA, Peterfy CG, Genant HK, Brasch RC, Kapila S. Arthritic temporomandibular joint: correlation of macromolecular contrast-enhanced MR imaging parameters and histopathologic findings. Radiology 1997;204:825–32.

[125] Hawkins RA, Choi Y, Huang S-C, Hoh CK, Dahlbom M, Schiepers C, et al. Evaluation of the skeletal kinetics of fluorine-18-fluoride ion with PET. Journal of Nuclear Medicine 1992;33:633–42.

[126] Piert M, Zittel TT, Becker GA, Jahn M, Stahlschmidt A, Maier G, et al. Assessment of porcine bone metabolism by dynamic [18F] fluoride ion PET: correlation with bone histomorphometry. Journal of Nuclear Medicine 2001;42:1091–100.

[127] Piert M, Winter E, Becker GA, Bilger K, Machulla H-J, Müller-Schauenburg W, et al. Allogenic bone graft viability after hip revision arthroplasty assessed by dynamic [18 F] fluoride ion positron emission tomography. Eur J Nucl Med 1999;26:615–24.

[128] Elliott JT, Addante RR, Slobogean GP, Jiang S, Henderson ER, Pogue BW, et al. Intraoperative fluorescence perfusion assessment should be corrected by a measured subject-specific arterial input function. J Biomed Opt 2020;25:066002.

[129] Stodilka RZ, Lewden B, Jerosch-Herold M, Sabondjian E, Prato FS. Examination of Contrast Agents in Medical Imaging Using Physiologically-Constrained Deconvolution. Advanced Signal Processing, CRC Press; 2017, p. 641–52.

[130] RUDOLPH AM, HEYMANN MA. The Circulation of the Fetus in Utero. Circ Res 1967;21:163–84. https://doi.org/10.1161/01.RES.21.2.163.

[131] Domenech RJ, Hoffman JI, Noble MI, SAUNDERS KB, HENSON JR, SUBIJANTO S. Total and regional coronary blood flow measured by radioactive microspheres in conscious and anesthetized dogs. Circ Res 1969;25:581–96.

[132] Buckberg GD, Luck JC, Payne DB, Hoffman JI, Archie JP, Fixler DE. Some sources of error in measuring regional blood flow with radioactive microspheres. J Appl Physiol 1971;31:598–604.

[133] Bassingthwaighte JB, Malone MA, Moffett TC, King RB, Little SE, Link JM, et al. Validity of microsphere depositions for regional myocardial flows. American Journal of Physiology-Heart and Circulatory Physiology 1987;253:H184–93.

[134] Glenny RW, Bernard S, Brinkley M. Validation of fluorescent-labeled microspheres for measurement of regional organ perfusion. J Appl Physiol 1993;74:2585–97.

[135] Van Oosterhout MFM, Prinzen FW, Sakurada S, Glenny RW, Hales JRS. Fluorescent microspheres are superior to radioactive microspheres in chronic blood flow measurements. American Journal of Physiology-Heart and Circulatory Physiology 1998;275:H110–5.

[136] Heymann MA, Payne BD, Hoffman JIE, Rudolph AM. Blood flow measurements with radionuclide-labeled particles. Prog Cardiovasc Dis 1977;20:55–79.

[137] Hale SL, Alker KJ, Kloner RA. Evaluation of nonradioactive, colored microspheres for measurement of regional myocardial blood flow in dogs. Circulation 1988;78:428–34.

[138] Quintana A, Raczka E, Bonaccorsi A. Cardiac output distribution measured with radioactive microspheres in the mouse. Pharmacol Res Commun 1979;11:245–52.

[139] Cenic A, Nabavi DG, Craen RA, Gelb AW, Lee T-Y. Dynamic CT measurement of cerebral blood flow: a validation study. American Journal of Neuroradiology 1999;20:63–73.

[140] Schimmel C, Frazer D, Glenny RW. Extending fluorescent microsphere methods for regional organ blood flow to 13 simultaneous colors. American Journal of Physiology-Heart and Circulatory Physiology 2001;280:H2496–506.

[141] Tan W, Riggs KW, Thies RL, Rurak DW. Use of an automated fluorescent microsphere method to measure regional blood flow in the fetal lamb. Can J Physiol Pharmacol 1997;75:959–68.

[142] Anetzberger H, Thein E, Becker M, Zwissler B, Messmer K. Microspheres accurately predict regional bone blood flow. Clinical Orthopaedics and Related Research (1976-2007) 2004;424:253–65.

[143] Anetzberger H, Thein E, Maier M, Birkenmaier C, Messmer K. Fluorescent microspheres are reliable for serial bone blood flow measurements. Clinical Orthopaedics and Related Research (1976-2007) 2004;427:241–8.

[144] Hu Q, Nelson TJ, Seymour RS. Regional femoral bone blood flow rates in laying and non-laying chickens estimated with fluorescent microspheres. Journal of Experimental Biology 2021;224:jeb242597.

[145] Serrat MA. Measuring bone blood supply in mice using fluorescent microspheres. Nat Protoc 2009;4:1749–58.

[146] Anetzberger H, Thein E, Loffler G, Messmer K. Fluorescent microsphere method is suitable for chronic bone blood flow measurement: a long-term study after meniscectomy in rabbits. J Appl Physiol 2004;96:1928–36.

[147] Aref MW, Akans E, Allen MR. Assessment of regional bone tissue perfusion in rats using fluorescent microspheres. Bone Rep 2017;6:140–4.

[148] Kelly JJ, Ewen JR, Bernard SL, Glenny RW, Barlow CH. Regional blood flow measurements from fluorescent microsphere images using an Imaging CryoMicrotome. Review of Scientific Instruments 2000;71:228–34.

[149] Bernard SL, Ewen JR, Barlow CH, Kelly JJ, McKinney S, Frazer DA, et al. High spatial resolution measurements of organ blood flow in small laboratory animals. American Journal of Physiology-Heart and Circulatory Physiology 2000;279:H2043–52.

[150] Wirth D, Byrd B, Meng B, Strawbridge RR, Samkoe KS, Davis SC. Hyperspectral imaging and spectral unmixing for improving whole-body fluorescence cryo-imaging. Biomed Opt Express 2021;12:395–408.

[151] Jacques SL, Pogue BW. Tutorial on diffuse light transport. J Biomed Opt 2008;13:041302.

[152] Gioux S, Choi HS, Frangioni J V. Image-guided surgery using invisible near-infrared light: fundamentals of clinical translation. Mol Imaging 2010;9:2010–7290.

[153] Flower RW. Extraction of choriocapillaris hemodynamic data from ICG fluorescence angiograms. Invest Ophthalmol Vis Sci 1993;34:2720–9.

[154] Miwa M. Photodynamic Characteristics of ICG Fluorescence Imaging. ICG Fluorescence Imaging and Navigation Surgery, Springer; 2016, p. 3–7.

[155] Bashkatov AN, Genina EA, Kochubey VI, Tuchin V V. Optical properties of human cranial bone in the spectral range from 800 to 2000 nm. Saratov Fall Meeting 2005: Optical Technologies in Biophysics and Medicine VII, vol. 6163, SPIE; 2006, p. 306–16.

[156] Firbank M, Hiraoka M, Essenpreis M, Delpy DT. Measurement of the optical properties of the skull in the wavelength range 650-950 nm. Phys Med Biol 1993;38:503.

[157] Bevilacqua F, Piguet D, Marquet P, Gross JD, Tromberg BJ, Depeursinge C. In vivo local determination of tissue optical properties: applications to human brain. Appl Opt 1999;38:4939–50.

[158] Tauber S, Baumgartner R, Schorn K, Beyer W. Lightdosimetric quantitative analysis of the human petrous bone: Experimental study for laser irradiation of the cochlea. Lasers in Surgery and Medicine: The Official Journal of the American Society for Laser Medicine and Surgery 2001;28:18–26.

[159] Pifferi A, Torricelli A, Taroni P, Bassi AL, Chikoidze E, Giambattistelli E, et al. Optical biopsy of bone tissue: a step toward the diagnosis of bone pathologies. J Biomed Opt 2004;9:474–80.

[160] Rossi VM, Gustafson SB, Jacques SL. Characterizing light propagation in bone for photodynamic therapy of osteosarcoma. Optics in Bone Biology and Diagnostics, vol. 7166, SPIE; 2009, p. 140–51.

[161] Frangioni J V. In vivo near-infrared fluorescence imaging. Curr Opin Chem Biol 2003;7:626–34.

[162] Hwang K, Houston JP, Rasmussen JC, Joshi A, Ke S, Li C, et al. Improved excitation light rejection enhances small-animal fluorescent optical imaging. Mol Imaging 2005;4:15353500200505142.

[163] Sexton K, Davis SC, McClatchy D, Valdes PA, Kanick SC, Paulsen KD, et al. Pulsed-light imaging for fluorescence guided surgery under normal room lighting. Opt Lett 2013;38:3249–52.

[164] Tauber S, Stepp H, Meier R, Bone A, Hofstetter A, Stief C. Integral spectrophotometric analysis of 5-aminolaevulinic acid-induced fluorescence cytology of the urinary bladder. BJU Int 2006;97:992–6.

[165] Tunnell JW, Desjardins AE, Galindo L, Georgakoudi I, McGee SA, Mirkovic J, et al. Instrumentation for multi-modal spectroscopic diagnosis of epithelial dysplasia. Technol Cancer Res Treat 2003;2:505–14.

[166] Cardenas-Turanzas M, Freeberg JA, Benedet JL, Atkinson EN, Cox DD, Richards-Kortum R, et al. The clinical effectiveness of optical spectroscopy for the in vivo diagnosis of cervical intraepithelial neoplasia: where are we? Gynecol Oncol 2007;107:S138–46.

[167] DaCosta RS, Wilson BC, Marcon NE. Fluorescence and spectral imaging. ScientificWorldJournal 2007;7:2046–71.

[168] Comelli D, Valentini G, Nevin A, Farina A, Toniolo L, Cubeddu R. A portable UV-fluorescence multispectral imaging system for the analysis of painted surfaces. Review of Scientific Instruments 2008;79:086112.

[169] DSouza A V, Lin H, Gunn JR, Pogue BW. Logarithmic intensity compression in fluorescence guided surgery applications. J Biomed Opt 2015;20:080504.

[170] Samkoe KS, Tichauer KM, Gunn JR, Wells WA, Hasan T, Pogue BW. Quantitative In Vivo Immunohistochemistry of Epidermal Growth Factor Receptor Using a Receptor Concentration Imaging ApproachQuantitative In Vivo Immunohistochemistry of EGFR. Cancer Res 2014;74:7465–74.

[171] Tichauer KM, Samkoe KS, Sexton KJ, Hextrum SK, Yang HH, Klubben WS, et al. In vivo quantification of tumor receptor binding potential with dual-reporter molecular imaging. Mol Imaging Biol 2012;14:584–92.

[172] Tichauer KM, Wang Y, Pogue BW, Liu JTC. Quantitative in vivo cell-surface receptor imaging in oncology: kinetic modeling and paired-agent principles from nuclear medicine and optical imaging. Phys Med Biol 2015;60:R239.

[173] Xu L, Su H, Sun G-R, Wang Y, Guo S, Zhang X, et al. Fluorescein-labeled “arch-like” DNA probes for electrochemical detection of DNA on gold nanoparticle-modified gold electrodes. J Biotechnol 2013;168:388–93.

[174] Tsujimoto H, Morimoto Y, Takahata R, Nomura S, Yoshida K, Horiguchi H, et al. Photodynamic therapy using nanoparticle loaded with indocyanine green for experimental peritoneal dissemination of gastric cancer. Cancer Sci 2014;105:1626–30.

[175] Navarro FP, Berger M, Guillermet S, Josserand V, Guyon L, Neumann E, et al. Lipid nanoparticle vectorization of indocyanine green improves fluorescence imaging for tumor diagnosis and lymph node resection. J Biomed Nanotechnol 2012;8:730–41.

[176] Watanabe R, Sato K, Hanaoka H, Harada T, Nakajima T, Kim I, et al. Minibody-indocyanine green based activatable optical imaging probes: the role of short polyethylene glycol linkers. ACS Med Chem Lett 2014;5:411–5.

[177] Sano K, Nakajima T, Ali T, Bartlett DW, Wu AM, Kim I, et al. Activatable fluorescent cys-diabody conjugated with indocyanine green derivative: consideration of fluorescent catabolite kinetics on molecular imaging. J Biomed Opt 2013;18:101304.

[178] Olafsen T, Wu AM. Antibody vectors for imaging. Semin Nucl Med, vol. 40, Elsevier; 2010, p. 167–81.

[179] Ahmed TAAE-TA. Pharmacokinetics of Drugs Following IV Bolus, IV Infusion, and Oral Administration. Basic Pharmacokinetic Concepts and Some Clinical Applications, Rijeka: IntechOpen; 2015, p. Ch. 3. https://doi.org/10.5772/61573.

[180] Orton MR, d'Arcy JA, Walker-Samuel S, Hawkes DJ, Atkinson D, Collins DJ, et al. Computationally efficient vascular input function models for quantitative kinetic modelling using DCE-MRI. Phys Med Biol 2008;53:1225.

[181] Tofts PS, Berkowitz B, Schnall MD. Quantitative analysis of dynamic Gd-DTPA enhancement in breast tumors using a permeability model. Magn Reson Med 1995;33:564–8.

[182] Tofts PS, Kermode AG. Measurement of the blood-brain barrier permeability and leakage space using dynamic MR imaging. 1. Fundamental concepts. Magn Reson Med 1991;17:357–67.

[183] Ingrisch M, Sourbron S. Tracer-kinetic modeling of dynamic contrast-enhanced MRI and CT: a primer. J Pharmacokinet Pharmacodyn 2013;40:281–300.

[184] Parker GJM, Roberts C, Macdonald A, Buonaccorsi GA, Cheung S, Buckley DL, et al. Experimentally-derived functional form for a population-averaged high-temporal-resolution arterial input function for dynamic contrast-enhanced MRI. Magnetic Resonance in Medicine: An Official Journal of the International Society for Magnetic Resonance in Medicine 2006;56:993–1000.

[185] Yankeelov TE, Luci JJ, Lepage M, Li R, Debusk L, Lin PC, et al. Quantitative pharmacokinetic analysis of DCE-MRI data without an arterial input function: a reference region model. Magn Reson Imaging 2005;23:519–29. https://doi.org/https://doi.org/10.1016/j.mri.2005.02.013.

[186] Iijima T, Iwao Y, Sankawa H. Circulating Blood Volume Measured by Pulse Dye-Densitometry: Comparison with131I-HSA Analysis. The Journal of the American Society of Anesthesiologists 1998;89:1329–35.

[187] He L, Baker WB, Milej D, Kavuri VC, Mesquita RC, Busch DR, et al. Noninvasive continuous optical monitoring of absolute cerebral blood flow in critically ill adults. Neurophotonics 2018;5:045006.

[188] Cobelli C, Carson E. Introduction to modeling in physiology and medicine. Academic Press; 2019.

[189] Jackson A, Buckley DL, Parker GJM. Dynamic contrast-enhanced magnetic resonance imaging in oncology. vol. 12. Springer; 2005.

[190] Schoepf UJ, Costello P. CT angiography for diagnosis of pulmonary embolism: state of the art. Radiology 2004;230:329–37.

[191] Roblot V, Giret Y, Antoun MB, Morillot C, Chassin X, Cotten A, et al. Artificial intelligence to diagnose meniscus tears on MRI. Diagn Interv Imaging 2019;100:243–9.

[192] Chan H, Lo SB, Sahiner B, Lam KL, Helvie MA. Computer-aided detection of mammographic microcalcifications: Pattern recognition with an artificial neural network. Med Phys 1995;22:1555–67.

[193] Bauer S, Wiest R, Nolte L-P, Reyes M. A survey of MRI-based medical image analysis for brain tumor studies. Phys Med Biol 2013;58:R97.

[194] Couteaux V, Si-Mohamed S, Nempont O, Lefevre T, Popoff A, Pizaine G, et al. Automatic knee meniscus tear detection and orientation classification with Mask-RCNN. Diagn Interv Imaging 2019;100:235–42.

[195] Mitchell TM, Shinkareva S V, Carlson A, Chang K-M, Malave VL, Mason RA, et al. Predicting human brain activity associated with the meanings of nouns. Science (1979) 2008;320:1191–5.

[196] Davatzikos C, Fan Y, Wu X, Shen D, Resnick SM. Detection of prodromal Alzheimer's disease via pattern classification of magnetic resonance imaging. Neurobiol Aging 2008;29:514–23.

[197] Kim D, Burge J, Lane T, Pearlson GD, Kiehl KA, Calhoun VD. Hybrid ICA–Bayesian network approach reveals distinct effective connectivity differences in schizophrenia. Neuroimage 2008;42:1560–8.

[198] Breiman L, Friedman JH, Olshen RA, Stone CJ. Classification and regression trees. Routledge; 2017.

[199] Harper PR. A review and comparison of classification algorithms for medical decision making. Health Policy (New York) 2005;71:315–31.

[200] Boussion N, Cheze Le Rest C, Hatt M, Visvikis D. Incorporation of wavelet-based denoising in iterative deconvolution for partial volume correction in whole-body PET imaging. Eur J Nucl Med Mol Imaging 2009;36:1064–75.

[201] Caicedo JC, Cooper S, Heigwer F, Warchal S, Qiu P, Molnar C, et al. Data-analysis strategies for image-based cell profiling. Nat Methods 2017;14:849–63.

[202] Gjesteby L, De Man B, Jin Y, Paganetti H, Verburg J, Giantsoudi D, et al. Metal artifact reduction in CT: where are we after four decades? Ieee Access 2016;4:5826–49.

[203] Sled JG, Zijdenbos AP, Evans AC. A nonparametric method for automatic correction of intensity nonuniformity in MRI data. IEEE Trans Med Imaging 1998;17:87–97.

[204] Smith K, Li Y, Piccinini F, Csucs G, Balazs C, Bevilacqua A, et al. CIDRE: an illumination-correction method for optical microscopy. Nat Methods 2015;12:404–6.

[205] Haralick RM, Shapiro LG. Image segmentation techniques. Comput Vis Graph Image Process 1985;29:100–32.

[206] Gonzalez RC. Digital image processing. Pearson education india; 2009.

[207] Pal NR, Pal SK. A review on image segmentation techniques. Pattern Recognit 1993;26:1277–94.

[208] Pham DL, Xu C, Prince JL. Current methods in medical image segmentation. Annu Rev Biomed Eng 2000;2:315–37.

[209] Zwanenburg A, Vallières M, Abdalah MA, Aerts HJWL, Andrearczyk V, Apte A, et al. The image biomarker standardization initiative: standardized quantitative radiomics for high-throughput image-based phenotyping. Radiology 2020;295:328–38.

[210] Gillies RJ, Kinahan PE, Hricak H. Radiomics: images are more than pictures, they are data. Radiology 2016;278:563.

[211] Haralick RM, Shanmugam K, Dinstein IH. Textural features for image classification. IEEE Trans Syst Man Cybern 1973:610–21.

[212] Grossmann P, Grove O, El-Hachem N. Identification of molecular phenotypes in lung cancer by integrating radiomics and genomics. Sci Transl Med n.d.

[213] Larkin TJ, Canuto HC, Kettunen MI, Booth TC, Hu D, Krishnan AS, et al. Analysis of image heterogeneity using 2D Minkowski functionals detects tumor responses to treatment. Magn Reson Med 2014;71:402–10.

[214] Burian E, Subburaj K, Mookiah MRK, Rohrmeier A, Hedderich DM, Dieckmeyer M, et al. Texture analysis of vertebral bone marrow using chemical shift encoding–based water-fat MRI: a feasibility study. Osteoporosis International 2019;30:1265–74.

[215] de Sá Cavalcante D, da Silva Castro MG, Quidute ARP, Martins MRA, Cid AMPL, de Barros Silva PG, et al. Evaluation of bone texture imaging parameters on panoramic radiographs of patients with Sheehan's syndrome: a STROBE-compliant case-control study. Osteoporosis International 2019;30:2257–69.

[216] Kawashima Y, Fujita A, Buch K, Li B, Qureshi MM, Chapman MN, et al. Using texture analysis of head CT images to differentiate osteoporosis from normal bone density. Eur J Radiol 2019;116:212–8.

[217] Valentinitsch A, Trebeschi S, Kaesmacher J, Lorenz C, Löffler MT, Zimmer C, et al. Opportunistic osteoporosis screening in multi-detector CT images via local classification of textures. Osteoporosis International 2019;30:1275–85.

[218] White R, Krueger D, De Guio F, Michelet F, Hans D, Anderson P, et al. An exploratory study of the texture research investigational platform (TRIP) to evaluate bone texture score of distal femur DXA scans–a TBS-based approach. Journal of Clinical Densitometry 2021;24:112–7.

[219] Ferizi U, Besser H, Hysi P, Jacobs J, Rajapakse CS, Chen C, et al. Artificial intelligence applied to osteoporosis: a performance comparison of machine learning algorithms in predicting fragility fractures from MRI data. Journal of Magnetic Resonance Imaging 2019;49:1029–38.

[220] Ferizi U, Honig S, Chang G. Artificial intelligence, osteoporosis and fragility fractures. Curr Opin Rheumatol 2019;31:368.

[221] Madelin G, Poidevin F, Makrymallis A, Regatte RR. Classification of sodium MRI data of cartilage using machine learning. Magn Reson Med 2015;74:1435–48.

[222] Kruse C, Eiken P, Vestergaard P. Machine learning principles can improve hip fracture prediction. Calcif Tissue Int 2017;100:348–60.

[223] Hirvasniemi J, Gielis WP, Arbabi S, Agricola R, van Spil WE, Arbabi V, et al. Bone texture analysis for prediction of incident radiographic hip osteoarthritis using machine learning: data from the Cohort Hip and Cohort Knee (CHECK) study. Osteoarthritis Cartilage 2019;27:906–14.

[224] Le Corroller T, Halgrin J, Pithioux M, Guenoun D, Chabrand P, Champsaur P. Combination of texture analysis and bone mineral density improves the prediction of fracture load in human femurs. Osteoporosis International 2012;23:163–9.

[225] Thomas R, Qin L, Alessandrino F, Sahu SP, Guerra PJ, Krajewski KM, et al. A review of the principles of texture analysis and its role in imaging of genitourinary neoplasms. Abdominal Radiology 2019;44:2501–10.

[226] Hall M. Correlation-based Feature Selection for Machine Learning. The University of Waikato, 1999.

[227] Dash M, Liu H. Consistency-based search in feature selection. Artif Intell 2003;151:155–76.

[228] Hall MA, Smith LA. Practical feature subset selection for machine learning 1998.

[229] Kononenko I. Estimating attributes: Analysis and extensions of RELIEF. ECML, vol. 94, Citeseer; 1994, p. 171–82.

[230] Guyon I, Weston J, Barnhill S, Vapnik V. Gene selection for cancer classification using support vector machines. Mach Learn 2002;46:389–422.

[231] Tibshirani R. Regression shrinkage and selection via the lasso. Journal of the Royal Statistical Society: Series B (Methodological) 1996;58:267–88.

[232] Maldonado S, Weber R. A wrapper method for feature selection using support vector machines. Inf Sci (N Y) 2009;179:2208–17.

[233] Remeseiro B, Bolon-Canedo V. A review of feature selection methods in medical applications. Comput Biol Med 2019;112:103375.

[234] Wold S, Esbensen K, Geladi P. Principal component analysis. Chemometrics and Intelligent Laboratory Systems 1987;2:37–52.

[235] Jolliffe IT, Cadima J. Principal component analysis: a review and recent developments. Philosophical Transactions of the Royal Society A: Mathematical, Physical and Engineering Sciences 2016;374:20150202.

[236] van Walraven C, Musselman R. The Surgical Site Infection Risk Score (SSIRS): a model to predict the risk of surgical site infections. PLoS One 2013;8:e67167.

[237] Culver DH, Horan TC, Gaynes RP, Martone WJ, Jarvis WR, Emori TG, et al. Surgical wound infection rates by wound class, operative procedure, and patient risk index. Am J Med 1991;91:S152–7.

[238] Solarino G, Abate A, Vicenti G, Spinarelli A, Piazzolla A, Moretti B. Reducing periprosthetic joint infection: what really counts? Joints 2015;3:208–14.

[239] Møller AM, Villebro N, Pedersen T, Tønnesen H. Effect of preoperative smoking intervention on postoperative complications: a randomised clinical trial. The Lancet 2002;359:114–7.

[240] Halabi SS, Prevedello LM, Kalpathy-Cramer J, Mamonov AB, Bilbily A, Cicero M, et al. The RSNA pediatric bone age machine learning challenge. Radiology 2019;290:498.

[241] Shohat N, Goswami K, Tan TL, Yayac M, Soriano A, Sousa R, et al. 2020 Frank Stinchfield Award: identifying who will fail following irrigation and debridement for prosthetic joint infection: a machine learning-based validated tool. Bone Joint J 2020;102:11–9.

[242] Klemt C, Laurencin S, Uzosike AC, Burns JC, Costales TG, Yeo I, et al. Machine learning models accurately predict recurrent infection following revision total knee arthroplasty for periprosthetic joint infection. Knee Surgery, Sports Traumatology, Arthroscopy 2022;30:2582–90.

[243] Green III JM, Sabino J, Fleming M, Valerio I. Intraoperative fluorescence angiography: a review of applications and outcomes in war-related trauma. Mil Med 2015;180:37–43.

[244] Glenny RW. Manual for using fluorescent microspheres to measure regional organ perfusion. Washington, Fluorescent Microsphere Resource Center 1996.

[245] Byrd BK, Wirth DJ, Meng B, Strawbridge RS, Davis SC. A hyperspectral approach for recovering agent excretion biodistributions using whole-body fluorescence cryo-imaging. Molecular-Guided Surgery: Molecules, Devices, and Applications VII, vol. 11625, SPIE; 2021, p. 19–23.

[246] Reinhard E, Khan EA, Akyuz AO, Johnson G. Color imaging: fundamentals and applications. CRC Press; 2008.

[247] Davis SC, Samkoe KS, Tichauer KM, Sexton KJ, Gunn JR, Deharvengt SJ, et al. Dynamic dual-tracer MRI-guided fluorescence tomography to quantify receptor density in vivo. Proceedings of the National Academy of Sciences 2013;110:9025–30.

[248] Krishnamurthi G, Wang CY, Steyer G, Wilson DL. Removal of subsurface fluorescence in cryo-imaging using deconvolution. Opt Express 2010;18:22324–38.

[249] Serra J. Image analysis and mathematical morphol-ogy. (No Title) 1982.

[250] Bolte S, Cordelières FP. A guided tour into subcellular colocalization analysis in light microscopy. J Microsc 2006;224:213–32.

[251] Han X, Demidov V, Wirth D, Byrd B, Davis S, Gitajn L, et al. Validation of dynamic contrast-enhanced bone blood flow imaging technique with fluorescent microspheres. Molecular-Guided Surgery: Molecules, Devices, and Applications VIII, vol. 11943, SPIE; 2022, p. 118–23.

[252] Duprée A, Rieß HC, von Kroge PH, Izbicki JR, Debus ES, Mann O, et al. Validation of quantitative assessment of indocyanine green fluorescent imaging in a one-vessel model. PLoS One 2020;15:e0240188.

[253] Demidov V V, Clark MA, Streeter SS, Sottosanti JS, Gitajn IL, Elliott JT. High-energy open-fracture model with initial experience of fluorescence-guided bone perfusion assessment. Journal of Orthopaedic Research® 2022.

[254] Bonnarens F, Einhorn TA. Production of a standard closed fracture in laboratory animal bone. Journal of Orthopaedic Research 1984;2:97–101.

[255] Demidov V, Bond MC, Gitajn IL, Nadell CD, Elliott JT. Antimicrobial PDT effectively destroys E. coli and E. faecalis orthopaedic biofilms compared to low efficacy of a tobramycin and vancomycin mixture: an in vitro study using optical coherence tomography. Photonic Diagnosis, Monitoring, Prevention, and Treatment of Infections and Inflammatory Diseases 2023, vol. 12358, SPIE; 2023, p. 25–30.

[256] Moormeier DE, Bose JL, Horswill AR, Bayles KW. Temporal and stochastic control of Staphylococcus aureus biofilm development. MBio 2014;5:e01341-14.

[257] Pohler OEM. Unalloyed titanium for implants in bone surgery. Injury 2000;31:D7–13. https://doi.org/https://doi.org/10.1016/S0020-1383(00)80016-9.

[258] Wagner C, Aytac S, Hänsch GM. Biofilm growth on implants: bacteria prefer plasma coats. Int J Artif Organs 2011;34:811–7.

[259] Knecht CS, Moley JP, McGrath MS, Granger JF, Stoodley P, Dusane DH. Antibiotic loaded calcium sulfate bead and pulse lavage eradicates biofilms on metal implant materials in vitro. Journal of Orthopaedic Research® 2018;36:2349–54.

[260] Moley JP, McGrath MS, Granger JF, Stoodley P, Dusane DH. Reduction in Pseudomonas aeruginosa and Staphylococcus aureus biofilms from implant materials in a diffusion dominated environment. Journal of Orthopaedic Research® 2018;36:3081–5.

[261] Nguyen JT, Ashitate Y, Buchanan IA, Ibrahim AMS, Gioux S, Patel PP, et al. Bone flap perfusion assessment using near-infrared fluorescence imaging. Journal of Surgical Research 2012;178:e43–50.

[262] Fichter AM, Ritschl LM, Georg R, Kolk A, Kesting MR, Wolff K-D, et al. Effect of segment length and number of osteotomy sites on cancellous bone perfusion in free fibula flaps. J Reconstr Microsurg 2019;35:108–16.

[263] Michi M, Madu M, Winters HAH, de Bruin DM, van der Vorst JR, Driessen C. Near-Infrared Fluorescence with Indocyanine Green to Assess Bone Perfusion: A Systematic Review. Life 2022;12:154.

[264] Matsui A, Winer JH, Laurence RG, Frangioni J V. Predicting the survival of experimental ischaemic small bowel using intraoperative near-infrared fluorescence angiography. Journal of British Surgery 2011;98:1725–34.

[265] Diana M, Halvax P, Dallemagne B, Nagao Y, Diemunsch P, Charles A-L, et al. Real-time navigation by fluorescence-based enhanced reality for precise estimation of future anastomotic site in digestive surgery. Surg Endosc 2014;28:3108–18.

[266] Diana M, Noll E, Diemunsch P, Dallemagne B, Benahmed MA, Agnus V, et al. Enhanced-reality video fluorescence: a real-time assessment of intestinal viability. Ann Surg 2014;259:700–7.

[267] Diana M, Agnus V, Halvax P, Liu Y-Y, Dallemagne B, Schlagowski A-I, et al. Intraoperative fluorescence-based enhanced reality laparoscopic real-time imaging to assess bowel perfusion at the anastomotic site in an experimental model. Journal of British Surgery 2015;102:e169–76.

[268] Seeliger B, Agnus V, Mascagni P, Barberio M, Longo F, Lapergola A, et al. Simultaneous computer-assisted assessment of mucosal and serosal perfusion in a model of segmental colonic ischemia. Surg Endosc 2020;34:4818–27.

[269] Wada T, Kawada K, Takahashi R, Yoshitomi M, Hida K, Hasegawa S, et al. ICG fluorescence imaging for quantitative evaluation of colonic perfusion in laparoscopic colorectal surgery. Surg Endosc 2017;31:4184–93.

[270] Tang Y, Gitajn IL, Cao X, Han X, Elliott JT, Yu X, et al. Automated motion artifact correction for dynamic contrast-enhanced fluorescence imaging during open orthopedic surgery. Molecular-Guided Surgery: Molecules, Devices, and Applications IX, vol. 12361, SPIE; 2023, p. 17–20.

[271] Wang Y, Huang W, Panicek DM, Schwartz LH, Koutcher JA. Feasibility of using limited-population-based arterial input function for pharmacokinetic modeling of osteosarcoma dynamic contrast-enhanced MRI data. Magnetic Resonance in Medicine: An Official Journal of the International Society for Magnetic Resonance in Medicine 2008;59:1183–9.

[272] Ishizawa T, Fukushima N, Shibahara J, Masuda K, Tamura S, Aoki T, et al. Real-time identification of liver cancers by using indocyanine green fluorescent imaging. Cancer 2009;115:2491–504.

[273] Uchiyama K, Ueno M, Ozawa S, Kiriyama S, Shigekawa Y, Yamaue H. Combined use of contrast-enhanced intraoperative ultrasonography and a fluorescence navigation system for identifying hepatic metastases. World J Surg 2010;34:2953–9.

[274] Peloso A, Franchi E, Canepa MC, Barbieri L, Briani L, Ferrario J, et al. Combined use of intraoperative ultrasound and indocyanine green fluorescence imaging to detect liver metastases from colorectal cancer. Hpb 2013;15:928–34.

[275] Ishizuka M, Kubota K, Kita J, Shimoda M, Kato M, Sawada T. Intraoperative observation using a fluorescence imaging instrument during hepatic resection for liver metastasis from colorectal cancer. Hepato Gastroenterology-Current Medical and Surgical Trends 2012;59:90.

[276] Murawa D, Hirche C, Dresel S, Hünerbein M. Sentinel lymph node biopsy in breast cancer guided by indocyanine green fluorescence. Journal of British Surgery 2009;96:1289–94.

[277] Hojo T, Nagao T, Kikuyama M, Akashi S, Kinoshita T. Evaluation of sentinel node biopsy by combined fluorescent and dye method and lymph flow for breast cancer. The Breast 2010;19:210–3.

[278] Kitai T, Inomoto T, Miwa M, Shikayama T. Fluorescence navigation with indocyanine green for detecting sentinel lymph nodes in breast cancer. Breast Cancer 2005;12:211–5.

[279] Sevick-Muraca EM, Sharma R, Rasmussen JC, Marshall M V, Wendt JA, Pham HQ, et al. Imaging of lymph flow in breast cancer patients after microdose administration of a near-infrared fluorophore: feasibility study. Radiology 2008;246:734–41.

[280] Hirche C, Murawa D, Mohr Z, Kneif S, Hünerbein M. ICG fluorescence-guided sentinel node biopsy for axillary nodal staging in breast cancer. Breast Cancer Res Treat 2010;121:373–8.

[281] Whitney MA, Crisp JL, Nguyen LT, Friedman B, Gross LA, Steinbach P, et al. Fluorescent peptides highlight peripheral nerves during surgery in mice. Nat Biotechnol 2011;29:352–6.

[282] Gibbs-Strauss SL, Nasr KA, Fish KM, Khullar O, Ashitate Y, Siclovan TM, et al. Nerve-highlighting fluorescent contrast agents for image-guided surgery. Mol Imaging 2011;10:2010–7290.

[283] Medved M, Karczmar G, Yang C, Dignam J, Gajewski TF, Kindler H, et al. Semiquantitative analysis of dynamic contrast enhanced MRI in cancer patients: variability and changes in tumor tissue over time. Journal of Magnetic Resonance Imaging: An Official Journal of the International Society for Magnetic Resonance in Medicine 2004;20:122–8.

[284] Zahra MA, Tan LT, Priest AN, Graves MJ, Arends M, Crawford RAF, et al. Semiquantitative and quantitative dynamic contrast-enhanced magnetic resonance imaging measurements predict radiation response in cervix cancer. Int J Radiat Oncol Biol Phys 2009;74:766–73.

[285] Cuenod CA, Balvay D. Perfusion and vascular permeability: basic concepts and measurement in DCE-CT and DCE-MRI. Diagn Interv Imaging 2013;94:1187–204.

[286] Miles KA, Lee T-Y, Goh V, Klotz E, Cuenod C, Bisdas S, et al. Current status and guidelines for the assessment of tumour vascular support with dynamic contrast-enhanced computed tomography. Eur Radiol 2012;22:1430–41.

[287] Barney J, Piuzzi N, Akhondi H. Femoral Head Avascular Necrosis. StatPearls, StatPearls Publishing; 2020.

[288] Beltran J, Burk JM, Herman LJ, Clark RN, Zuelzer WA, Freedy MR, et al. Avascular necrosis of the femoral head: early MRI detection and radiological correlation. Magn Reson Imaging 1987;5:431–42.

[289] Krammer D, Schmidmaier G, Weber M-A, Doll J, Rehnitz C, Fischer C. Contrast-enhanced ultrasound quantifies the perfusion within tibial non-unions and predicts the outcome of revision surgery. Ultrasound Med Biol 2018;44:1853–9.

[290] Parmar C, Grossmann P, Bussink J, Lambin P, Aerts HJWL. Machine learning methods for quantitative radiomic biomarkers. Sci Rep 2015;5:1–11.

[291] Antropova N, Huynh BQ, Giger ML. A deep feature fusion methodology for breast cancer diagnosis demonstrated on three imaging modality datasets. Med Phys 2017;44:5162–71.

[292] Yao Y, Zhang F, Wang B, Wan J, Si L, Dong Y, et al. Polarization imaging-based radiomics approach for the staging of liver fibrosis. Biomed Opt Express 2022;13:1564–80.

[293] Pires L, Demidov V, Vitkin IA, Bagnato V, Kurachi C, Wilson BC. Optical clearing of melanoma in vivo: characterization by diffuse reflectance spectroscopy and optical coherence tomography. J Biomed Opt 2016;21:81210.

[294] Pires L, Demidov V, Wilson BC, Salvio AG, Moriyama L, Bagnato VS, et al. Dual-agent photodynamic therapy with optical clearing eradicates pigmented melanoma in preclinical tumor models. Cancers (Basel) 2020;12:1956.

[295] McBride TO, Pogue BW, Poplack S, Soho S, Wells WA, Jiang S, et al. Multispectral near-infrared tomography: a case study in compensating for water and lipid content in hemoglobin imaging of the breast. J Biomed Opt 2002;7:72–9.

[296] Pires L, Requena MB, Demidov V, Salvio AG, Vitkin IA, Wilson BC, et al. The role of optical clearing to enhance the applications of in vivo OCT and photodynamic therapy: towards PDT of pigmented melanomas and beyond. Handbook of Tissue Optical Clearing: New Prospects in Optical Imaging 2022.

[297] Demidov V, Demidova N, Pires L, Demidova O, Flueraru C, Wilson BC, et al. Volumetric tumor delineation and assessment of its early response to radiotherapy with optical coherence tomography. Biomed Opt Express 2021;12:2952–67.

[298] Lever J, Krzywinski M, Altman N. Points of significance: Principal component analysis. Nat Methods 2017;14:641–3.

[299] Chen CH. Handbook of pattern recognition and computer vision. World Scientific; 2015.

[300] Bouvet M, Hoffman RM. Glowing tumors make for better detection and resection. Sci Transl Med 2011;3:110fs10-110fs10.

[301] Boni L, David G, Mangano A, Dionigi G, Rausei S, Spampatti S, et al. Clinical applications of indocyanine green (ICG) enhanced fluorescence in laparoscopic surgery. Surg Endosc 2015;29:2046–55.

[302] Holm C, Mayr M, Höfter E, Becker A, Pfeiffer UJ, Mühlbauer W. Intraoperative evaluation of skin-flap viability using laser-induced fluorescence of indocyanine green. Br J Plast Surg 2002;55:635–44.

[303] Han X, Demidov V, Jiang S, Gitajn IL, Elliott JT. Intraoperative assessment of patient bone viability using texture analysis of dynamic contrast-enhanced fluorescence imaging. European Conference on Biomedical Optics, Optical Society of America; 2021, p. EM2A-1.

[304] DSouza A V, Lin H, Henderson ER, Samkoe KS, Pogue BW. Review of fluorescence guided surgery systems: identification of key performance capabilities beyond indocyanine green imaging. J Biomed Opt 2016;21:80901.

[305] Van Timmeren JE, Cester D, Tanadini-Lang S, Alkadhi H, Baessler B. Radiomics in medical imaging—"how-to" guide and critical reflection. Insights Imaging 2020;11:1–16.

[306] Dennis Cheong LH, Tchoyoson Lim CC, Koh TS. Dynamic contrast-enhanced CT of intracranial meningioma: comparison of distributed and compartmental tracer kinetic models—initial results. Radiology 2004;232:921–30.